

# Axial Vector Form Factors of the Nucleon from Lattice QCD

Rajan Gupta,<sup>1,\*</sup> Yong-Chull Jang,<sup>1,†</sup> Huey-Wen Lin,<sup>2,‡</sup> Boram Yoon,<sup>3,§</sup> and Tanmoy Bhattacharya<sup>1,¶</sup>  
(Precision Neutron Decay Matrix Elements (PNDME) Collaboration)

<sup>1</sup>*Los Alamos National Laboratory, Theoretical Division T-2, Los Alamos, NM 87545*

<sup>2</sup>*Department of Physics and Astronomy, Michigan State University, MI, 48824, U.S.A*

<sup>3</sup>*Los Alamos National Laboratory, Computer Computational and Statistical Sciences, CCS-7, Los Alamos, NM 87545*

(Dated: August 17, 2017)

We present results for the form factors of the isovector axial vector current in the nucleon state using large scale simulations of lattice QCD. The calculations were done using eight ensembles of gauge configurations generated by the MILC collaboration using the HISQ action with 2+1+1 dynamical flavors. These ensembles span three lattice spacings  $a \approx 0.06, 0.09$  and  $0.12$  fm and light-quark masses corresponding to the pion masses  $M_\pi \approx 135, 225$  and  $310$  MeV. High-statistics estimates allow us to quantify systematic uncertainties in the extraction of  $G_A(Q^2)$  and the induced pseudoscalar form factor  $\tilde{G}_P(Q^2)$ . We perform a simultaneous extrapolation in the lattice spacing, lattice volume and light-quark masses of the axial charge radius  $r_A$  data to obtain physical estimates. Using the dipole ansatz to fit the  $Q^2$  behavior we obtain  $r_A|_{\text{dipole}} = 0.49(3)$  fm, which corresponds to  $\mathcal{M}_A = 1.39(9)$  GeV, and is consistent with  $\mathcal{M}_A = 1.35(17)$  GeV obtained by the miniBooNE collaboration. The estimate obtained using the  $z$ -expansion is  $r_A|_{z-\text{expansion}} = 0.46(6)$  fm, and the combined result is  $r_A|_{\text{combined}} = 0.48(4)$  fm. Analysis of the induced pseudoscalar form factor  $\tilde{G}_P(Q^2)$  yields low estimates for  $g_P^*$  and  $g_{\pi NN}$  compared to their phenomenological values. To understand these, we analyze the partially conserved axial current (PCAC) relation by also calculating the pseudoscalar form factor. We find that these low values are due to large deviations in the PCAC relation between the three form factors and from the pion-pole dominance hypothesis.

PACS numbers: 11.15.Ha, 12.38.Gc

Keywords: nucleon form factors, lattice QCD, charge radii

## I. INTRODUCTION

Spurred by the demonstration of neutrino oscillations [1–4], a number of neutrino experiments are underway worldwide [5, 6] to probe more detailed properties of neutrinos including CP violation in the lepton sector, the mass hierarchy, the absolute mass scale and whether the neutrino is its own antiparticle, i.e., a Majorana neutrino. A major challenge to many of these experiments is the precise determination of the flux of neutrino beams and their cross-sections off nuclear targets. The standard model provides the strength and nature (V–A) of the interactions of the neutrinos with quarks through charged and neutral current interactions. To describe the interactions of neutrinos with nuclei, these elementary interactions have to be first corrected for the interaction between quarks and gluons, described by QCD, to account for the binding of quarks into nucleons and then by nuclear effects such as the binding of the nucleons within the nuclei. Since the energy scale of both neutrino oscillations and neutrino-less double  $\beta$ -decay ( $0\nu\beta\beta$ ) experiments is less than a few GeV, non-perturbative analyses are needed for both QCD and nuclear effects.

There is little experimental data, beyond old bubble chamber results, on neutrino scattering off nucleons. A recent analysis of the data off deuterium is given in Ref. [7]. The best data are for heavier nuclei such as carbon, oxygen and iron. The current approach used to extract the axial vector form factors of nucleons from these data is a combination of phenomenology and modeling of nuclear effects [8, 9]. As an alternate, first principle determinations of nucleon form factors using lattice QCD can be convoluted with nuclear effects to make predictions and determine the cross-sections of neutrinos off nuclei needed to analyze experimental data.

The charged current interaction of the neutrino with the nucleon is given by the matrix element of the isovector axial vector current, defined to be  $A_\mu = \bar{u}\gamma_\mu\gamma_5 d$ , within the nucleon state  $N$ . It is expressed in terms of two form factors through the relativistically covariant decomposition

$$\langle N(\vec{p}_f) | A_\mu(\vec{q}) | N(\vec{p}_i) \rangle = \bar{u}_N(\vec{p}_f) \left( G_A(q^2)\gamma_\mu + q_\mu \frac{\tilde{G}_P(q^2)}{2M_N} \right) \gamma_5 u_N(\vec{p}_i), \quad (1)$$

where  $G_A(q^2)$  is the axial vector form factor,  $\tilde{G}_P(q^2)$  is the induced pseudoscalar form factor and the momentum transfer  $\vec{q} = \vec{p}_f - \vec{p}_i$ . In this paper, we will express the form factors in terms of the space-like four-momentum transfer  $Q^2 \equiv \mathbf{p}^2 - (E - m)^2 = -q^2$ . Also, in the decomposition in Eq. (1), we neglect the induced tensor form factor  $\tilde{G}_T$  since it vanishes in the limit of isospin sym-

\* [rajan@lanl.gov](mailto:rajan@lanl.gov)

† [ypj@lanl.gov](mailto:ypj@lanl.gov)

‡ [hwlin@pa.msu.gov](mailto:hwlin@pa.msu.gov)

§ [boram@lanl.gov](mailto:boram@lanl.gov)

¶ [tanmoy@lanl.gov](mailto:tanmoy@lanl.gov)

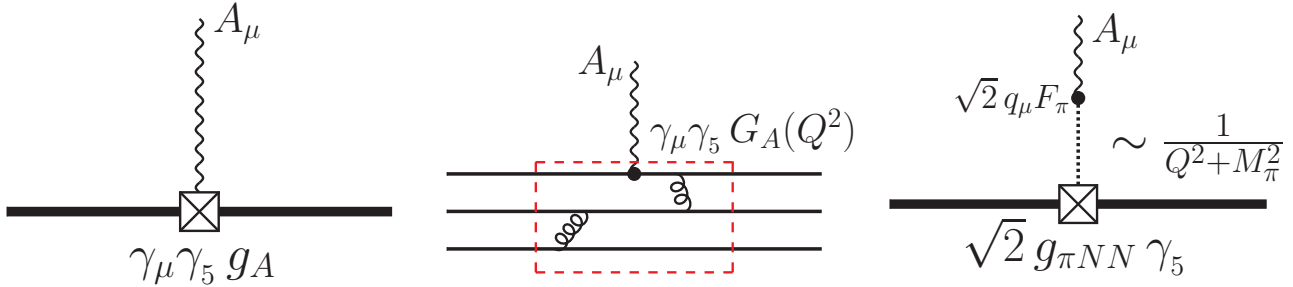


FIG. 1. The Feynman diagrams illustrating the decomposition of the matrix element of the axial current  $A_\mu = \bar{u}\gamma_\mu\gamma_5 d$  within a nucleon state in terms of form factors. The plot on the left represents the interaction at  $Q^2 = 0$  in which case the axial current interacts with the nucleon with strength  $g_A$ . The middle panel shows one of the lowest order two-gluon exchange Feynman diagrams that contributes to  $G_A(Q^2)$ , and provides the basis for the dipole ansatz. The diagram on the right is the leading contribution to the induced pseudoscalar form factor  $\tilde{G}_P(Q^2)$  by a pion intermediate state. Its coupling to the nucleon at the pion pole defines  $g_{\pi NN}$ .

metry that is implicit in this work [10], i.e., the up and down quarks are taken to be degenerate.

We also define the pseudoscalar form factor  $G_P$

$$\langle N(\vec{p}_f) | P(\vec{q}) | N(\vec{p}_i) \rangle = \bar{u}_N(\vec{p}_f) G_P(q^2) \gamma_5 u_N(\vec{p}_i), \quad (2)$$

where the operator  $P = \bar{u}\gamma_5 d$ . Contracting Eq. (1) with  $q^\mu$  and using the partially conserved axial current (PCAC) identity gives the following relation between the three form factors

$$2\hat{m}G_P(Q^2) = 2M_N G_A(Q^2) - \frac{Q^2}{2M_N} \tilde{G}_P(Q^2), \quad (3)$$

where we define  $\hat{m} \equiv Z_m Z_P (m_u + m_d) / 2Z_A$ , the common mass of the u and d quarks in our isospin symmetric theory multiplied by the appropriate renormalization constants arising in Eq. (3). This mass parameter,  $\hat{m}$ , can be measured directly on the lattice again using PCAC from the pseudoscalar two-point correlation function, i.e., by requiring that, up to lattice artifacts,  $\Gamma(t) = \langle \Omega | (\partial_\mu A_\mu - 2\hat{m}P)_t P_0 | \Omega \rangle = 0$  for all Euclidean times  $t$ . Note that  $\tilde{G}_P(Q^2)$  and  $G_P(Q^2)$  cannot be extracted at  $Q^2 = 0$ .

The three form factors can be extracted directly from the two matrix elements defined in Eqs. (1) and (2). PCAC relates them, and  $G_A(Q^2)$  and  $\tilde{G}_P(Q^2)$  are usually taken to be the two independent form factors. Since PCAC is an operator relation, it should be satisfied at all values of  $a$ ,  $M_\pi$  and  $Q^2$  up to lattice discretization effects. The first goal of large scale simulations of lattice QCD is, therefore, to calculate these three form factors with control over all systematics and show that they satisfy the PCAC relation. Only then can one compare them with phenomenological extractions to constrain/guide the modeling of nuclear effects in the calculation of the cross-section of neutrinos off nuclei.

A diagrammatic description of these form factors is as follows. At  $Q^2 = 0$  the axial current interacts with the nucleon with strength given by the axial charge  $g_A$  as shown in Fig. 1 (left). At high  $Q^2$ , the lowest order

Feynman diagram contributing to  $G_A(Q^2)$  requires two gluons to be exchanged between the three quarks in all possible combinations as illustrated in Fig. 1 (middle). This two gluon exchange amplitude at large  $Q^2$  behaves as  $1/Q^4$ , and is the historical motivation for the dipole ansatz we discuss below. In Fig. 1 (right), we show the interaction via a pion intermediate state, i.e., the axial current creates a pion intermediate state with coupling  $\sqrt{2}q^\mu F_\pi$ . This pion state propagates with the factor  $1/(Q^2 + M_\pi^2)$  before interacting with the nucleon with strength  $\sqrt{2}g_{\pi NN}$ . This diagram constitutes the lowest order contribution to the induced pseudoscalar form factor  $\tilde{G}_P(Q^2)$  and provides the motivation for analyzing it using the pion pole-dominance ansatz.

In this paper we present results for the isovector part of  $G_A$  and  $\tilde{G}_P$  in the range  $0.05 < Q^2 \lesssim 0.8$  GeV $^2$  using first principle simulations of lattice QCD on eight ensembles covering the range of lattice spacings ( $0.06 \lesssim a \lesssim 0.12$  fm), pion masses ( $135 \lesssim M_\pi \lesssim 320$  MeV) and lattice volumes ( $3.3 \lesssim M_\pi L \lesssim 5.5$ ). These ensembles were generated using  $2+1+1$ -flavors of highly improved staggered quarks (HISQ) [11] by the MILC collaboration [12]. On four of these ensembles we have also calculated the pseudoscalar form factor  $G_P$  that is needed to check the PCAC relation.

The axial radius of the nucleon is determined from the slope of  $G_A(Q^2)$  in the  $Q^2 \rightarrow 0$  limit:

$$\langle r_A^2 \rangle = -6 \frac{d}{dQ^2} \left( \frac{G_A(Q^2)}{G_A(0)} \right) \Big|_{Q^2=0}. \quad (4)$$

The challenge to the direct calculation of the slope using a discrete derivative is that the value of the smallest momenta and the intervals between the lowest few lattice momenta in typical lattice simulations are large. In our calculations, the lowest non-zero momenta is  $\gtrsim 220$  MeV. It is, therefore, customary to fit the data using a physically motivated ansatz for  $G_A(Q^2)$  and then use the result to evaluate the derivative given in Eq. (4). This modeling of  $G_A$  introduces a systematic uncertainty in

the value of  $\langle r_A^2 \rangle$  that we estimate by comparing results using different fit ansatz.

An ansatz that is commonly used to fit the experimental data is the dipole approximation

$$G_A(Q^2) = \frac{G_A(0)}{(1 + Q^2/\mathcal{M}_A^2)^2} \implies \langle r_A^2 \rangle = \frac{12}{\mathcal{M}_A^2}, \quad (5)$$

where  $\mathcal{M}_A$  is the axial dipole mass. It is the simplest one parameter form that is normalized to  $G_A(0) \equiv g_A$  at  $Q^2 = 0$  and goes as  $Q^{-4}$  in the  $Q^2 \rightarrow \infty$  limit in accord with the leading contribution in perturbation theory as shown in the middle panel of Fig. 1. Estimates of the RMS charge radius  $r_A \equiv \sqrt{\langle r_A^2 \rangle}$  obtained from (i) a weighted world average of (quasi)elastic neutrino and anti-neutrino scattering data [13], (ii) charged pion electroproduction experiments [13], and (iii) a reanalysis of the deuterium target data [7] are

$$\begin{aligned} r_A &= 0.666(17) \text{ fm} & \nu, \bar{\nu} - \text{scattering}, \\ r_A &= 0.639(10) \text{ fm} & \text{Electroproduction}, \\ r_A &= 0.68(16) \text{ fm} & \text{Deuterium}, \end{aligned} \quad (6)$$

which correspond to the dipole masses

$$\begin{aligned} \mathcal{M}_A &= 1.026(21) \text{ GeV} & \nu, \bar{\nu} - \text{scattering}, \\ \mathcal{M}_A &= 1.069(16) \text{ GeV} & \text{Electroproduction}, \\ \mathcal{M}_A &= 1.00(24) \text{ GeV} & \text{Deuterium}. \end{aligned} \quad (7)$$

On the other hand, the MiniBooNE Collaboration, using the dipole ansatz and a relativistic Fermi gas model [14], find that  $\mathcal{M}_A = 1.35(17)$  GeV reproduces their double differential cross-section for charged current quasi elastic neutrino and antineutrino scattering data off carbon [9]. Lattice QCD, by providing first-principle estimates of  $G_A(Q^2)$  for nucleons, aims to resolve the difference in the phenomenological estimates and to pin down the  $Q^2$  behavior of the form factors.

The analysis presented here shows that the dipole ansatz fits the lattice data surprisingly well, however, our result,  $r_A|_{\text{dipole}} = 0.49(3)$ , is smaller than the phenomenological estimates given in Eq. (6).

The second ansatz we use is a model-independent parameterization called the  $z$ -expansion [15, 16]:

$$\frac{G_A(Q^2)}{G_A(0)} = \sum_{k=0}^{\infty} a_k z(Q^2)^k, \quad (8)$$

where the  $a_k$  are fit parameters and  $z$  is defined as

$$z = \frac{\sqrt{t_{\text{cut}} + Q^2} - \sqrt{t_{\text{cut}} + \bar{t}_0}}{\sqrt{t_{\text{cut}} + Q^2} + \sqrt{t_{\text{cut}} + \bar{t}_0}}, \quad (9)$$

with  $t_{\text{cut}} \equiv Q_{\text{cut}}^2 = 9M_\pi^2$ . The nearest singularity in the form factor  $G_A(Q^2)$  is the three-pion branch cut at  $Q^2 = 9M_\pi^2$ . In terms of  $z$ , the domain of analyticity of  $G_A(Q^2)$  is mapped into the unit circle with the three-pion branch cut at  $t_{\text{cut}} = 9M_\pi^2$  moved to  $z = 1$  [16]. The value of the constant  $\bar{t}_0$  is typically chosen to be

in the middle of the range of  $Q^2$  of interest to minimize  $z_{\text{max}}$  and possibly improve the convergence of the  $z$ -expansion. The choice of  $\bar{t}_0$  could have been important in our calculation because we have data at only the five lowest values of momenta on most ensembles and can, therefore, perform an analysis keeping terms only up to  $O(z^4)$ . Our analysis of the data with  $\bar{t}_0 = 0$  and  $\bar{t}_0 = \bar{t}_0^{\text{mid}} \equiv \{0.12, 0.20, 0.40\}$  GeV<sup>2</sup>, corresponding to the approximate midpoint of the range of  $Q^2$  on the  $M_\pi \approx \{130, 220, 310\}$  MeV ensembles, respectively, however shows that the quality of the fits and the results are insensitive to the choice of  $\bar{t}_0$ . For presenting our final results, we choose the midpoint values,  $\bar{t}_0^{\text{mid}}$ .

The asymptotic requirement, that  $G_A(Q^2) \rightarrow Q^{-4}$  as  $Q^2 \rightarrow \infty$ , requires  $Q^n G_A(Q^2) \rightarrow 0$  for  $n = 0, 1, 2, 3$  [17]. These constraints can be incorporated into the  $z$ -expansion as four sum rules

$$\sum_{k=n}^{k_{\text{max}}} k(k-1)\dots(k-n+1)a_k = 0 \quad n = 0, 1, 2, 3, \quad (10)$$

where for  $n = 0$  it is  $\sum_{k=0}^{k_{\text{max}}} a_k = 0$ . Incorporating these sumrules ensures that the  $a_k$  are not only bounded but must also decrease at large  $k$  [17]. We have six data points (zero and five non-zero momentum cases) for all but the two physical quark mass ensembles,  $a09m130$  and  $a06m135$ . The analysis was therefore done using  $k_{\text{max}} = 5, 6, 7$  and  $8$ . Including the four sum rules, these values of  $k_{\text{max}}$  correspond to  $4, 3, 2$ , and  $1$  degrees of freedom, respectively. We use the quality of the fits and the stability of the value of the axial charge radius squared  $\langle r_A^2 \rangle$  obtained from them as checks on the consistency of the analysis, ensemble by ensemble. Based on these checks, we drop  $k_{\text{max}} = 5$  fits as the associated  $\chi^2/\text{d.o.f.}$  are not good and the  $k_{\text{max}} = 8$  fits, as they are unstable in many cases.

Our final result,  $r_A|_{z\text{-expansion}} = 0.46(6)$  fm, is obtained as an average of the  $k_{\text{max}} = 6$  and  $7$  analyses, which we label  $k^{2+4}$  and  $k^{3+4}$  to make explicit that four powers of  $z$  are constrained by the sumrules. This lattice estimate is again smaller than the current phenomenological estimates given in Eq. (6). The uncertainty in the estimates, ensemble by ensemble, is larger with the  $z$ -expansion versus the dipole ansatz.

The induced pseudoscalar form factor  $\tilde{G}_P(Q^2)$  is typically analyzed assuming the pion pole-dominance ansatz:

$$\tilde{G}_P(Q^2) \propto G_A(Q^2) \left[ \frac{1}{Q^2 + M_\pi^2} \right], \quad (11)$$

where the coefficient of proportionality is often taken to  $4M_N^2$  as suggested by the Goldberger-Trieman relation [18]. This behavior is consistent with the PCAC relation, Eq. (3), only if  $2\tilde{m}G_P(Q^2) = (M_\pi^2/2M_N)\tilde{G}_P(Q^2)$ . If this ansatz is a good approximation, then there is only one independent form factor, which can be taken to be  $G_A(Q^2)$  or  $\tilde{G}_P(Q^2)$ .

Ensemble ID	$a$ (fm)	$M_\pi^{\text{sea}}$ (MeV)	$M_\pi^{\text{val}}$ (MeV)	$L^3 \times T$	$M_\pi^{\text{val}} L$	$t_{\text{sep}}/a$	$N_{\text{conf}}$	$N_{\text{meas}}^{\text{HP}}$	$N_{\text{meas}}^{\text{AMA}}$
a12m310	0.1207(11)	305.3(4)	310.2(2.8)	$24^3 \times 64$	4.55	{8, 10, 12}	1013	8104	64,832
a12m220L	0.1189(09)	217.0(2)	227.6(1.7)	$40^3 \times 64$	5.49	{8, 10, 12, 14}	1010	8080	68,680
a09m310	0.0888(08)	312.7(6)	313.0(2.8)	$32^3 \times 96$	4.51	{10, 12, 14}	881	7048	
a09m220	0.0872(07)	220.3(2)	225.9(1.8)	$48^3 \times 96$	4.79	{10, 12, 14}	890	7120	
a09m130	0.0871(06)	128.2(1)	138.1(1.0)	$64^3 \times 96$	3.90	{10, 12, 14}	883	7064	60,044
a06m310	0.0582(04)	319.3(5)	319.6(2.2)	$48^3 \times 144$	4.52	{16, 20, 22, 24}	1000	8000	64,000
a06m220	0.0578(04)	229.2(4)	235.2(1.7)	$64^3 \times 144$	4.41	{16, 20, 22, 24}	650	2600	41,600
a06m135	0.0570(01)	135.5(2)	135.6(1.4)	$96^3 \times 192$	3.7	{16, 18, 20, 22}	322	1610	51,520

TABLE I. Parameters, including the Goldstone pion mass  $M_\pi^{\text{sea}}$ , of the eight 2+1+1- flavor HISQ lattices generated by the MILC collaboration and analyzed in this study are quoted from Ref. [12]. All fits are made versus  $M_\pi^{\text{val}}$  and finite-size effects are analyzed in terms of  $M_\pi^{\text{val}} L$ . Estimates of  $M_\pi^{\text{val}}$ , the clover-on-HISQ pion mass, are the same as given in Ref. [19] and the error is governed mainly by the uncertainty in the lattice scale. In the last four columns, we give, for each ensemble, the values of the source-sink separation  $t_{\text{sep}}$  used in the calculation of the three-point functions, the number of configurations analyzed, and the number of measurements made using the HP and AMA methods. The HP calculation on the  $a12m220L$  ensemble has been done with a single  $t_{\text{sep}} = 10$  while the LP analysis has been done with  $t_{\text{sep}} = \{8, 10, 12, 14\}$ .

Experimentally,  $\tilde{G}_P(Q^2)$  is probed in muon capture by a proton,  $\mu^- + p \rightarrow \nu_\mu + n$  [20, 21]. From these measurements, the induced pseudoscalar charge  $g_P^*$  is defined as

$$g_P^* \equiv \frac{m_\mu}{2M_N} \tilde{G}_P(Q^2 = Q^{*2} \equiv 0.88m_\mu^2). \quad (12)$$

Current estimates from the MuCap experiment [20, 21], and from chiral perturbation theory [13, 22] are

$$\begin{aligned} g_P^*|_{\text{MuCap}} &= 8.06(55), \\ g_P^*|_{\chi\text{PT}} &= 8.29^{+0.24}_{-0.13} \pm 0.52. \end{aligned} \quad (13)$$

On the lattice, once the modeling of the  $Q^2$  behavior of  $\tilde{G}_P(Q^2)$  is under control, one can determine  $g_P^*$  by extrapolation to  $Q^2 = Q^{*2} \equiv 0.88m_\mu^2$  and the pion-nucleon coupling  $g_{\pi\text{NN}}$  as the residue at  $Q^2 = -M_\pi^2$ . To compare our lattice QCD estimates with these phenomenological values, we first extract  $g_P^*$  from fits to  $\tilde{G}_P(Q^2)$  versus  $Q^2$  for each ensemble, and then extrapolate these data to  $a = 0$  and  $M_\pi = 135$  MeV. The result is a surprisingly low value,  $g_P^* = 4.44(18)$ , compared to the values given in Eq. (13). This discrepancy arises due to large deviations from the PCAC relation involving the three form factors as discussed further in Sec. VIII. We also show that using just the pion-pole ansatz to extrapolate  $g_P^*(Q^{*2})$  obtained from simulations at  $M_\pi > 300$  MeV to  $M_\pi \rightarrow M_\pi^{\text{Physical}} = 135$  MeV does not match our lattice data at  $M_\pi = 220$  or 135 MeV.

Lastly, we evaluate the pion-nucleon coupling  $g_{\pi\text{NN}}$  using the Goldberger-Treiman (GT) relation  $g_{\pi\text{NN}} = M_N g_A/F_\pi$ , and as the residue at the pion pole at  $Q^2 = -M_\pi^2$  of  $\tilde{G}_P(Q^2)$ . As discussed in Sec. X, our estimate,  $g_{\pi\text{NN}} = M_N g_A/F_\pi = 12.87(34)$  using the lattice data is consistent with that obtained using the experimental values. Our direct calculation of  $g_{\pi\text{NN}}$ , as the residue of  $\tilde{G}_P(Q^2)$  at the pion pole, suffers from the same problem as the analysis of  $g_P^*$  and gives  $g_{\pi\text{NN}} =$

5.78(57), much smaller than the phenomenological estimate  $13.69 \pm 0.12 \pm 0.15$  obtained from the  $\pi N$  scattering length analysis [23].

This paper is organized as follows. In Sec. II, we describe the parameters of the gauge ensembles analyzed and the lattice methodology. The strategy used to isolate excited-state contamination is described in Sec. III. In Sec. IV, we present the analysis of the two-point correlation functions. The extraction of the form factors from the three-point functions is discussed in Sec. V, and of the axial charge radius  $r_A$  from these in Sec. VI. Simultaneous fits in the lattice spacing  $a$ , the pion mass  $M_\pi$  and the lattice size  $M_\pi L$  to obtain our physical estimate of  $r_A$  are presented in Sec. VII. The analysis of the induced pseudoscalar form factor is carried out in Sec. VIII, of  $g_P^*$  in Sec. IX, and of the pion-nucleon coupling,  $g_{\pi\text{NN}}$ , in Sec. X. In Sec. XI, we present a heuristic analysis to understand violations of the PCAC relation between  $G_A(Q^2)$ ,  $\tilde{G}_P(Q^2)$ , and  $G_P(Q^2)$ . We end with conclusions in Sec. XII.

## II. LATTICE METHODOLOGY

The eight ensembles used in the analysis cover a range of lattice spacings ( $0.06 \lesssim a \lesssim 0.12$  fm), pion masses ( $135 \lesssim M_\pi \lesssim 320$  MeV) and lattice volumes ( $3.3 \lesssim M_\pi L \lesssim 5.5$ ). These were generated using 2+1+1-flavors of highly improved staggered quarks (HISQ) [11] by the MILC collaboration [12] and their parameters are summarized in Table I. Results for the isovector charges,  $g_A^{u-d}$ ,  $g_S^{u-d}$  and  $g_T^{u-d}$  on these ensembles have already been published in Refs. [19, 25]. In this work we follow the same computational strategy, so we only summarize the important issues and point the reader to the appropriate references for details.

The correlation functions used to calculate the matrix

ID	$m_l$	$c_{\text{sw}}$	Smearing Parameters
a12m310	-0.0695	1.05094	{5.5, 70}
a12m220L	-0.075	1.05091	{5.5, 70}
a09m310	-0.05138	1.04243	{5.5, 70}
a09m220	-0.0554	1.04239	{5.5, 70}
a09m130	-0.058	1.04239	{5.5, 70}
a06m310	-0.0398	1.03493	{6.5, 70}
a06m220	-0.04222	1.03493	{5.5, 70}
a06m135	-0.044	1.03493	{9.0, 150}

TABLE II. The parameters used in the calculation of clover propagators. The hopping parameter  $\kappa$  in the clover action is given by  $2\kappa_l = 1/(m_l + 4)$ . The Gaussian smearing parameters are defined by  $\{\sigma, N_{\text{KG}}\}$  where  $N_{\text{KG}}$  is the number of applications of the Klein-Gordon operator and the width of the smearing is controlled by the coefficient  $\sigma$ , both in Chroma convention [24].  $m_l$  is tuned to achieve  $M_\pi^{\text{val}} \approx M_\pi^{\text{sea}}$ .

elements on these HISQ ensembles are constructed using Wilson-clover fermions after the lattices have been smoothed using hypercubic (HYP) smearing [26]. This mixed-action, clover-on-HISQ approach, leads to a non-unitary lattice formulation that at small, but *a priori* unknown, quark masses suffers from the problem of exceptional configurations. As described in Ref. [19], tests performed by us did not find configurations exhibiting large deviations from the mean behavior on these ensembles.

The parameters used to construct the quark propagators with the clover action are given in Table II. The Sheikholeslami-Wohlert coefficient [27] used in the clover action is fixed to its tree-level value with tadpole improvement, i.e.,  $c_{\text{sw}} = 1/u_0^3$ , where  $u_0$  is the fourth root of the plaquette expectation value calculated on the HYP smeared HISQ lattices.

The masses of light clover quarks were tuned so that the clover-on-HISQ pion masses,  $M_\pi^{\text{val}}$ , match the HISQ-on-HISQ Goldstone ones,  $M_\pi^{\text{sea}}$ . Both estimates are given in Table I. All fits in  $M_\pi^2$  to study the chiral behavior are made using the clover-on-HISQ  $M_\pi^{\text{val}}$  since the correlation functions, and thus the observables, have a greater sensitivity to it. Henceforth, we denote the clover-on-HISQ pion mass as  $M_\pi$ .

On six ensembles, we have used the truncated solver method with bias correction (labeled the AMA method) [28, 29] to cost-effectively increase the statistics in the calculation of the two- and three-point correlation functions. The details of our implementation are given in Refs. [19, 25, 30].

The two- and three-point correlation functions were constructed using the nucleon interpolating operator

$$\chi(x) = \epsilon^{abc} \left[ q_1^{aT}(x) C \gamma_5 \frac{(1 \pm \gamma_4)}{2} q_2^b(x) \right] q_1^c(x) \quad (14)$$

with color indices  $\{a, b, c\}$ , charge conjugation matrix  $C = \gamma_0 \gamma_2$ , and  $q_1$  and  $q_2$  denoting the two different flavors of light Dirac quarks. The non-relativistic projection

$(1 \pm \gamma_4)/2$  is inserted to improve the signal, with the plus (minus) sign applied to the forward (backward) propagation in Euclidean time as described in Refs. [19, 25, 30]. On the other hand, the  $\gamma_4$  part introduces mixing with spin 3/2 states at non-zero momentum, with concomitant excited-state contamination.

All errors are determined using a single-elimination Jackknife procedure. We first construct the configuration average, i.e., the mean of the correlation functions over multiple measurements on each configuration, and then implement the Jackknife process over these configuration averages. In all the fits to the two- and three-point correlation functions based on minimizing the  $\chi^2/\text{d.o.f.}$ , we used the full covariance matrix as described in Ref. [30].

The value of the axial radius from each ensemble was extracted from the form factors using two fit ansatz: the model-independent  $z$ -expansion, and the dipole fit.  $\tilde{G}_P$  was analyzed using the PCAC relation and the pion pole-dominance ansatz.

All estimates, such as  $\langle r_A^2 \rangle$  and  $g_P^*$  obtained on the eight ensembles, were simultaneously fit versus the three variables, the lattice spacing  $a$ , the pion mass  $M_\pi$ , and the lattice size parameterized by  $M_\pi L$ , keeping only the leading order correction terms in each. From these fits, the final value was obtained at the physical pion mass  $M_\pi = 135$  MeV with extrapolation to the continuum and the infinite volume limits.

The renormalization factor for the axial current cancels in the ratios used in the extraction of the axial charge radius, defined in Eq. (4), and in the analysis of  $\tilde{G}_P(Q^2)$  using the pole-dominance hypothesis given in Eq. (11). Thus, all results presented in this work are the same as for renormalized operators.

Further details of the analysis are given at appropriate places when discussing the results.

### III. CONTROLLING EXCITED-STATE CONTAMINATION

To extract the desired nucleon form factors we need to evaluate the matrix elements of the axial current between ground-state nucleons. The lattice nucleon interpolating operator given in Eq. (14), however, couples to the nucleon, all excitations and multiparticle states with the same quantum numbers. Three strategies are used to reduce excited-state contamination as described in Refs. [19, 25, 30].

- The overlap between the nucleon operator and the excited states in the construction of the two- and three-point functions is reduced by using tuned smeared sources when calculating the quark propagators on the HYP smeared HISQ lattices. We construct gauge-invariant Gaussian smeared sources by applying the three-dimensional Laplacian operator,  $\nabla^2$ , a fixed number,  $N_{\text{GS}}$ , of times, i.e.,  $(1 + \sigma^2 \nabla^2 / (4N_{\text{GS}}))^{N_{\text{GS}}}$ . The smearing parameters  $\{\sigma, N_{\text{GS}}\}$  for each ensemble are given in Table II.

- The analysis of the nucleon two-point functions,  $C^{2\text{pt}}$ , was carried out keeping four states in the spectral decomposition:

$$C^{2\text{pt}}(t, \mathbf{p}) = |\mathcal{A}_0|^2 e^{-E_0 t} + |\mathcal{A}_1|^2 e^{-E_1 t} + |\mathcal{A}_2|^2 e^{-E_2 t} + |\mathcal{A}_3|^2 e^{-E_3 t}, \quad (15)$$

where the amplitudes and the energies with momentum  $\mathbf{p}$  of the four states are denoted by  $\mathcal{A}_i$  and  $E_i$ , respectively. The strategy for the selection of non-trivial priors for the masses and amplitudes used in the fits is the same as described in Ref. [30]. A comparison between 2- and 4-state fits is shown in Figs. 22–29 in Appendix A. In the 4-state fits used in the final analysis, the starting time slice in the fit,  $t_{\min}$ , is chosen to be small to include as much data as possible while maintaining the stability of the fit parameters. Since the excited-state contamination is observed to be similar,  $t_{\min}$  is chosen to be the same for all momenta for a given ensemble. The analysis of the three-point functions,  $C_{\Gamma}^{(3\text{pt})}(t; \tau; \mathbf{p}', \mathbf{p})$  was carried out keeping two states in the spectral decomposition:

$$C_{\Gamma}^{(3\text{pt})}(t; \tau; \mathbf{p}', \mathbf{p}) = \mathcal{A}'_0 \mathcal{A}_0 \langle 0' | \mathcal{O}_{\Gamma} | 0 \rangle e^{-E_0 t - M_0(\tau - t)} + \mathcal{A}'_1 \mathcal{A}_1 \langle 1' | \mathcal{O}_{\Gamma} | 1 \rangle e^{-E_1 t - M_1(\tau - t)} + \mathcal{A}'_0 \mathcal{A}_1 \langle 0' | \mathcal{O}_{\Gamma} | 1 \rangle e^{-E_0 t - M_1(\tau - t)} + \mathcal{A}'_1 \mathcal{A}_0 \langle 1' | \mathcal{O}_{\Gamma} | 0 \rangle e^{-E_1 t - M_0(\tau - t)}, \quad (16)$$

where the source point is translated to  $t = 0$ , the operator is inserted at time  $t$ , and nucleon state is annihilated at the sink time slice  $\tau \equiv t_{\text{sep}}$ . The states  $|0\rangle$  and  $|1\rangle$  represent the ground and all higher states that we collectively label the “first excited” state, respectively. The label  $\mathcal{A}'_i$  denotes the amplitude for the creation of state  $i$  with momentum  $\mathbf{p}'$  by the nucleon interpolating operator  $\chi$ . To extract the matrix elements, we need the four amplitudes  $\mathcal{A}_0$ ,  $\mathcal{A}_1$ ,  $\mathcal{A}'_0$  and  $\mathcal{A}'_1$ , which we obtain from the 4-state fits to the two-point functions. Note that the insertion of the nucleon at the sink timeslice  $t = \tau = t_{\text{sep}}$  is at  $\mathbf{p} = 0$  in all cases, and the insertion of the current at time  $t$  is at a definite momentum  $\mathbf{p}'$ . To ensure a good signal for all  $\mathbf{p}'$ , the nucleon state at the source timeslice, constructed from smeared sources, should have a large overlap with all momentum states analyzed. The data in Figs. 22–29 show that with the smeared sources used, a decent signal is achieved for  $Q^2 \lesssim 1 \text{ GeV}^2$ .

- We calculate the three-point correlation functions for a number of values of the source-sink separation  $t_{\text{sep}}$  that are listed in Table I. We fit the data at all  $t_{\text{sep}}$  simultaneously using the 2-state ansatz given

in Eq. (16). In these fits, we skip  $t_{\text{skip}}$  points adjacent to the source and sink for each  $t_{\text{sep}}$  as these points have the largest excited state contamination. As a result, more points with larger  $t_{\text{sep}}$  that have less excited-state contamination and larger statistical errors are included. The value of  $t_{\text{skip}}$  for each ensemble is chosen to be same for all momenta since the onset of the plateau in the effective-mass plot is observed to start at roughly the same timeslice, independent of the momenta, as shown in Figs. 22–29.

From these fits we get  $\langle 0' | \mathcal{O}_{\Gamma} | 0 \rangle$ , the desired  $\tau \rightarrow \infty$  estimate. The above procedure has been followed for all values of momentum insertion and on each ensemble.

#### IV. FITS TO THE TWO-POINT FUNCTIONS

On each ensemble, we performed 2-, 3- and 4-state fits to the two-point correlation function data to extract the amplitudes and the masses. On all ensembles, we collected data for momenta  $\mathbf{p} = 2\pi\mathbf{n}/aL$  with  $\mathbf{n} = \{(0, 0, 0), (1, 0, 0), (1, 1, 0), (1, 1, 1), (2, 0, 0), (2, 1, 0)\}$ . On the  $a09m130$  and  $a06m135$  ensembles, we also collected data for  $\mathbf{n} = \{(2, 1, 1), (2, 2, 0), (2, 2, 1), (3, 0, 0), (3, 1, 0)\}$ .

We illustrate the quality of the two-point data by plotting the effective-energy defined as

$$E_{\text{eff}}(t) = \log \frac{C^{2\text{pt}}(t)}{C^{2\text{pt}}(t+1)}, \quad (17)$$

in Figs. 22, 23, 24, 25, 26, 27, 28, and 29 given in Appendix A. In each panel, we show the data for the various momentum channels analyzed. The panels on the left (right) show results of the 2-state (4-state) fits to the two-point function data for the different momenta. The data with the largest errors and the least convincing plateau at the larger momenta are from (i) the  $a09m310$  and  $a09m220$  ensembles that have lower statistics as they have not been analyzed using the AMA method, and (ii) the  $a06m220$  and  $a06m135$  ensembles at the weakest coupling that have the fewest gauge configurations analyzed. Also, on a number of ensembles, we observe correlated fluctuations in the data for  $E_{\text{eff}}$ ; both over  $t$  for a given momenta and at a given  $t$  over the various momenta. The former are taken into account by using the full covariance matrix in the fits to correlators at a given momenta. Since data at each momentum are analyzed separately, the latter are ignored.

The results for the  $M_i$  and the  $\mathcal{A}_i$  are given in Tables XI, XII, XIII, XIV, XV, XVI, XVII and XVIII in Appendix A. The results from the 2-state fit shown in these tables are slightly different from those presented in Ref. [25] because, in this study, we use the full covariance matrix when doing the fits, whereas in Ref. [25] only the diagonal elements were used.

As shown in Tables XI–XVIII, the ground state parameters,  $E_0$  and  $\mathcal{A}_0$  are consistent between the 2-, 3-

and 4-state fits. The parameters for the first excited state,  $E_1$  and  $\mathcal{A}_1$ , also needed in 2-state fits to three-point functions show stability only between the 3- and 4-state fits. When analyzing the three-point correlation functions, we, therefore, used estimates obtained from the 4-state fits for all four parameters,  $M_0$ ,  $\mathcal{A}_0$ ,  $M_1$  and  $\mathcal{A}_1$ . It is worth noting the change in the ratio  $\Delta M_1/M_0$  for the two ensembles  $a06m220$  and  $a06m135$  to about 0.85 compared to  $\lesssim 0.6$  for the other six ensembles. With the current data, we cannot ascertain whether this change is a statistical fluctuation or implies that the combination and/or the nature of excited-states contributing have changed.

When analyzing the three-point data to extract the form factors, we need to decide what definition of momenta to use, i.e., whether one should use  $ap_i$  or  $\sin(ap_i)$  or  $2\sin(ap_i/2)$  for the lattice momenta in the expression  $Q^2 = \mathbf{p}^2 - (E - m)^2$ . Since the three versions differ at  $O(a^2)$  and our calculation has errors starting at  $O(a)$ , there is no theoretical reason to prefer one over the other. For guidance, we examined the dispersion relation for the nucleon,  $(aE)^2 - \sum_i f_i^2 = (aM)^2$ , for the three cases  $f_i = ap_i$ ,  $\sin(ap_i)$  and  $2\sin(ap_i/2)$  in Fig. 30 (Appendix A), for four ensembles, two with the largest values of  $\mathbf{p}$  and the two physical mass ensembles. We find that, with our statistics, the difference between the three forms is insignificant in all cases for  $(ap)^2 < 0.1$ . Only the data at the highest momenta on the  $a12m310$ ,  $a12m220L$  and  $a09m310$  ensembles, that have results at  $(ap)^2 \gtrsim 0.1$ , do we see some variation. In short, no one form is uniformly preferred by the data on all the ensembles.<sup>1</sup> Nevertheless, we carried through the analysis to extract the axial charge radius  $r_A$  from fits to  $G_A(Q^2)$  using all three forms, and found no sensitivity to the choice of the form. As illustrated in Fig. 6, the difference between the three forms is not significant enough to even estimate an associated systematic uncertainty. We, therefore, present our final estimates using the simplest version,  $f_i = ap_i$ .

In Fig. 30 (bottom panels), we show the two points with momentum components  $n_i = (2, 2, 1)$  and  $n_i = (3, 0, 0)$ , corresponding to  $\mathbf{n}^2 = 9$ , in the  $a09m130$  and  $a06m135$  data. The difference between these two estimates is a measure of the effect of the breaking of the rotational symmetry on the lattice to the cubic group. Throughout this work, we keep these two data points separate when analyzing the  $a09m130$  and the  $a06m135$  ensembles data.

## V. EXTRACTING FORM FACTORS FROM FITS TO THE THREE-POINT FUNCTIONS

To display the data for the three-point correlation functions with the insertion of the axial current, we construct the following ratio,  $\mathcal{R}_{5\Gamma}$ , of the three-point to the two-point correlation functions,

$$\mathcal{R}_{\gamma_5\Gamma}(t, \tau, \mathbf{p}', \mathbf{p}) = \frac{C_{\Gamma}^{(3pt)}(t, \tau; \mathbf{p}', \mathbf{p})}{C^{(2pt)}(\tau, \mathbf{p}')} \times \left[ \frac{C^{(2pt)}(t, \mathbf{p}') C^{(2pt)}(\tau, \mathbf{p}') C^{(2pt)}(\tau - t, \mathbf{p})}{C^{(2pt)}(t, \mathbf{p}) C^{(2pt)}(\tau, \mathbf{p}) C^{(2pt)}(\tau - t, \mathbf{p}')} \right]^{1/2}. \quad (18)$$

This ratio gives the desired ground state matrix element in the limit  $\tau \rightarrow \infty$ ,  $t \rightarrow \infty$  and  $(\tau - t) \rightarrow \infty$ . For all the two-point correlation functions, we used the results of the 4-state fit. When calculating the matrix elements of the axial vector current, defined in Eq. (1), we use the spin projection operator  $\mathcal{P} = (1 + \gamma_4)(1 + i\gamma_5\gamma_3)/2$ . As a result, the imaginary part of the following three ratios of correlators have a signal and give the desired form factors in the limit  $t$ ,  $\tau - t$  and  $\tau \rightarrow \infty$ :

$$\mathcal{R}_{51} \rightarrow \frac{1}{\sqrt{(2E_p(E_p + M))}} \left[ -\frac{q_1 q_3}{2M} \tilde{G}_P \right], \quad (19)$$

$$\mathcal{R}_{52} \rightarrow \frac{1}{\sqrt{(2E_p(E_p + M))}} \left[ -\frac{q_2 q_3}{2M} \tilde{G}_P \right], \quad (20)$$

$$\mathcal{R}_{53} \rightarrow \frac{1}{\sqrt{(2E_p(E_p + M))}} \left[ -\frac{q_3^2}{2M} \tilde{G}_P + (M + E) G_A \right]. \quad (21)$$

where  $\mathcal{R}_{5i}$  implies the tensor structure  $\mathcal{R}_{\gamma_5\gamma_i}$ . We do not consider the  $\mathcal{R}_{54}$  channel as the signal in it is poor. The pseudoscalar form factor  $G_P(Q^2)$  is given by the real part of  $\mathcal{R}_5 \equiv \mathcal{R}_{\gamma_5}$ :

$$\mathcal{R}_5 \rightarrow \frac{1}{\sqrt{(2E_p(E_p + M))}} [q_3 G_P]. \quad (22)$$

In Fig. 2 (and in Figs. 31 and 32 in Appendix B), we give plots of the ratio  $\mathcal{R}_{53}$ , i.e., the ratio with tensor structure  $\gamma_5\gamma_3$  for the axial current, defined in Eq. (21). The data are shown for all values of  $t_{\text{sep}}$  and for two values of momenta,  $\mathbf{p} = (1, 0, 0)2\pi/La$  and  $\mathbf{p} = (2, 1, 0)2\pi/La$ . Note that both  $G_A$  and  $\tilde{G}_P$  contribute to this ratio. It is clear from the plots that the excited-state contamination is significant in the data with  $t_{\text{sep}} \approx 1$  fm for our choice of the nucleon interpolating operator, Eq. (14), and the smearing parameters given in Table II.

From these data, the matrix element within the ground state is obtained using Eq. (16), i.e., keeping two intermediate states in the fit to the three-point correlation function. The values of  $\tau \equiv t_{\text{sep}}$  and  $t_{\text{skip}}$  used in the fit are given in the figure's legend. All values of  $t_{\text{sep}}$  are fit simultaneously and the resulting  $\tau \rightarrow \infty$  estimates are shown by the horizontal band. Prediction of the fit for

<sup>1</sup> We did not investigate using alternate forms for energy such as  $\sinh aE$ .

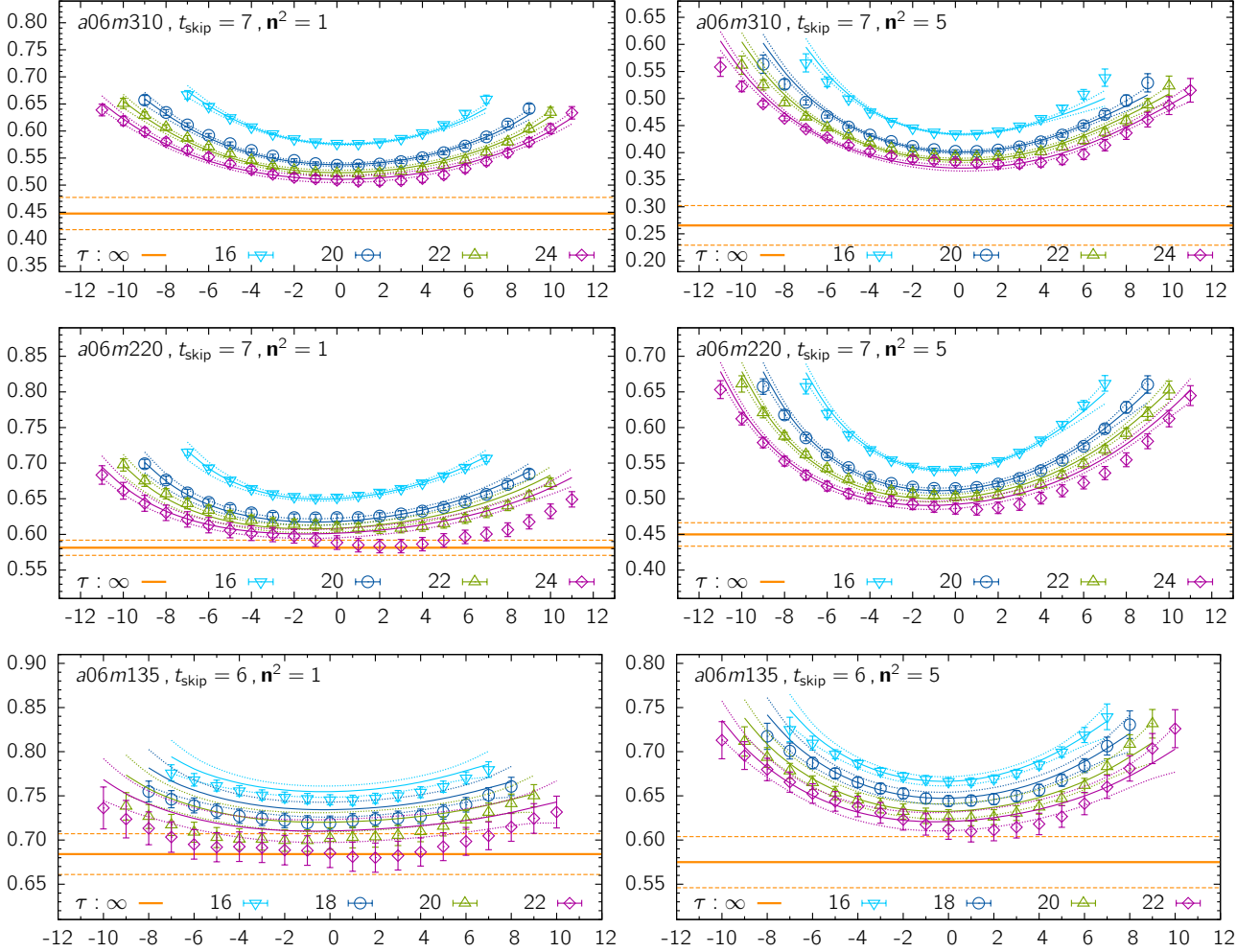


FIG. 2. The three-point data for  $\mathcal{R}_{53}$  defined in Eq. (18) versus the operator insertion time  $t$ , shifted by  $\tau/2$ . The labels give the ensemble ID, the number of points,  $t_{\text{skip}}$ , skipped on either end in the fits, the momentum label  $\mathbf{n}^2$  and the values of  $\tau$  simulated. Prediction of the 2-state fit for various values of the source-sink separation  $\tau$  is shown in the same color as the data. The result for the matrix elements in the  $\tau \rightarrow \infty$  limit is shown by the horizontal band. The plots on the top row are for the  $a06m310$  ensemble, middle row for the  $a06m220$ , and those on the bottom row for the  $a06m135$  ensemble. The plots on the left are for momenta  $\mathbf{p}^2 = \mathbf{n}^2(2\pi/La)^2$  with  $\mathbf{n}^2 = 1$ , while those on the right are with  $\mathbf{n}^2 = 5$ .

various values of  $t_{\text{sep}}$  are also shown as lines with error bands using the same color as the data points. We note that the  $\tau \rightarrow \infty$  estimate for some cases, such as on the  $a09m220$ ,  $a09m130$  and  $a06m310$  ensembles with  $\mathbf{n}^2 = 5$ , is significantly below the data. Fits using only the diagonal elements of the covariance matrix give  $\tau \rightarrow \infty$  results closer to the data. This could reflect that the statistical precision of the covariance matrix is inadequate. However, for consistency, we keep fits using the full covariance matrix in all cases.

We also illustrate how the excited-state contamination impacts the extraction of individual form factors  $G_A$  and  $\tilde{G}_P$  by choosing two channels,  $\mathcal{R}_{51}$  and  $\mathcal{R}_{53}$  with  $q_3 = 0$  but non-zero  $q_1$  or  $q_2$ , that give these directly. The data from the  $a06m135$  ensemble are shown in Fig. 3, while the data from ensembles  $a12m310$ ,  $a06m310$  and  $a06m220$  are given in Figs. 33, 34, 35 in Appendix B.

In these figures, fits to the pseudoscalar form factor, defined in Eq. (22), are also shown where available. For the small  $\mathbf{p}^2$  values, the convergence of the three form factors with respect to  $t_{\text{sep}}$  is from below, i.e., excited state contamination leads to an underestimate. The pattern of convergence changes for higher  $\mathbf{p}^2$ :  $G_A(Q^2)$  starts to converge from above for  $\mathbf{n}^2 \gtrsim 3$ , and  $\tilde{G}_P(Q^2)$  and  $G_P(Q^2)$  for  $\mathbf{n}^2 \gtrsim 10$  as shown in Fig. 3. Also illustrated in Figs. 33, 34, and 35 in Appendix B, the transition  $\mathbf{p}^2$  depends on the pion mass and the value of  $Q^2$  in physical units. Note that these differences in trends in convergence at low and high momenta act cohesively to increase the slope of  $G_A$  and  $\tilde{G}_P$  with respect to  $Q^2$ , and thus the values of  $r_A$  and  $g_P^*$  are larger compared to an analysis neglecting excited state contamination.

The final values of the two form factors,  $G_A(Q^2)$  and  $\tilde{G}_P(Q^2)$ , are extracted by solving the overdetermined

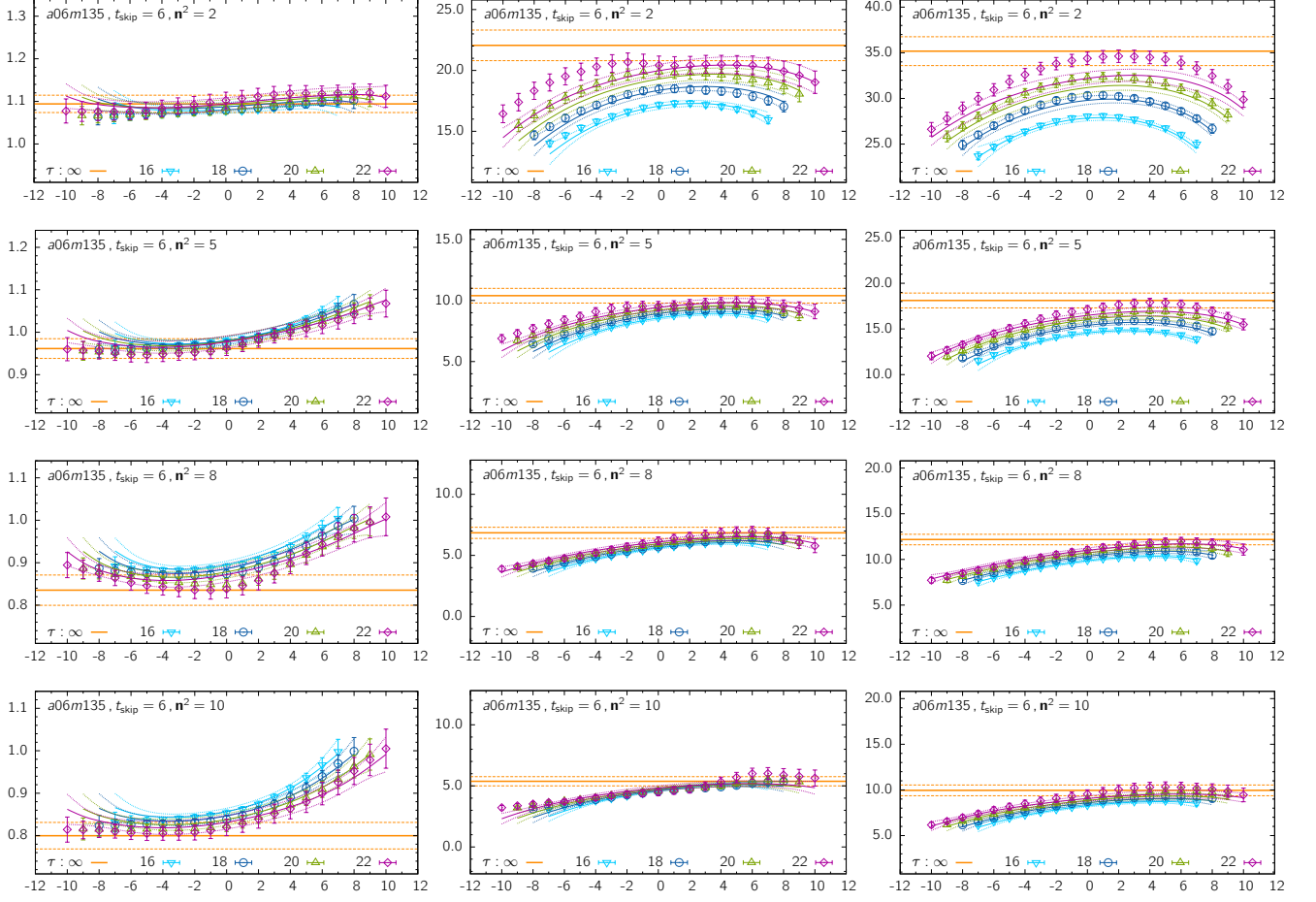


FIG. 3. Plots of the ratios  $\mathcal{R}_i$  that give the three form factors:  $G_A$  from  $\mathcal{R}_{53}$  with  $q_3 = 0$  but  $q_{1,2} \neq 0$  (left),  $\tilde{G}_P$  from  $\mathcal{R}_{51}$  (middle), and the pseudoscalar  $G_P$  from  $\mathcal{R}_5$  (right) versus the operator insertion time  $t$  shifted by  $\tau/2$  for the  $a06m135$  ensemble. The figures in the four rows are for data with  $\mathbf{p}^2 = \mathbf{n}^2(2\pi/La)^2$  where  $\mathbf{n}^2 = 2, 5, 8$ , and  $10$ , respectively.

	$\mathbf{n}^2 = 0$ $G_A$	$\mathbf{n}^2 = 1$ $Q^2$ $G_A(Q^2)$		$\mathbf{n}^2 = 2$ $Q^2$ $G_A(Q^2)$		$\mathbf{n}^2 = 3$ $Q^2$ $G_A(Q^2)$		$\mathbf{n}^2 = 4$ $Q^2$ $G_A(Q^2)$		$\mathbf{n}^2 = 5$ $Q^2$ $G_A(Q^2)$	
$a12m310$	1.270(12)	0.177	1.073(5)	0.344	0.929(8)	0.500	0.823(9)	0.652	0.723(12)	0.796	0.668(10)
$a12m220L$	1.304(20)	0.067	1.211(14)	0.133	1.132(10)	0.197	1.058(9)	0.258	1.007(10)	0.318	0.950(11)
$a09m310$	1.257(38)	0.183	1.073(18)	0.351	0.930(17)	0.522	0.793(23)	0.653	0.730(31)	0.801	0.660(31)
$a09m220$	1.291(44)	0.086	1.178(29)	0.170	1.081(21)	0.250	0.984(21)	0.325	0.918(24)	0.402	0.856(24)
$a09m130$	1.252(21)	0.049	1.193(17)	0.097	1.121(12)	0.145	1.052(11)	0.191	1.004(13)	0.237	0.945(14)
		0.282	0.897(16)			0.370	0.806(19)	0.411	0.783(19)	0.449	0.748(22)
0.407	0.781(22)										
$a06m310$	1.231(25)	0.189	1.018(10)	0.365	0.853(19)	0.532	0.721(30)	0.683	0.635(36)	0.846	0.529(42)
$a06m220$	1.206(14)	0.110	1.098(11)	0.216	0.997(10)	0.318	0.906(11)	0.414	0.845(14)	0.509	0.775(14)
$a06m135$	1.204(24)	0.051	1.136(20)	0.102	1.094(20)	0.152	1.031(26)	0.197	1.005(20)	0.246	0.953(23)
		0.294	0.900(31)			0.383	0.837(35)	0.428	0.793(36)	0.464	0.793(32)
						0.422	0.824(37)				

TABLE III. Results for the unrenormalized axial form factor  $G_A(Q^2)$  obtained from solving the overdetermined set of equations, Eqs. (19)-(21), relating the form factors to the matrix elements as described in the text. We also give the associated momentum transfer  $Q^2$  in units of  $\text{GeV}^2$ . The label  $\mathbf{n}^2 = \sum_i n_i^2$  gives the squared three-momentum in units of  $(2\pi/La)^2$ . The second row for the ensembles  $a09m130$  and  $a06m135$  gives  $G_A(Q^2)$  for momenta  $\mathbf{n}^2 + 5$ . The third row gives  $G_A(Q^2)$  for momentum  $\mathbf{n}^2 = 9$  with  $n_i = (3, 0, 0)$ , while the  $n_i = (2, 2, 1)$  case is given in the second row.

	$\mathbf{n}^2 = 1$	$\mathbf{n}^2 = 2$	$\mathbf{n}^2 = 3$	$\mathbf{n}^2 = 4$	$\mathbf{n}^2 = 5$
$a12m310$	15.67(31)	9.08(20)	6.10(14)	4.18(10)	3.35(8)
$a12m220L$	31.21(2.32)	20.79(1.56)	15.51(1.10)	12.27(83)	9.79(57)
$a09m310$	15.21(82)	8.53(32)	5.79(31)	4.00(41)	2.99(31)
$a09m220$	25.43(2.12)	16.57(1.46)	12.57(1.16)	9.50(75)	7.73(53)
$a09m130$	37.93(1.84) 9.62(28)	23.66(99)	17.57(70) 7.06(18)	14.19(52) 6.35(18)	11.21(35) 5.45(16) 6.25(19)
$a06m310$	14.41(53)	8.16(27)	5.25(20)	3.78(19)	2.73(16)
$a06m220$	19.94(45)	12.30(26)	8.60(20)	6.68(18)	5.25(13)
$a06m135$	31.88(1.19) 8.82(36)	22.00(82)	16.24(69) 6.88(34)	13.05(43) 5.79(26)	10.44(41) 5.42(27) 6.19(31)

TABLE IV. Results for the unrenormalized induced pseudoscalar form factor  $\tilde{G}_P(Q^2)$ . The values of  $Q^2$  for the various values of  $\mathbf{n}^2 = \sum_i n_i^2$  and other details are the same as given in Table III.

	$\mathbf{n}^2 = 1$	$\mathbf{n}^2 = 2$	$\mathbf{n}^2 = 3$	$\mathbf{n}^2 = 4$	$\mathbf{n}^2 = 5$
$a12m310$	19.24(41)	11.65(25)	8.06(18)	6.15(17)	4.84(11)
$a09m130$	54.12(3.00) 15.78(63)	36.58(1.92)	27.81(1.41) 11.98(41)	22.05(1.00) 10.75(38)	18.33(76) 9.34(32) 10.67(38)
$a06m220$	28.00(74)	18.06(44)	13.13(35)	10.11(30)	8.13(21)
$a06m135$	51.44(1.72) 15.55(58)	35.21(1.23)	26.77(95) 12.19(50)	21.18(77) 10.77(48)	18.11(66) 9.94(53) 10.89(58)

TABLE V. Results for the unrenormalized pseudoscalar form factor  $G_P(Q^2)$  obtained from the matrix element of the pseudoscalar operator  $\bar{\psi}\gamma_5\psi$  between nucleon states. The values of  $Q^2$  for the various values of  $\mathbf{n}^2 = \sum_i n_i^2$  and other details are the same as given in Table III.

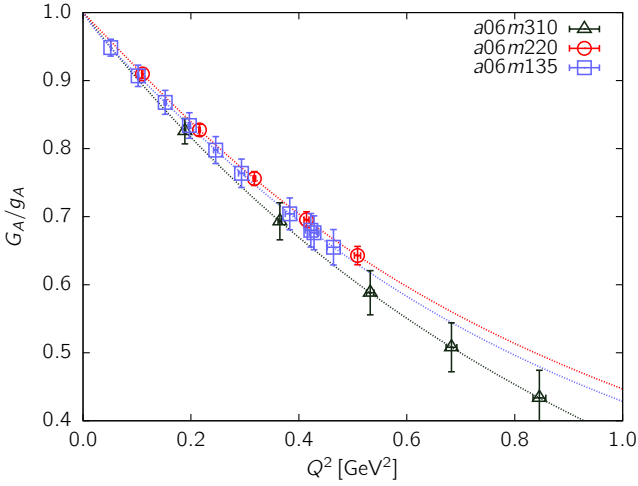
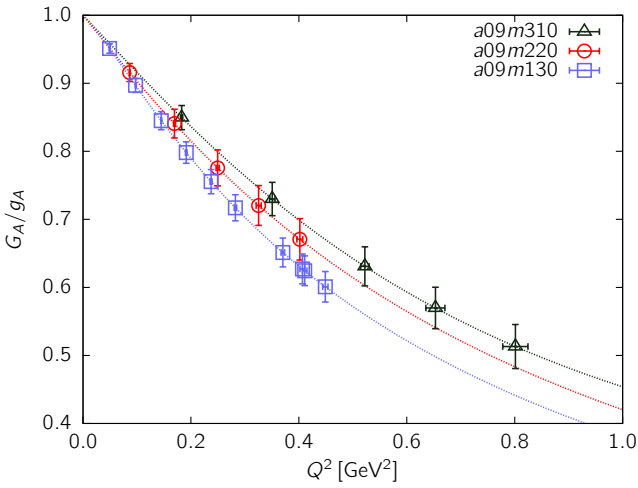
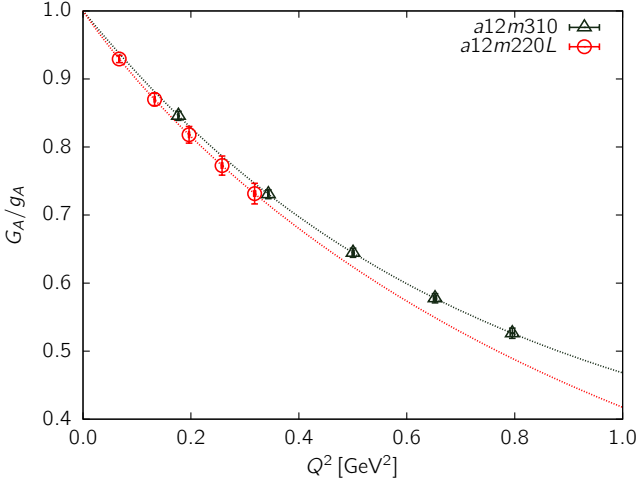


FIG. 4. The data for the normalized axial form factor  $G_A(Q^2)/g_A$  versus  $Q^2$  plotted to highlight the dependence on  $M_\pi^2$  for fixed  $a$ . The top figure is for the  $a \approx 0.12$  fm ensembles, the middle for the  $a \approx 0.09$  fm ensembles, and the bottom for the  $a \approx 0.06$  fm ensembles. We also show the  $z^{3+4}$  fit to the data for each ensemble; the corresponding value of  $r_A$  obtained from the slope at  $Q^2 = 0$  is given in Table VI. The color scheme used is black for the  $M_\pi \approx 310$ , red for  $M_\pi \approx 220$ , and purple for the  $M_\pi \approx 130$  MeV ensembles.

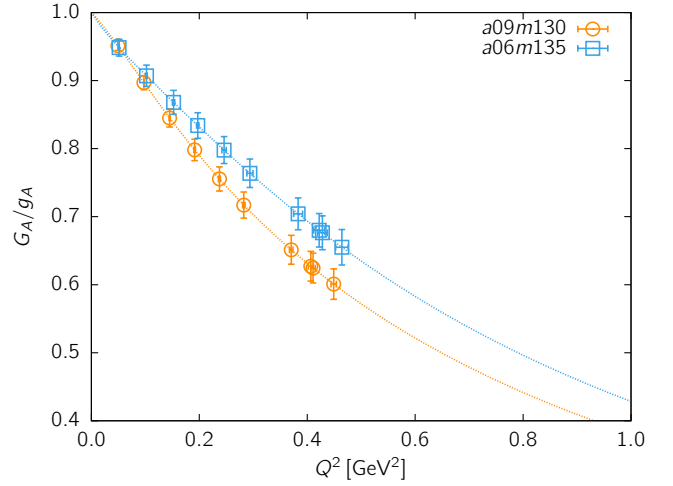
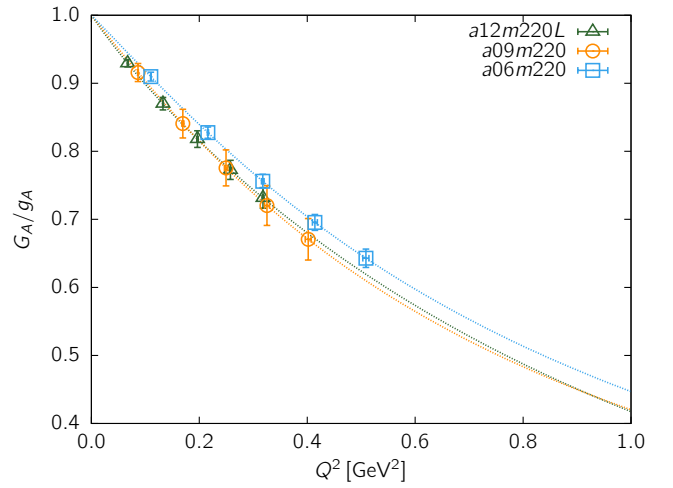
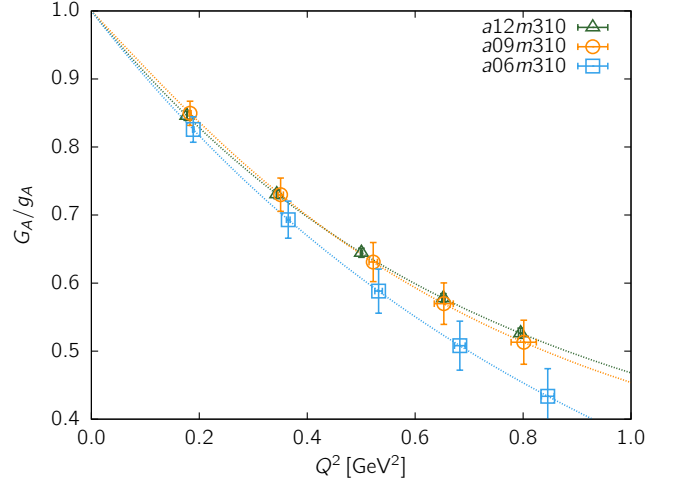


FIG. 5. The same data and fits for the normalized axial form factor  $G_A(Q^2)/g_A$  versus  $Q^2$  as shown in Fig. 4 but plotted to highlight the dependence on  $a$  for fixed  $M_\pi$ . The top figure is for the  $M_\pi \approx 310$  MeV ensembles, the middle for the  $M_\pi \approx 220$  MeV ensembles, and the bottom for the  $M_\pi \approx 130$  MeV ensembles. The color scheme used is green for the  $a \approx 0.12$ , orange for  $a \approx 0.09$  and blue for the  $a \approx 0.06$  fm ensembles.

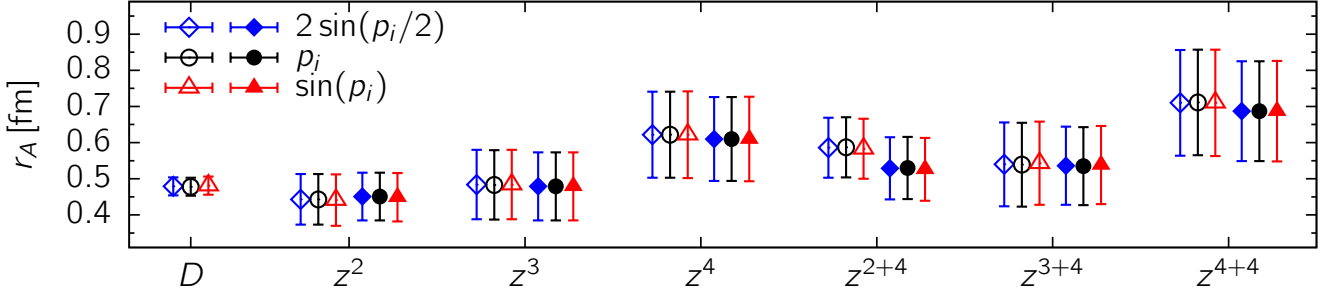


FIG. 6. Comparison of results for  $r_A$  obtained using three possible definitions of lattice momenta. For the six  $z$ -expansion fits we also show variation of estimates between the two values of  $\bar{t}_0$ :  $\bar{t}_0 = 0$  shown using open symbols and  $\bar{t}_0 = \bar{t}_0^{\text{mid}} = 0.12 \text{ GeV}^2$  with filled symbols. The label D stands for the dipole ansatz. The data are from the  $a06m135$  ensemble.

set of Eqs. (19)–(21) for each momentum  $Q^2$ . These results for  $G_A(Q^2)$  are given in Table III, and those for  $\tilde{G}_P(Q^2)$  in Table IV. The data for the pseudoscalar form factor, calculated from the matrix element of the operator  $\bar{u}\gamma_5 d$  using Eq. (22), are given in Table V for the four ensembles analyzed,  $a12m310$ ,  $a09m130$ ,  $a06m220$ , and  $a06m135$ . The values for the PCAC mass, determined from the pion two-point correlation functions, are  $\hat{m}a = a(m_u + m_d)Z_m Z_P / 2Z_A = 0.012119(18)$ ,  $0.0015383(39)$ ,  $0.0027984(23)$  and  $0.0008840(18)$ , respectively. The difference from the corresponding values for the HISQ light quarks,  $(m_u + m_d)/2 = 0.0102$ ,  $0.0012$ ,  $0.0024$  and  $0.00084$  [12], used in the generation of the ensembles, can be attributed to the factor  $Z_m Z_P / Z_A$  in the clover formalism, which is unity for HISQ.

Results for  $G_A(Q^2)$  are plotted as a function of  $Q^2$  in Figs. 4 and 5. The data in Fig. 4 are organized to exhibit the dependence on the light quark mass (equivalently,  $M_\pi^2$ ) for fixed lattice spacing, while Fig. 5 highlights the variation versus the lattice spacing  $a$  for fixed pion mass  $M_\pi$ . We also show the  $z$ -expansion fit  $z^{3+4}$ , discussed in Sec. VI, which is used in obtaining the final estimate of  $r_A$ . The data in Fig. 4 show weak dependence on the light quark mass for fixed  $a$  on all ensembles but the  $a09m130$  ensemble, for which they are a little lower, and give a slightly larger  $r_A$ . The trend in the data versus the lattice spacing  $a$  in Fig. 5 is a small decrease with  $a$  for the  $M_\pi = 310$  ensembles, but is reversed in the  $M_\pi \approx 220$  and 130 MeV data, suggesting that higher precision data are needed to establish a possible trend.

## VI. FITS TO EXTRACT THE AXIAL CHARGE RADIUS

The data for  $G_A(Q^2)$ , given in Table III, are fit using seven ansatz to parameterize the  $Q^2$  behavior: the dipole approximation given in Eq. (5); the  $z^2$ ,  $z^3$  and  $z^4$  truncation of the  $z$ -expansion given in Eq. (8); and these three truncations of the  $z$ -expansion supplemented with the four sum rule constraints given in Eq. (10) and labeled  $z^{2+4}$ ,  $z^{3+4}$  and  $z^{4+4}$ . From these fits we extract the axial charge radius squared,  $r_A^2$ , using Eq. (4).

In the analyses using the  $z$ -expansion, we first investigated the sensitivity of the fits on the choice of  $\bar{t}_0$  in the definition of  $z$  and on the three choices for momenta,  $f_i = ap_i$ ,  $\sin(ap_i)$  and  $2\sin(ap_i/2)$ , in evaluating  $Q^2$ . The quality of the fits and the results for  $r_A$  are indistinguishable between the three choices of  $f_i$  and between  $\bar{t}_0 = 0$  and the approximate mid-point of  $Q^2$  range, which we call  $\bar{t}_0^{\text{mid}}$ . We illustrate this insensitivity using the data from the  $a06m135$  ensemble, that has the largest number of  $Q^2$  values, in Fig. 6. The same pattern is seen in all eight ensembles. Also, the fits in  $z$  with and without using the sum rules, for example,  $z^2$  versus  $z^{2+4}$ , give consistent results for  $r_A$ , however, as expected, the large  $Q^2$  behavior is much more reasonable with fits including the sum rules.

For our final results we use fits with  $f_i = ap_i$ , the mid-point value,  $\bar{t}_0^{\text{mid}}$  as it minimizes  $z_{\text{max}}$ , and include the sum rules in the  $z$ -expansion. These fits to  $G_A(Q^2)$  versus  $Q^2$  for the eight ensembles are shown in Fig. 7. The labels give the estimates of  $r_A$  from the seven fit ansatz along with the  $\chi^2/\text{d.o.f.}$  within square brackets.<sup>2</sup> The resulting values of  $r_A$  from the seven fits are collected together in Table VI. Overall, the dipole ansatz does a remarkably good job of fitting the data as shown in Fig. 7.

We find that these estimates of  $r_A$  from the seven ansatz are, in most cases, consistent within the  $1\sigma$  combined statistical and fit uncertainty and show little dependence on the lattice spacing or the pion mass. The solid and dashed orange lines in Fig. 7 show that the  $k^4$  and the  $k^{4+4}$  fits, which have only one degree of freedom, and in many cases have a large curvature that becomes manifest outside the range of the data. For this reason, we do not include these ansatz in our final estimates.

<sup>2</sup> Fits to the ratio  $G_A(Q^2)/G_A(Q^2 = 0)$  give essentially identical results for  $r_A$  in all cases.

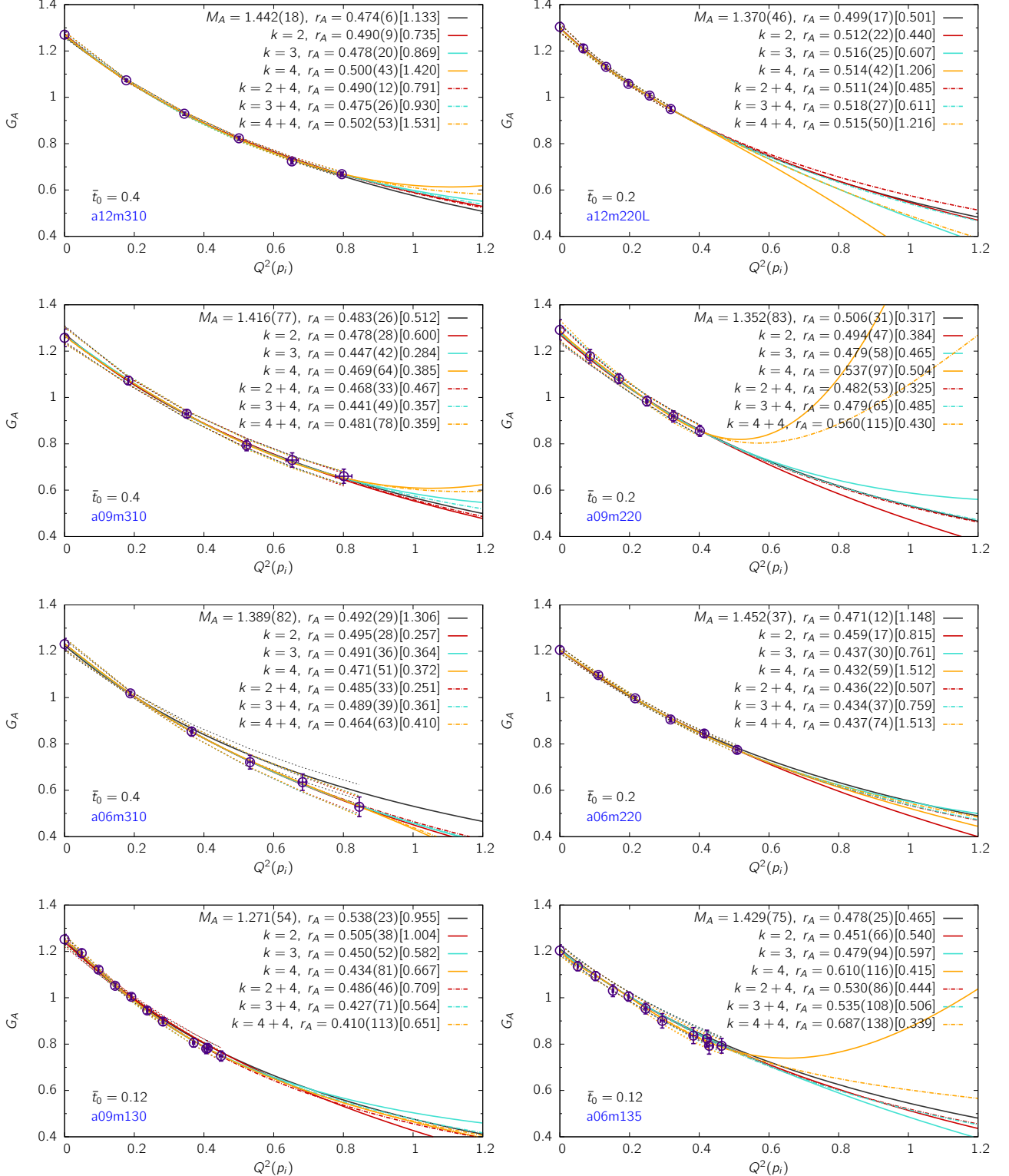


FIG. 7. Fits to the unrenormalized  $G_A(Q^2)$  data (circles) versus  $Q^2$  ( $\text{GeV}^2$ ) for the eight ensembles. The top two panels show data and fits for the  $a12m310$  and  $a12m220L$  ensembles; the second row for  $a09m310$  and  $a09m220$ ; the third row for  $a06m310$  and  $a06m220$ ; and the final row for the two physical mass ensembles  $a09m130$  and  $a06m135$ . The axial radius  $r_A$  is extracted from these fits using Eq. (4). Estimates of the mass  $M_A$  from the dipole fit and the axial radius  $r_A$  from the various fits are given in the labels. The number within the square brackets is the  $\chi^2/\text{d.o.f.}$  of the fit.

Ensemble	Dipole	$z^2$	$z^{2+4}$	$z^3$	$z^{3+4}$	$z^4$	$z^{4+4}$
$a12m310$	0.225(05)	0.240(09)	0.240(12)	0.228(19)	0.225(24)	0.250(43)	0.252(53)
$a12m220L$	0.249(17)	0.262(23)	0.261(24)	0.267(26)	0.268(28)	0.264(43)	0.265(51)
$a09m310$	0.233(25)	0.229(27)	0.219(31)	0.200(38)	0.195(43)	0.220(60)	0.231(75)
$a09m220$	0.256(31)	0.244(47)	0.232(52)	0.230(56)	0.230(63)	0.288(10)	0.314(129)
$a09m130$	0.289(24)	0.255(38)	0.236(45)	0.202(47)	0.183(61)	0.188(70)	0.168(93)
$a06m310$	0.242(29)	0.245(28)	0.235(32)	0.241(35)	0.239(38)	0.222(48)	0.215(58)
$a06m220$	0.222(11)	0.211(15)	0.190(19)	0.191(26)	0.188(32)	0.187(51)	0.191(65)
$a06m135$	0.229(24)	0.204(59)	0.281(91)	0.229(90)	0.287(116)	0.373(141)	0.473(190)
$a12m310$	0.474(06)	0.490(09)	0.490(12)	0.478(20)	0.475(26)	0.500(43)	0.502(53)
$a12m220L$	0.499(17)	0.512(22)	0.511(24)	0.516(25)	0.518(27)	0.514(42)	0.515(50)
$a09m310$	0.483(26)	0.478(28)	0.468(33)	0.447(42)	0.441(49)	0.469(64)	0.481(78)
$a09m220$	0.506(31)	0.494(47)	0.482(53)	0.479(58)	0.479(65)	0.537(97)	0.560(115)
$a09m130$	0.538(23)	0.505(38)	0.486(46)	0.450(52)	0.427(71)	0.434(81)	0.410(113)
$a06m310$	0.492(29)	0.495(28)	0.485(33)	0.491(36)	0.489(39)	0.471(51)	0.464(63)
$a06m220$	0.471(12)	0.459(17)	0.435(23)	0.436(31)	0.434(37)	0.432(60)	0.437(76)
$a06m135$	0.478(25)	0.451(66)	0.530(86)	0.479(94)	0.535(108)	0.610(116)	0.687(138)

TABLE VI. The upper half of the table lists the isovector axial radius squared,  $\langle r_A^2 \rangle$  in units of fm<sup>2</sup>, obtained from the dipole and six different  $z$ -expansion fits ( $z^2$ ,  $z^{2+4}$ ,  $z^3$ ,  $z^{3+4}$ ,  $z^4$ , and  $z^{4+4}$ ) to the form factor  $G_A(Q^2)$ . The fits  $z^{2+4}$ ,  $z^{3+4}$ , and  $z^{4+4}$  include the four sumrule constraints given in Eq. (10). For convinience, the bottom half of the table gives the radius,  $r_A$ , in units of fm.

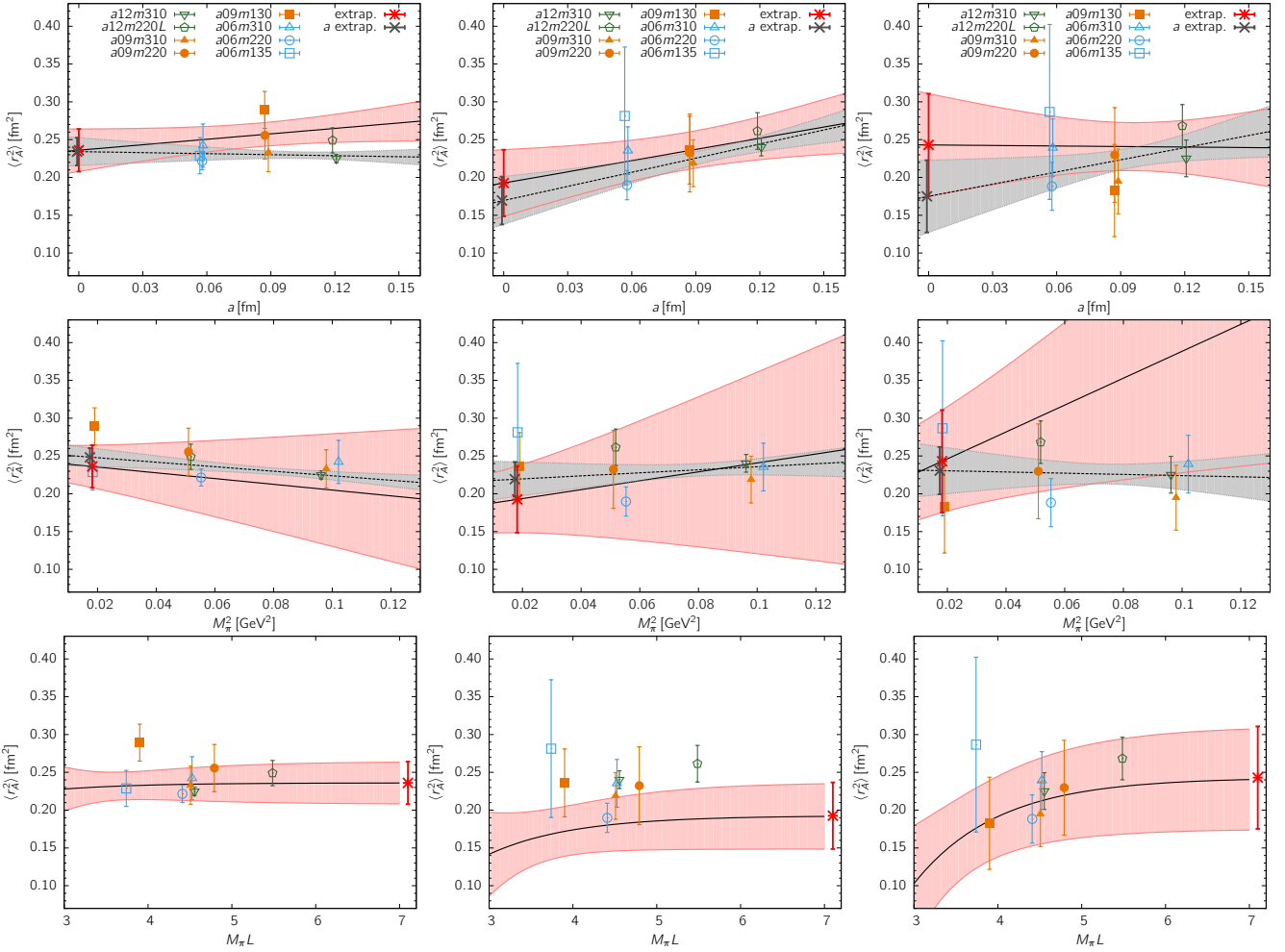


FIG. 8. The 8-point fit using the extrapolation ansatz Eq. (23) to the data for the axial radius squared  $\langle r_A^2 \rangle$ . Each panel shows the fit versus a single variable after the data have been extrapolated to the physical point in the other two variables. The top row shows plots versus  $a$ , the middle versus  $M_\pi^2$ , and the bottom row versus  $M_\pi L$ . Each row shows  $r_A$  extrapolated using the dipole ansatz (left); the  $z^{2+4}$  ansatz (middle); and the  $z^{3+4}$  ansatz (right). The extrapolated values are shown using the symbol red star. The overlaid grey bands in the upper (middle) row are fits to the single variable  $a$  ( $M_\pi^2$ ), i.e., ignoring possible dependence on the other two variables.

## VII. CONTINUUM, CHIRAL AND FINITE VOLUME EXTRAPOLATION OF $\langle r_A^2 \rangle$

To obtain results for the axial charge radius squared,  $\langle r_A^2 \rangle$ , in the limits  $a \rightarrow 0$ ,  $M_\pi \rightarrow 135$  MeV and  $M_\pi L \rightarrow \infty$ , we extrapolate the data for  $\langle r_A^2 \rangle$  given in Table VI and not the form factors themselves. Since the  $Q^2$  are different for each ensemble a more comprehensive fit including dependence on  $Q^2$  requires higher precision data. Using the eight data points, including the two physical mass points, we make a simultaneous fit in the three variables  $a$ ,  $M_\pi^2$  and the lattice size  $M_\pi L$  keeping only the lowest order correction term in each [25]

$$r_A^2(a, M_\pi, L) = c_1 + c_2 a + c_3 M_\pi^2 + c_4 M_\pi^2 e^{-M_\pi L}. \quad (23)$$

A comparison of these “8-point” extrapolation fits using the  $z$ -expansion and dipole ansatz data are shown

in Fig. 8. We do not show the two free parameter  $z^{1+4}$  fits as the  $\chi^2/\text{d.o.f.}$  are not good. The  $z^{4+4}$  fits, with only one degree of freedom, are questionable outside the range of  $Q^2$  values simulated, nevertheless, the data in Table VI show that they give values for  $\langle r_A \rangle$  that are consistent with the other fits. The error estimates, on the other hand, grow steadily between the  $z^{2+4}$  and the  $z^{4+4}$  cases.

The variation versus  $a$ ,  $M_\pi$  or  $M_\pi L$  for the results from the dipole,  $z^{2+4}$  and  $z^{3+4}$  fits are shown in Fig. 8. The least well-determined coefficient is the finite volume correction term,  $c_4$  in Eq. (23), which is consistent with zero. We, therefore, show the extrapolation with  $c_4 = 0$  in Fig. 9. The results of fits, with and without the  $c_4$ , are summarized in Table VII, and show that neglecting the finite volume correction term  $c_4$  does not significantly change the results, but on comparing Figs. 8 and 9 we find

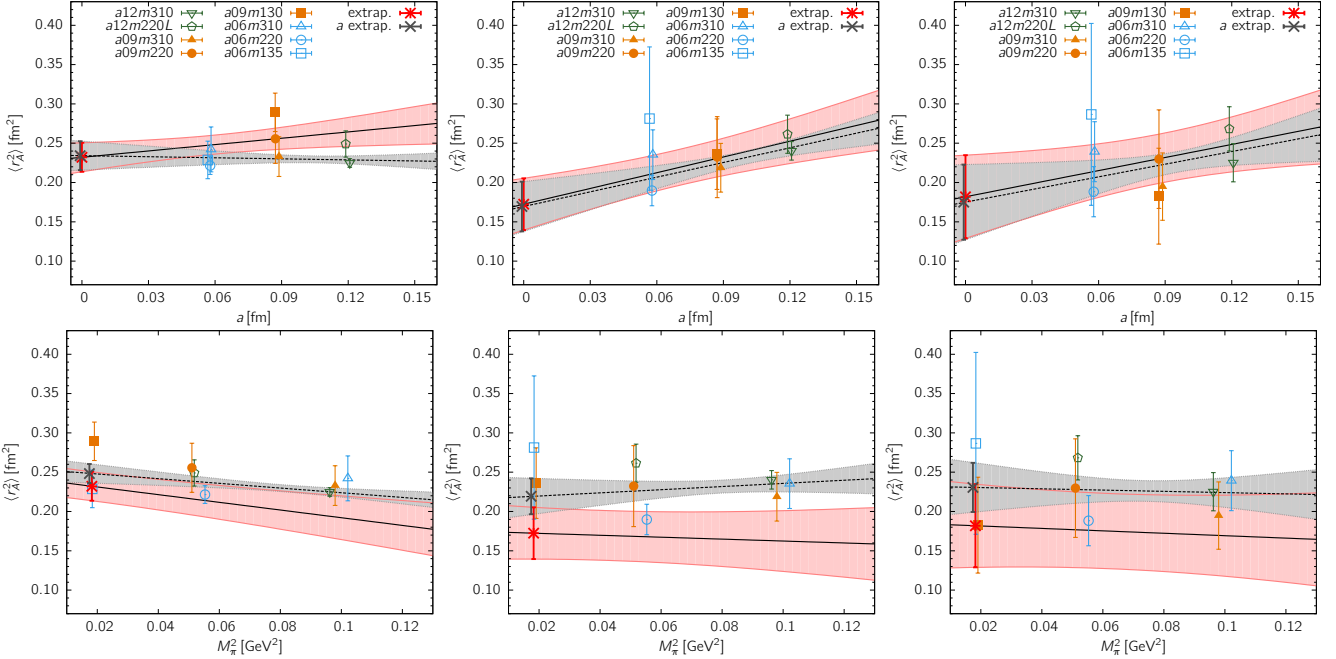


FIG. 9. The 8-point fit using Eq. (23) without the finite volume correction ( $c_4 = 0$ ) to the data for the axial radius squared  $\langle r_A^2 \rangle$ . The overlaid grey bands in the upper (bottom) row are fits to the single variable  $a$  ( $M_\pi^2$ ), i.e., ignoring possible dependence on the other variable. The rest is the same as in Fig 8.

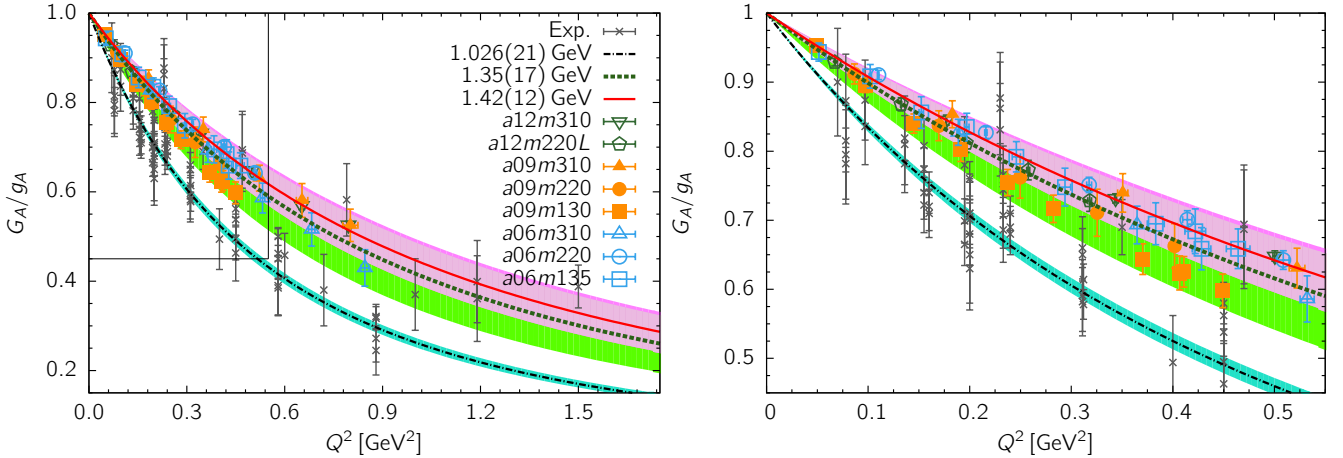


FIG. 10. (Left) The data for  $G_A(Q^2)/g_A$  from the eight ensembles is plotted versus  $Q^2$  ( $\text{GeV}^2$ ). We also show the dipole fit with the phenomenological estimates of the axial mass,  $\mathcal{M}_A = 1.026(21)$  GeV [13] (turquoise band), the miniBoone value  $\mathcal{M}_A = 1.35(17)$  GeV (green band), and our combined estimate  $\mathcal{M}_A = 1.42(12)$  GeV (magenta band) corresponding to  $r_A|_{\text{dipole}} = 0.49(3)$  given in Eq. (24). The experimental data, reproduced from Ref. [13], were provided by Ulf Meissner. (Right) A magnified view of the data and the three dipole fits in the region  $Q^2 < 0.5$   $\text{GeV}^2$ .

that the uncertainty versus  $M_\pi^2$  is reduced on neglecting  $c_4$ . Overall, the results of the simultaneous fits to data obtained using the three ansatz are consistent. In Figs. 8 and 9, we also show fits versus a single variable ( $a$  or  $M_\pi^2$ ) as a grey band. Given the weak dependence on  $a$ ,  $M_\pi$  or  $M_\pi L$ , they give estimates that are consistent with results of the simultaneous fits but with smaller uncertainty.

Our final estimates, using the data summarized in Ta-

ble VII for the case  $c_4 \neq 0$ , are

$$\begin{aligned}
 r_A|_{\text{dipole}} &= 0.49(3) \text{ fm}, \\
 r_A|_{z-\text{expansion}} &= 0.46(6) \text{ fm}, \\
 r_A|_{\text{combined}} &= 0.48(4) \text{ fm}, \\
 \mathcal{M}_A|_{\text{dipole}} &= 1.39(9) \text{ GeV}, \\
 \mathcal{M}_A|_{z-\text{expansion}} &= 1.48(19) \text{ GeV}, \\
 \mathcal{M}_A|_{\text{combined}} &= 1.42(12) \text{ GeV}.
 \end{aligned} \tag{24}$$

	Eq. (23)			Eq. (23) with $c_4 = 0$		
	$\langle r_A^2 \rangle$	$r_A$	$\mathcal{M}_A$	$\langle r_A^2 \rangle$	$r_A$	$\mathcal{M}_A$
dipole	0.24(3)	0.49(3)	1.41(08)	0.23(2)	0.48(2)	1.42(06)
$z^{2+4}$	0.19(4)	0.44(5)	1.56(18)	0.17(3)	0.42(4)	1.65(16)
$z^{3+4}$	0.24(7)	0.49(7)	1.39(19)	0.18(5)	0.43(6)	1.60(23)

TABLE VII. Results for  $\langle r_A^2 \rangle$  in units of  $\text{fm}^2$  after extrapolation to  $a \rightarrow 0$ ,  $M_\pi = 135$  MeV, and  $M_\pi L \rightarrow \infty$  using Eq. (23). We also give the corresponding  $r_A$  in units of fm and  $\mathcal{M}_A$  in units of GeV. The last three columns show results obtained by neglecting the finite volume correction term, i.e.,  $c_4 = 0$ .

The second two estimates are obtained by performing an average using the prescription for optimal correlation given in Ref. [31]. For the  $z$ -expansion data, we have averaged the  $z^{2+4}$  and the  $z^{3+4}$  estimates with the lattice size correction term,  $c_4$ , included. The  $r_A|_{\text{combined}}$  result is then obtained by averaging this  $z$ -expansion estimate with the dipole result. As remarked previously, the dipole ansatz fits our data remarkably well and the final result is close to it.

In Fig. 10, we plot the data for  $G_A(Q^2)$  from all eight ensembles and compare them against a dipole fit using two different estimates for the axial mass: the phenomenological value  $\mathcal{M}_A = 1.026(17)$  GeV obtained from the combined neutrino scattering and electroproduction data [13], and the value 1.35(17) used by the mini-BooNE Collaboration to fit their [anti]-neutrino cross-section data [9]. We also reproduce the data in Ref. [13] (provided by Ulf Meissner) that was used to obtain the estimate  $\mathcal{M}_A = 1.026(17)$  GeV. It is clear that the lattice data for  $G_A(Q^2)$  show little variation with the lattice spacing or the pion mass, and prefer the larger values of  $\mathcal{M}_A$  as shown in Table VI. The MiniBooNE value  $\mathcal{M}_A = 1.35(17)$  covers the spread in the lattice data, and our result  $\mathcal{M}_A = 1.42(12)$  GeV is consistent with it. However, the bands showing our and MiniBooNE results lie above most of the earlier experimental data for the form factor, and the corresponding values of  $\mathcal{M}_A$  are larger than the phenomenological value, given in Eq. (6), extracted from the experimental data.

Two recent lattice QCD calculations give

$$\begin{aligned} \mathcal{M}_A|_{\text{dipole}} &= 1.32(7) \text{ GeV} & (\text{ETMC}), \\ \mathcal{M}_A|_{z-\text{expansion}} &= 1.14(15) \text{ GeV} & (\text{Mainz}), \end{aligned} \quad (25)$$

where the first number is from the ETMC collaboration [32] who use a dipole fit and analyze a single  $N_f = 2$  twisted mass ensemble with  $M_\pi \approx 130$  MeV and  $a = 0.093$  fm. The second number is from the Mainz collaboration [33] who use the  $z$ -expansion method on  $N_f = 2$  ensembles generated by the CLS collaboration. Ensemble by ensemble, their data, which in in all but one case have been obtained with  $M_\pi > 260$  MeV, are consistent with what we find. The difference in the final results is a consequence of their final extrapolation in  $M_\pi \rightarrow 135$  MeV. Our data at  $M_\pi \approx 220$  and  $\approx 135$  MeV, and that by the ETMC collaboration at  $M_\pi \approx 130$  MeV, do not support

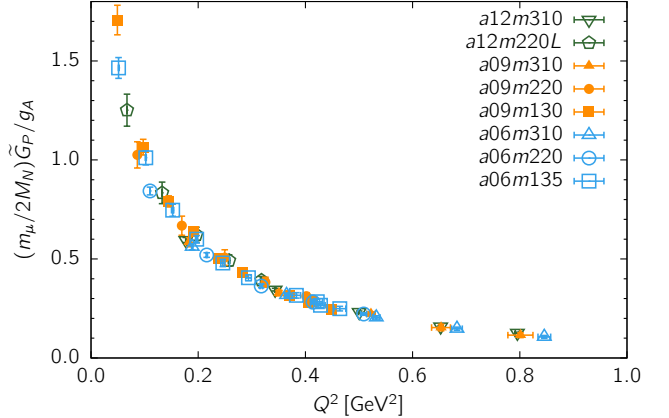


FIG. 11. The data for  $(m_\mu/2M_N)G_P(Q^2)/g_A$  from the eight ensembles is plotted versus  $Q^2$  in units of  $\text{GeV}^2$ . They show little dependence on the lattice spacing  $a$  or the pion mass  $M_\pi$ .

the large increase in  $r_A$  from their data to their value after extrapolation in  $M_\pi$ .

### VIII. ANALYSIS OF THE INDUCED PSEUDOSCALAR FORM FACTOR $\tilde{G}_P(Q^2)$

The data for the normalized induced pseudoscalar form factor  $(m_\mu/2M_N)\tilde{G}_P(Q^2)/g_A$  versus  $Q^2$  from the eight ensembles is summarized in Figs. 11 and 12. Overall, the data show remarkably little dependence on the pion mass or the lattice spacing.

The traditional starting point of the analysis of the  $Q^2$  behavior of  $\tilde{G}_P(Q^2)$  data given in Table IV is the pion pole-dominance ansatz given in Eq. (11). In Fig. 13, we show the data for  $(Q^2 + M_\pi^2)\tilde{G}_P(Q^2)/(4M_\pi^2 G_A(Q^2))$ , which should be unity, versus  $Q^2$  from all eight ensembles. We find that it tends to unity for  $Q^2 \gtrsim 0.5 \text{ GeV}^2$ . At low  $Q^2$ , however, there are significant deviations suggesting that corrections to the pion pole-dominance ansatz are large for  $Q^2 \lesssim 0.2 \text{ GeV}^2$ , precisely in the region in which it is expected to work best. Very similar behavior was reported in Ref. [34].

To further evaluate the pion pole-dominance ansatz, we exhibit the dependence of  $(m_\mu/2M_N)G_P(Q^2)/g_A$  on  $M_\pi^2$  for fixed  $a$  in Fig. 12 (left column), and on  $a$  for fixed  $M_\pi^2$  (right column). These plots also show a fit using the simplest small  $Q^2$  expansion of Eq. (26) [34],

$$\frac{m_\mu}{2M_N} \frac{\tilde{G}_P(Q^2)}{g_A} = \frac{c_1}{M_\pi^2 + Q^2} + c_2 + c_3 Q^2, \quad (26)$$

where the leading term is the pion-pole term and the polynomial approximates the small  $Q^2$  expansion of the dipole or the  $z$ -expansion ansatz for  $G_A$ . It is also the behavior predicted for small  $Q^2$  and  $M_\pi^2$  by the leading

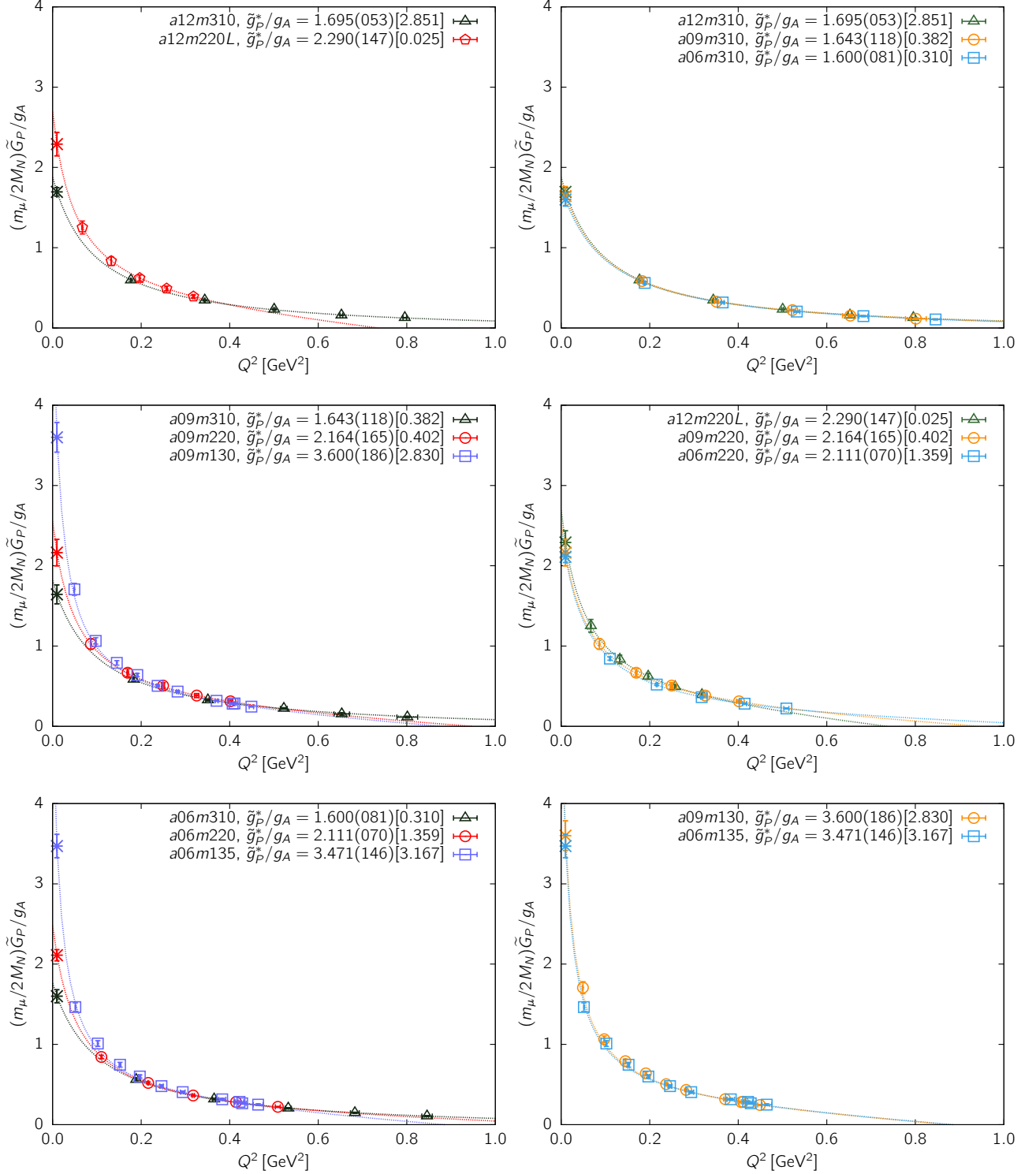


FIG. 12. The data for the induced pseudoscalar form factor  $(m_\mu/2M_N)\tilde{G}_P(Q^2)/g_A$  versus  $Q^2$  in units of  $\text{GeV}^2$ . The left column highlights the dependence on  $M_\pi^2$  for fixed  $a$ . The top panel is for the  $a \approx 0.12$  fm, the middle for the  $a \approx 0.09$  fm, and the bottom for the  $a \approx 0.06$  fm ensembles. The right column highlights the dependence on  $a$  for fixed  $M_\pi$ . The top panel is for the  $M_\pi \approx 310$  MeV, the middle for the  $M_\pi \approx 220$  MeV, and the bottom for the  $M_\pi \approx 130$  MeV ensembles. The fits are made using Eq. (26) with lattice estimates for the axial charge  $g_A$  and nucleon mass  $M_N$ . The muon mass is  $m_\mu = 0.10566$  GeV. The number within the square brackets in the labels is the  $\chi^2/\text{d.o.f.}$  of the fit.

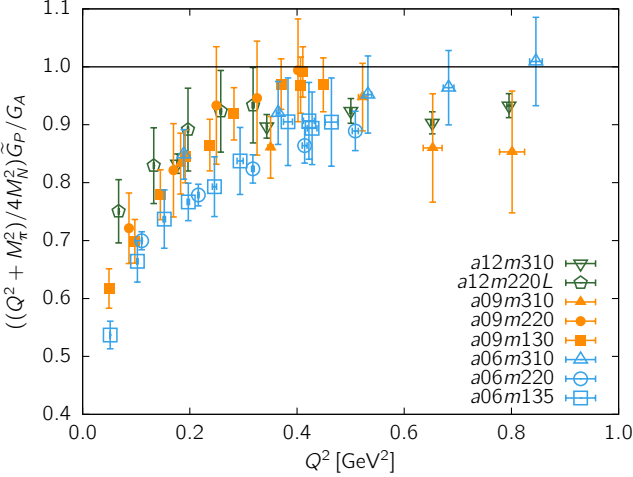


FIG. 13. Plot of the ratio  $(Q^2 + M_\pi^2)\tilde{G}_P(Q^2)/(4M_p^2G_A(Q^2))$  versus  $Q^2$  for the eight ensembles. Validity of the pion pole-dominance hypothesis, given in Eq. (11), requires that this ratio is unity for all  $Q^2$ . Our data show significant deviations, especially for  $Q^2 \lesssim 0.2$  GeV $^2$ .

order chiral perturbation theory [13].<sup>3</sup> We use lattice estimates for the axial charge  $g_A$  given in the Table III, the nucleon mass  $M_N$  from Tables XI–XVIII, and the muon mass is  $m_\mu = 0.10566$  GeV. The values of the fit parameters  $c_1$ ,  $c_2$  and  $c_3$ , defined in Eq. (26), are given in Table VIII. Pion pole-dominance implies that the contribution of terms proportional to  $c_2$  and  $c_3$  is relatively small. The data in Table VIII show that both  $c_2$  and  $c_3$  grow as  $M_\pi$  is decreased, signaling that the pion pole-dominance ansatz has large and growing corrections. This change in behavior is exhibited in the Fig. 14; as  $M_\pi$  decreases and contribution of the quadratic term becomes larger.

For each ensemble, the result for  $g_P^*$ , defined in Eq. (12) and obtained from the fit, is given in Fig. 12 and in the third column of Table VIII. We find that the estimates from the physical pion mass ensembles are about half the values obtained from the muon capture experiment or the  $\chi$ PT analysis given in Eq. (13). It is, therefore, important to understand how and where the analysis based on the pion pole-dominance ansatz, Eq. (11), breaks down.

To do this, we start with the axial Ward identity Eq. (3) rewritten as

$$\frac{Q^2}{4M_N^2} \frac{\tilde{G}_P(Q^2)}{G_A(Q^2)} + \frac{2\hat{m}}{2M_N} \frac{G_P(Q^2)}{G_A(Q^2)} = 1. \quad (27)$$

This PCAC relation has to hold for each  $Q^2$  and  $M_\pi$  up to corrections starting at  $O(a)$  for the lattice action and operators used by us. If the  $O(a)$  improved axial current

$A_\mu^I = Z_A(1+b_Ama)(A_\mu + c_Aa\partial_\mu P)$  is used, then Eq. (27) is modified to

$$\frac{Q^2}{4M_N^2} \frac{\tilde{G}_P^I(Q^2)}{G_A(Q^2)} + \frac{2\hat{m}}{2M_N} \frac{G_P(Q^2)}{G_A(Q^2)} = 1. \quad (28)$$

where  $\tilde{G}_P^I(Q^2) = \tilde{G}_P(Q^2) + 2M_N a c_A G_P$ . Note that the extraction of  $G_A(Q^2)$  is unchanged because the improvement term contributes only to  $\tilde{G}_P$ . Also, there is no  $O(a)$  correction to the pseudoscalar density [35]. Typical estimates of the improvement coefficient are  $c_A \lesssim -0.05$  [36], and based on the values given there, we take these to be  $c_A = -0.05$ ,  $-0.04$  and  $-0.03$  for the  $a = 0.12$ ,  $0.09$  and  $0.06$  fm ensembles, respectively, for the purpose of the test. In the following discussion of tests of the PCAC relation, we also ignore the differences in the mass dependent corrections  $(1 + b_i ma)$  to the renormalization constants  $Z_i$  ( $i \in m, A, P$ ) as these are small ( $ma < 0.01$ ) compared to the effects under consideration.

The PCAC relation reduces to the pion pole-dominance ansatz given in Eq. (11) provided the relation

$$2\hat{m} G_P(Q^2) = (M_\pi^2/2M_N) \tilde{G}_P^{[I]}(Q^2) \quad (29)$$

also holds up to corrections starting at  $O(a)$ . Validation of both the PCAC relation and the pion pole-dominance ansatz implies that only one of the three form factors is independent.

We first test that the three form factors satisfy the PCAC relation, Eq. (27), by confirming that the quark mass  $\hat{m}$  obtained from the pion two-point correlation functions,  $\langle \Omega | (\partial_\mu A_\mu - 2\hat{m}P)_t P_0 | \Omega \rangle = 0$ , is consistent with that from the three-point function  $\langle \Omega | \chi_\tau (\partial_\mu A_\mu - 2\hat{m}P)_t \bar{\chi}_0 | \Omega \rangle = 0$  for  $\mathbf{p} = 0$ .<sup>4</sup> Using the more accurate value of  $\hat{m}$  determined from the two-point functions, we plot in Fig. 15 (left) the following five quantities motivated by the PCAC relation given in Eq. (27):

$$R_1 = \frac{Q^2}{4M_N^2} \frac{\tilde{G}_P(Q^2)}{G_A(Q^2)}, \quad (30)$$

$$R_2 = \frac{2\hat{m}}{2M_N} \frac{G_P(Q^2)}{G_A(Q^2)}, \quad (31)$$

$$R_3 = \frac{Q^2 + M_\pi^2}{4M_N^2} \frac{\tilde{G}_P(Q^2)}{G_A(Q^2)}, \quad (32)$$

$$R_4 = \frac{4\hat{m}M_N}{M_\pi^2} \frac{G_P(Q^2)}{\tilde{G}_P(Q^2)}, \quad (33)$$

$$R_5 = \frac{aQ^2}{4M_N} \frac{G_P(Q^2)}{G_A(Q^2)}, \quad (34)$$

for the four ensembles  $a12m310$ ,  $a09m130$ ,  $a06m220$  and  $a06m135$ . Including the  $O(a)$  improvement of the axial

<sup>3</sup> In our calculations, the  $Q^2$  values are large, roughly 2–10  $M_\pi^2$  as can be inferred from Table III.

<sup>4</sup> The full set of correlation functions needed to analyze the PCAC relation for the  $\mathbf{p} \neq 0$  cases were, unfortunately, not calculated.

ensemble	$(Q^{*2} + M_\pi^2)\tilde{G}_P(Q^{*2})/g_A$	$g_P^*/g_A$ ( $Q^2 = Q^{*2}$ )	$c_1 * (2M_N/m_\mu)$ [GeV $^2$ ]	$g_{\pi\text{NN}}/g_A$ ( $Q^2 = -M_\pi^2$ )	$c_2 * (2M_N/m_\mu)$	$c_3 * (2M_N/m_\mu)$ [GeV $^{-2}$ ]
$a12m310$	3.72(12)	1.70(05)	3.94(16)	8.35(38)	-2.02(48)	0.24(42)
$a12m220L$	2.70(17)	2.29(15)	2.47(18)	5.86(43)	3.85(1.1)	-9.5(2.5)
$a09m310$	3.67(26)	1.64(12)	3.83(38)	8.20(83)	-1.56(1.2)	-0.21(94)
$a09m220$	2.53(19)	2.16(17)	2.35(26)	5.63(62)	3.01(1.9)	-5.7(3.3)
$a09m130$	1.85(10)	3.60(19)	1.75(10)	4.83(30)	3.37(43)	-6.04(63)
$a06m310$	3.74(19)	1.60(08)	3.94(27)	8.31(59)	-1.85(82)	-0.10(62)
$a06m220$	2.70(09)	2.11(07)	2.64(12)	6.28(30)	0.93(61)	-2.54(84)
$a06m135$	1.77(07)	3.47(15)	1.66(09)	4.56(26)	3.84(63)	-6.4(1.1)

TABLE VIII. Results obtained from fits to  $(m_\mu/2M_N)\tilde{G}_P(Q^2)/g_A$  using Eq. (26). The second column gives  $(Q^2 + M_\pi^2)\tilde{G}_P(Q^{*2})/g_A$  at  $Q^2 = Q^{*2} = 0.88m_\mu^2$  GeV $^2$ . These data are shown by the symbol star in Fig. 12. The third column gives  $g_P^*/g_A$  using Eq. (12). The fit parameters  $c_i$  are rescaled by  $2M_N/m_\mu$  so that the fourth column gives the residue of the pole at  $Q^2 = -M_\pi^2$  from which  $g_{\pi\text{NN}}/g_A$ , given in column five, is obtained by dividing by  $4M_N F_\pi$ . Corrections to the pion pole-dominance ansatz are proportional to the parameters  $c_2$  and  $c_3$ .

current, the ratios in Eqs (30), (32) and-(33) become

$$R_1^I = \frac{Q^2}{4M_N^2} \frac{\tilde{G}_P^I(Q^2)}{G_A(Q^2)}, \quad (35)$$

$$R_3^I = \frac{Q^2 + M_\pi^2}{4M_N^2} \frac{\tilde{G}_P^I(Q^2)}{G_A(Q^2)}, \quad (36)$$

$$R_4^I = \frac{2\hat{m}2M_N}{M_\pi^2} \frac{G_P(Q^2)}{\tilde{G}_P^I(Q^2)}. \quad (37)$$

The three improved ratios  $R_{1,3,4}^I$  are shown in Fig. 15 (right). Note that  $R_1^{[I]} + R_2 = 1$  checks the PCAC relation given in Eq. (27) (or Eq. (28));  $R_3^{[I]} = 1$  tests the pion pole-dominance ansatz Eq. (11); and  $R_4^{[I]} = 1$  tests the relation Eq. (29). Comparing the two sets of panels in Fig. 15 shows that improving the axial current has a very small effect. This is because the value of the improvement coefficient  $c_A$ , that multiplies the correction term  $R_5^{[I]}$ , is small. Thus, improving the axial current to  $O(a)$  does not explain the large deviation of  $R_1^{[I]} + R_2$  from unity illustrated in Fig. 15.

For all four ensembles, data in Fig. 15 show that  $R_1^{[I]} + R_2 \approx R_3^{[I]}$  for small  $Q^2$ , however, both  $R_1^{[I]} + R_2$  and  $R_3^{[I]}$  are much smaller than unity. The deviation of  $R_4^{[I]}$  from unity grows with  $Q^2$ , but decreases as  $a \rightarrow 0$  and  $M_\pi \rightarrow M_\pi^{\text{Physical}}$ . This pattern is, in general, consistent with these being discretization effects. Note that the corrections to  $2\hat{m}G_P(Q^2) = (M_\pi^2/2M_N)\tilde{G}_P(Q^2)$ , or to  $R_4^{[I]} = 1$ , do not significantly impact  $R_1^{[I]} + R_2 \approx R_3^{[I]}$  because the dominant contribution to both sides of this approximate equality comes from  $R_1^{[I]}$ .

The data for  $R_3$  from all eight ensembles is plotted in Fig. 13 and show that the deviations from unity increase with decreasing  $Q^2$ ,  $a$  and  $M_\pi^2$ . For the physical pion mass ensembles, the  $O(50\%)$  deviation for  $Q^2 < 0.2$  GeV $^2$  is surprisingly large. Such  $Q^2$  dependent deviations from the PCAC relation are, generically, indicators of discretization artifacts. The increase in the deviations with decreasing  $a$  does not support this expectation, and as

shown in Fig. 15, the  $O(a)$  improvement of the axial current does not reduce the deviations. Therefore, the observed large deviation remains unexplained and requires further investigation.

## IX. ANALYSIS OF $g_P^*$

To determine  $g_P^*/g_A$  and  $g_{\pi\text{NN}}/g_A$  we need to evaluate  $\tilde{G}_P(Q^2)$  at  $Q^2 \equiv Q^{*2} = 0.88m_\mu^2$  and at  $Q^2 = -M_\pi^2$ . This is done using the ansatz given in Eq. (26). In Fig. 14, the data for  $(Q^2 + M_\pi^2)\tilde{G}_P(Q^2)/g_A$  and the result of the fit using Eq. (26). The extrapolated values are shown using the symbol star at  $Q^{*2} = 0.88m_\mu^2$  and by the symbol plus at  $Q^2 = -M_\pi^2$ . It is clear from Fig. 14, that there are enough free parameters in Eq. (26) to fit the data and the values obtained at  $Q^{*2}$  and  $Q^2 = -M_\pi^2$  by extrapolation are reasonable. However, the contributions of terms proportional to  $c_2$  and  $c_3$  (see Table VIII) increase as the lattice spacing  $a \rightarrow 0$  and  $M_\pi \rightarrow 135$  MeV. The quantitative change in behavior is already clear in all three  $M_\pi \approx 220$  MeV ensembles. Thus, it is unlikely that the change in behavior between the  $M_\pi \approx 310$  MeV ensembles and those at lighter  $M_\pi$  is a statistical fluctuation. Because of this change in behavior, we get low estimates of  $g_P^*/g_A$  and  $g_{\pi\text{NN}}/g_A$ .

Given the data in Table VIII, to estimate  $g_P^*$  in the limit  $a \rightarrow 0$  and  $M_\pi \rightarrow 135$  MeV, we make a fit using the ansatz

$$g_P^*(a, M_\pi)/g_A = d_1 + d_2 a + \frac{d_3}{M_\pi^2 + 0.88m_\mu^2} + d_4 M_\pi^2, \quad (38)$$

where the leading behavior in  $M_\pi^2$  is taken to be the pion-pole term evaluated at the experimental momentum scale of muon capture. We neglect possible finite volume corrections in the data in obtaining the estimates since the data do not show an obvious dependence on  $M_\pi L$ . The simultaneous fits in  $a$  and  $M_\pi$  are shown in Fig. 16. They

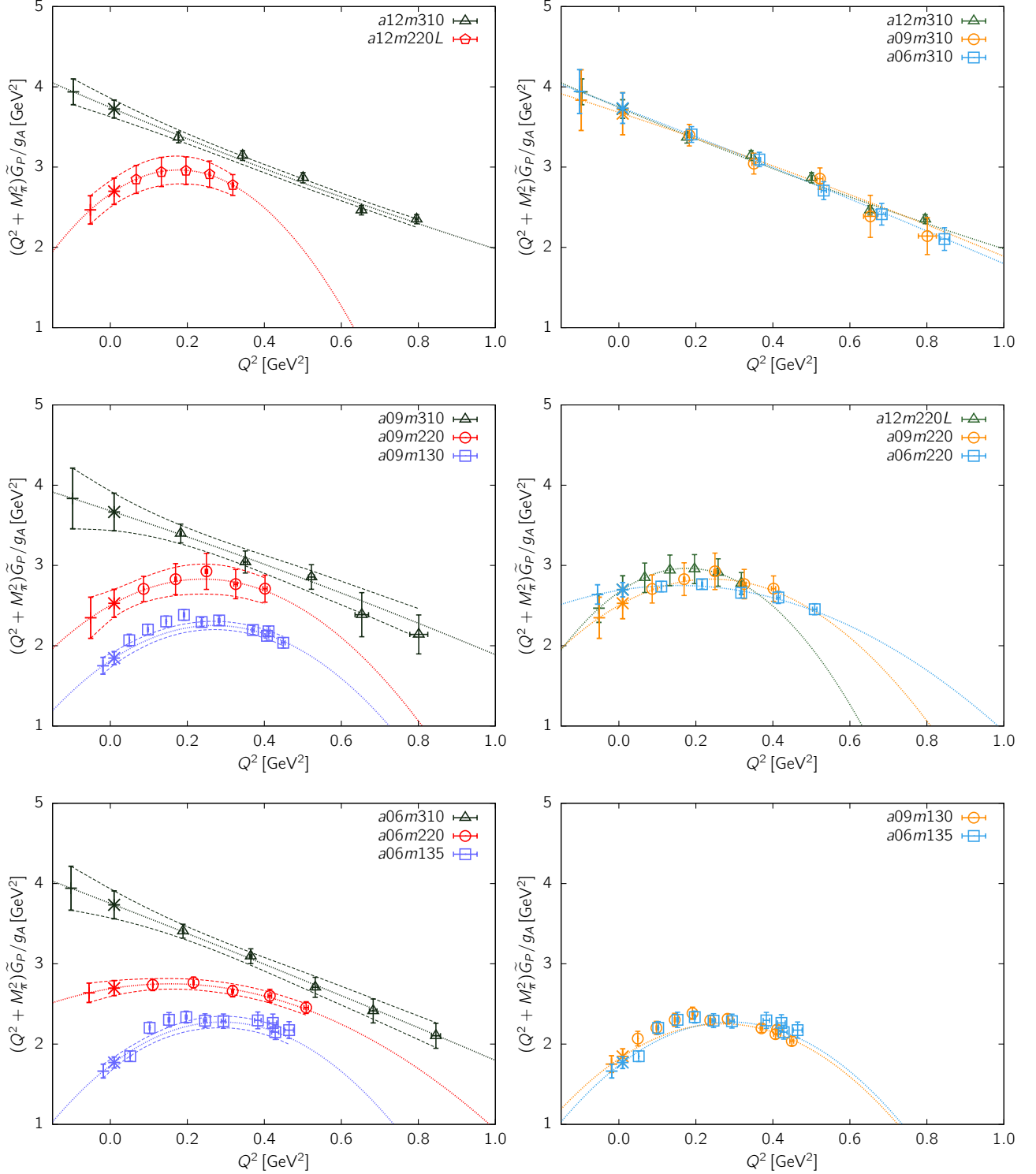


FIG. 14. The data for and the fits to the quantity  $(Q^2 + M_\pi^2) \tilde{G}_P(Q^2) / g_A$ . The figures in the left column highlight the dependence on  $M_\pi^2$  for fixed  $a$ , and those in the right column highlight the dependence on  $a$  for fixed  $M_\pi$ . The fits versus  $Q^2$  ( $\text{GeV}^2$ ) are performed using Eq. (26) with lattice estimates for the axial charge  $g_A$  and the nucleon mass,  $M_N$ . The muon mass is  $m_\mu = 0.10566$  GeV. The point with symbol star (plus) gives the value at  $Q^2 = Q^{*2} \equiv 0.88m_\mu^2$  ( $Q^2 = -M_\pi^2$ ). We show the  $1\sigma$  error band of the fits in the panels on the left.

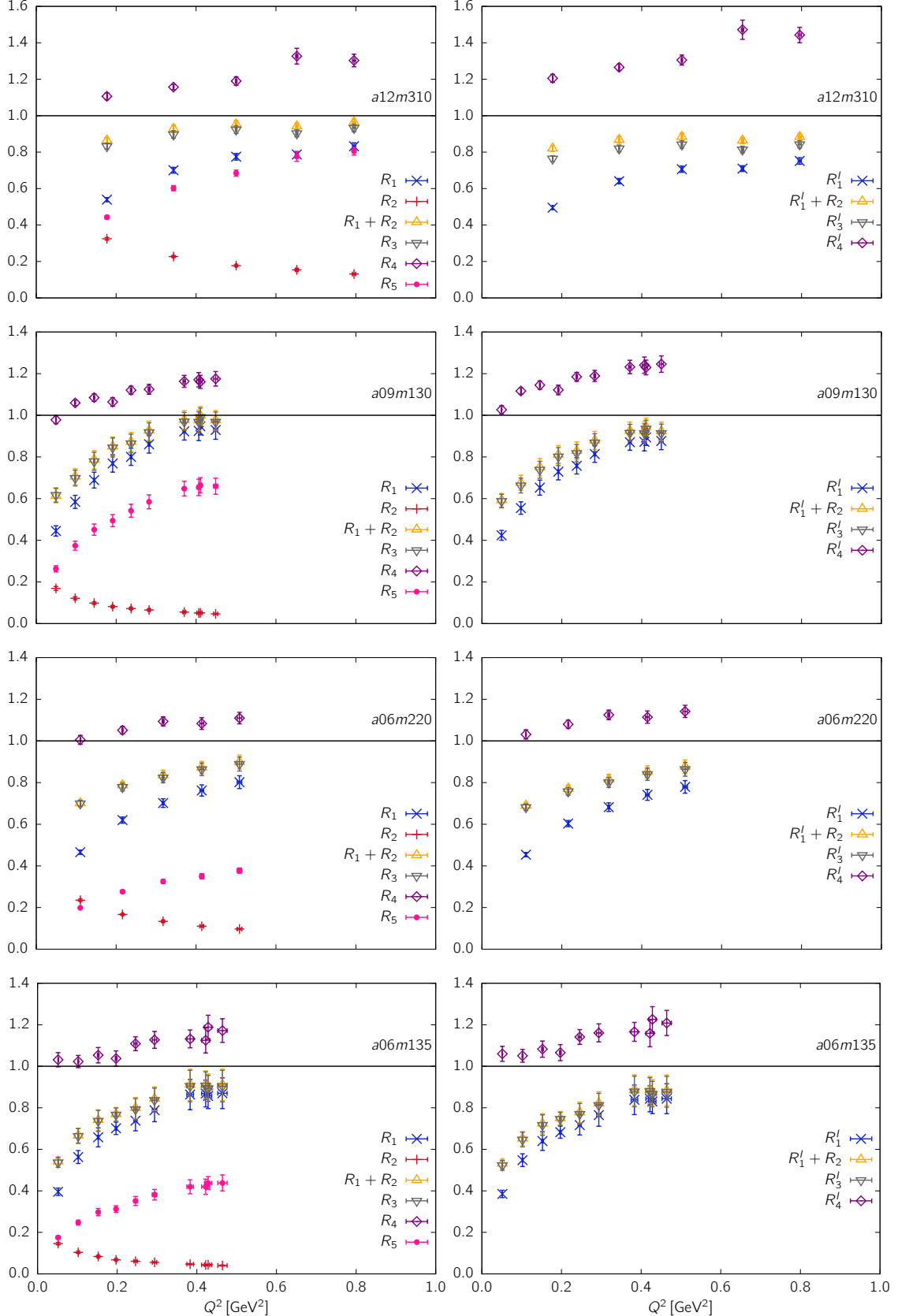


FIG. 15. (Left) The data for the five ratios  $R_i$ , defined in Eqs. (30)–(34). The four rows show data from the four ensembles  $a12m310$ ,  $a09m130$ ,  $a06m220$  and  $a06m135$ . Test of the PCAC relation, Eq. (27), is  $R_1^{[I]} + R_2 = 1$ ; of the pion pole-dominance ansatz, Eq. (11), is  $R_3^{[I]} = 1$ ; and of the relation given in Eq. (29) is  $R_4^{[I]} = 1$ . (Right) Results for the four ratios defined in Eqs. (35)–(37) using the  $O(a)$  improved axial current.

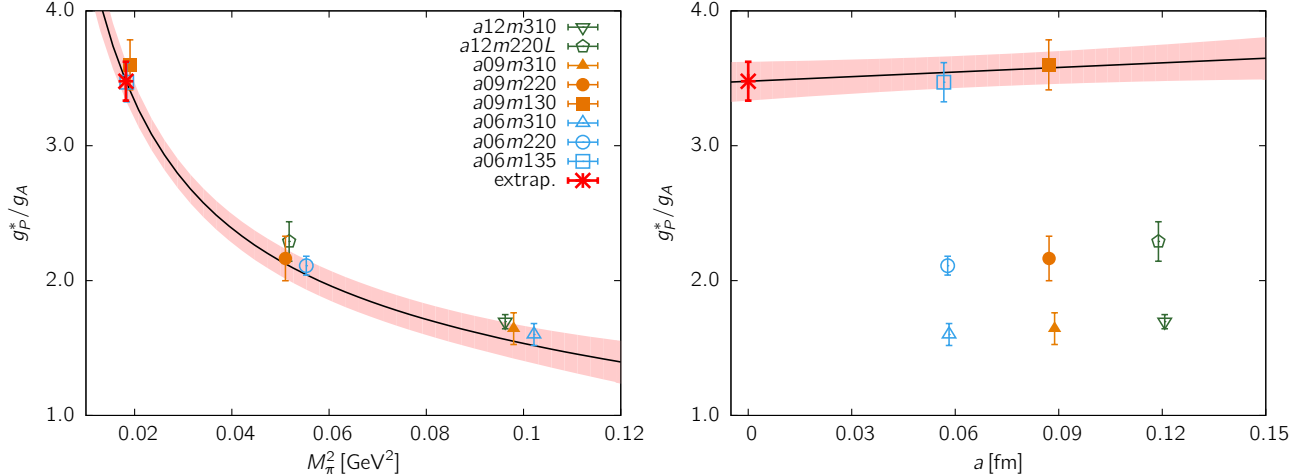


FIG. 16. The 8-point fit using Eq. (38) to the lattice data for  $g_P^*/g_A$ . In the left (right) panel, the data are shown versus the single variable  $M_\pi^2$  ( $a$ ), whereas the fits include dependence on both variables simultaneously. The same symbols are used for data in both figures and defined in the left panel.

give

$$\begin{aligned} g_P^*/g_A &= 3.48(14), \\ g_P^* &= 4.44(18), \end{aligned} \quad (39)$$

where the final value of  $g_P^*$  is obtained by multiplying the ratio obtained from the fit by the experimental value  $g_A = 1.276$ .

We summarize lattice QCD results for  $g_P^*$  in Fig. 17. The results  $g_P^* = 7.68 \pm 1.03$  (Lin(2008) [37]),  $g_P^* = 6.4 \pm 1.2$  (Yamazaki(2009) [38]), and  $g_P^* = 8.47(21)(87)(2)(7)$  (Green(2017) [39]) have all been obtained on ensembles with  $M_\pi > 300$  MeV and extrapolated to  $M_\pi^{\text{Physical}}$  using just the pion-pole term,  $(Q^{*2} + M_\pi^2)\tilde{G}_P(Q^{*2})/((Q^{*2} + M_\pi^2)^{\text{Physical}})$ . Thus all estimates from  $M_\pi > 300$  MeV ensembles, including our three  $M_\pi \approx 310$  MeV ensembles, yield  $g_P^* \approx 8$  after scaling in  $M_\pi$  using the pion-pole ansatz. As we have discussed above, the  $Q^2$  corrections to the pion-pole ansatz become large for  $M_\pi < 300$  MeV and our direct simulations at  $M_\pi \approx 220$  and 135 MeV show that using just the pion-pole ansatz for scaling in  $M_\pi^2$  is not justified.

Our estimate,  $g_P^* = 4.44(18)$ , is consistent with the value  $g_P^* = 4.20(20)$  extracted from Ref. [34], once their result is corrected for by the factor 0.5 that was missed in their definition of  $g_P^*$ . Note that their analysis also shows the change in the scaling behavior for  $M_\pi < 300$ , and they report results analogous to our Fig. 15.

To summarize, our low value,  $g_P^* = 4.44(18)$ , is about half of the values obtained from the muon capture experiment and  $\chi$ PT as summarized in Eq. (13). Our data are well-fit by the ansatz given in Eq. (26), however, the corrections proportional to the parameters  $c_2$  and  $c_3$  become large as  $M_\pi \rightarrow 135$  MeV. Thus, one cannot extrapolate to  $M_\pi^{\text{Physical}}$  using just the pion-pole term. The underlying reason for a low value of  $g_P^*$  is the large deviation from unity of the ratios  $R_1^{[I]} + R_2$  and  $R_3^{[I]}$ , defined in

Eqs. (30)–(32), at low  $Q^2$ . The size of the deviations are shown in Fig. 13. Considering that the  $O(a)$  improvement of the axial current does not reduce the deviation, the observed violation of the PCAC relation remains unexplained.

## X. ANALYSIS OF THE PION-NUCLEON COUPLING, $g_{\pi\text{NN}}$

The pion-nucleon coupling,  $g_{\pi\text{NN}}$ , is defined as the residue at the pion pole of  $\tilde{G}_P(Q^2)$ , i.e., at  $Q^2 = -q^2 = -M_\pi^2$ . Since all our data are obtained at positive values of  $Q^2$ , we first fit  $\tilde{G}_P(Q^2)$  using the ansatz in Eq. (26) and then calculate

$$g_{\pi\text{NN}} = \lim_{Q^2 \rightarrow -M_\pi^2} \frac{M_\pi^2 + Q^2}{4M_N F_\pi} \tilde{G}_P(Q^2), \quad (40)$$

where  $F_\pi$  is the pion decay constant. These estimates are given in the fifth column of Table VIII. To extrapolate to  $a \rightarrow 0$  and  $M_\pi \rightarrow 135$  MeV, we use the leading order ansatz given in Eq. (23). The fit, shown in Fig. 18, gives

$$\begin{aligned} g_{\pi\text{NN}}/g_A &= 4.53(45), \\ g_{\pi\text{NN}} &= 5.78(57), \end{aligned} \quad (41)$$

with  $g_A = 1.276$ . This lattice value has to be compared with  $g_{\pi\text{NN}} = 13.69 \pm 0.12 \pm 0.15$  obtained from the  $\pi N$  scattering length analysis [23]. As discussed above in the analysis of  $g_P^*$ , our low value is a consequence of the unexplained deviation of the ratios  $R_1^{[I]} + R_2$  and  $R_3^{[I]}$  from unity at small  $Q^2$  on the  $M_\pi = 220$  and 135 MeV ensembles.

We can also estimate  $g_{\pi\text{NN}}$  using the Goldberger-Treiman relation,

$$g_{\pi\text{NN}} = \frac{M_N g_A}{F_\pi}. \quad (42)$$

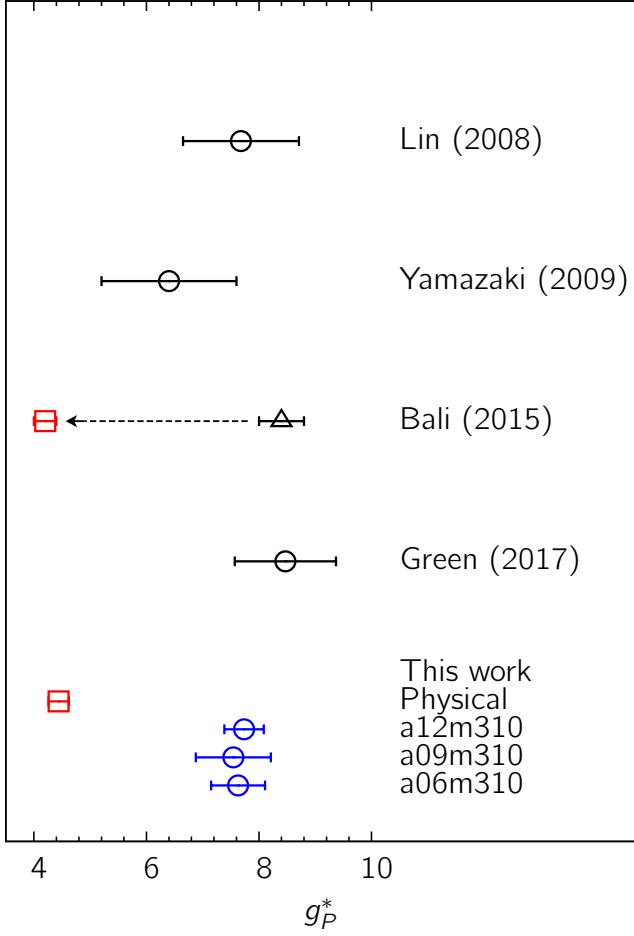


FIG. 17. Summary of lattice QCD results for the renormalized  $g_P^*$ . Previous results are from Lin(2008) [37], Yamazaki(2009) [38], Bali(2015) [34], and Green(2017) [39]. The data with open circles were obtained from simulations with  $M_\pi > 300$  MeV and scaled to the physical pion mass  $M_\pi = 135$  MeV using just the pion-pole term as discussed in the text.

The resulting values of  $g_{\pi\text{NN}}$  given in Table IX for each ensemble are obtained using estimates of  $g_A/F_\pi$  from Ref. [25].<sup>5</sup> The extrapolation to  $a \rightarrow 0$  and  $M_\pi \rightarrow 135$  MeV using the ansatz given in Eq. (23) with just the leading order corrections is shown in Fig. 19. The result,  $g_{\pi\text{NN}} = 12.87(34)$ , is consistent with the value,  $g_{\pi\text{NN}} = 13$ , one gets by using the experimental values,  $g_A = 1.276$ ,  $M_N = 939$  MeV and  $F_\pi = 92.2$  MeV. Note that this test of the Goldberger-Treiman relation relies on our calculation of  $g_A$  right to within 5%, whereas direct calculations of  $g_P^*$  and  $g_{\pi\text{NN}}$  depend on  $\tilde{G}_P(Q^2)$ , which we find shows large deviations from the PCAC relation.

	$M_\pi \approx 310$ MeV	$M_\pi \approx 220$ MeV	$M_\pi \approx 135$ MeV
$a = 0.12$ fm	12.7(2)	12.4(2)	
$a = 0.09$ fm	12.9(4)	12.6(4)	12.1(3)
$a = 0.06$ fm	12.4(2)	12.6(2)	13.3(3)

TABLE IX. Results for  $g_{\pi\text{NN}} = M_N g_A/F_\pi$  determined using values of  $M_N$ ,  $g_A$  and  $F_\pi$  obtained on the eight ensembles.

## XI. A HEURISTIC ANALYSIS

Testing the PCAC relation, Eq. (3), requires no input outside of our lattice calculations: the three form factors,  $G_A(Q^2)$ ,  $\tilde{G}_P(Q^2)$ , and  $G_P(Q^2)$ , are obtained from our lattice calculations of three-point functions, and  $\hat{m}$  is obtained from the pion two-point correlations functions. Thus, the large deviations from the PCAC relation, as discussed in Sections VIII, IX and X, are troubling. They motivated us to examine alternatives to the single pion pole-dominance ansatz. The data in Fig. 15 suggest that the deviation from the PCAC relation can be reduced by enhancing the contribution of  $R_2$ , i.e., the relative size of the  $M_\pi^2$  versus the  $Q^2$  term in pion pole-dominance ansatz. We, therefore, fit the data using

$$\frac{m_\mu}{2M_N} \frac{\tilde{G}_P(Q^2)}{g_A} = \frac{e_1}{M_{\text{pole}}^2 + Q^2} + e_2 + e_3 Q^2, \quad (43)$$

where  $M_{\text{pole}}^2$  and  $e_i$  are free parameters. The fits for  $e_3 = 0$  are shown in Fig. 20 and the resulting value of  $M_{\text{pole}}$  is given in Table X. As expected, allowing  $M_{\text{pole}}$  to be a free parameter changes the fits very significantly and the results mimic the pion pole-dominance behavior seen for the  $M_\pi > 300$  MeV ensembles. This can be seen by comparing the fits in Fig. 20 with those in Fig. 14 which were obtained using the fit ansatz given in Eq. (26). The surprise is the size of the difference,  $M_{\text{pole}} - M_\pi$ , that can be inferred from Table X. While we expect some shift in  $M_\pi$  to correct for all the intermediate states that couple to the axial current rather than just the groundstate pion, it is difficult to explain the observed large shift. Nevertheless, continuing with this heuristic analysis, we show in Fig. 21 the extrapolation of the estimates of  $g_P^*$ , given in Table X and obtained with  $e_3 = 0$ , to the physical pion mass and the continuum limit using the ansatz  $h_0/(Q^{*2} + M_{\text{pole}}^2) + h_1 + h_2 a$ . This analysis gives  $g_P^* = 7.0(7)$  and similarly  $g_{\pi\text{NN}} = 11.2(1.3)$ . The large change is mainly because the extrapolation is now being done from the larger values of  $M_{\text{pole}}$ .

For the physical pion mass ensembles,  $a09m130$  and  $a06m135$ , the fits can be performed with  $e_3$  a free parameter since we have data at ten values of  $Q^2$ . Adding  $e_3$  to the fit ansatz give a significantly different value for  $M_{\text{pole}}$  and, as a result, the violet open squares move to the filled green squares in Fig. 20. Even the curvature of the fit has opposite sign in the two cases. Not surprisingly, the values of  $g_P^*$  and  $g_{\pi\text{NN}}$  for the two physical mass ensembles change significantly and in opposite di-

<sup>5</sup> The values for the  $a06m135$  ensemble are  $g_A/F_\pi = 12.62(29)$  and  $F_\pi = 95.4(1.0)$ .

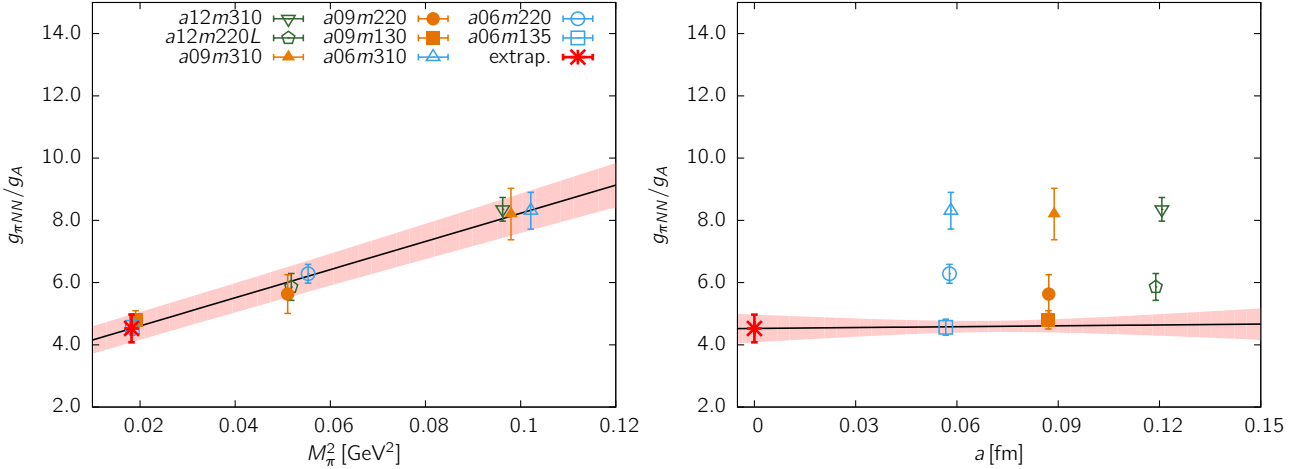


FIG. 18. The 8-point fit to the lattice data for  $g_{\pi NN}/g_A$  using Eq. (23). In this fit, We neglect the possible finite volume term. In the left (right) panel, the data are shown versus the single variable  $M_\pi^2$  ( $a$ ), whereas the fit is to estimates extrapolated to the physical value in the other variable. The same symbols are used for data in both figures and defined in the left panel.

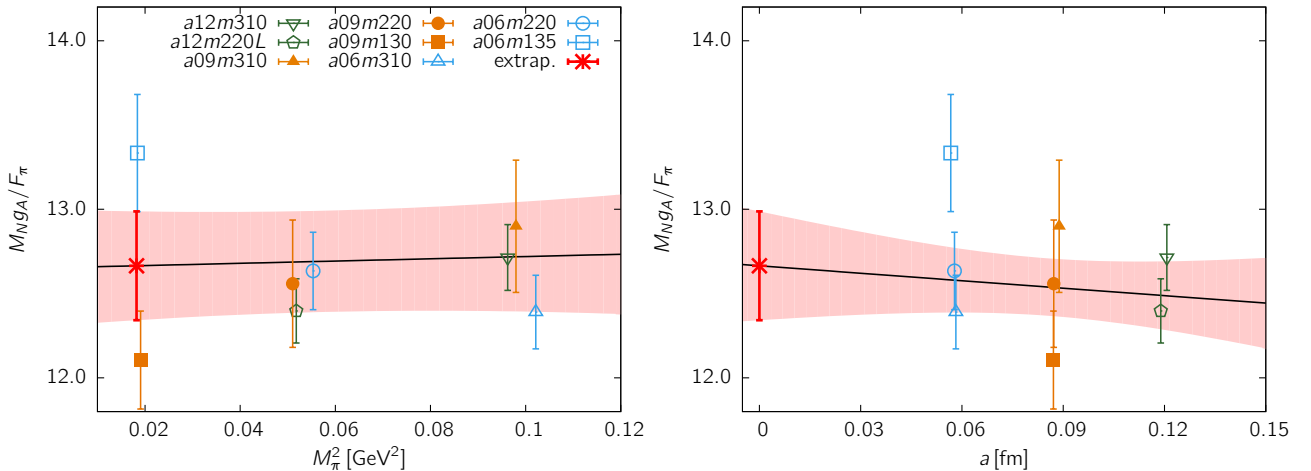


FIG. 19. The data for  $g_{\pi NN} = M_N g_A / F_\pi$  from the eight ensembles and the simultaneous fit in  $a$  and  $M_\pi^2$  to obtain the result in the limit  $a \rightarrow 0$  and  $M_\pi = 135$  MeV using the ansatz in Eq. (23). The finite volume correction term is neglected in the fit. The rest is the same as in Fig. 18.

rection on including the  $e_3$  term in the fit. In short, this heuristic analysis becomes unstable as  $M_\pi \rightarrow 135$  MeV.

Note that introducing  $M_\pi^2$  as a free parameter is analogous to tuning  $\hat{m}$  in the PCAC relation, Eq. 3, by requiring  $R_1 + R_2$ , shown in Fig. 15, is unity independent of  $Q^2$ , rather than using the value from the PCAC relation applied to the pion two-point correlation function. The bottom line of such a heuristic analysis is that the change,  $M_\pi^2 \rightarrow M_\pi^2$  or in  $\hat{m}$ , to accomodate the data is much larger than what is expected from discretization effects. Therefore, understanding why the three form factors do not satisfy the PCAC relation remains our highest priority for future work.

	$M_\pi$ [MeV]	$M_{\text{pole}}$ [MeV]	$g_P^*/g_A$	$g_{\pi NN}/g_A$
<i>a12m310</i>	310(3)	307(23)	1.69(15)	8.1(0.5)
<i>a12m220L</i>	228(2)	294(18)	2.07(13)	9.6(1.4)
<i>a09m310</i>	313(3)	320(51)	1.62(31)	8.5(1.2)
<i>a09m220</i>	226(2)	294(47)	1.88(22)	8.7(2.2)
<i>a09m130</i>	138(1)	219(9)	2.84(18)	8.2(0.4)
<i>a06m310</i>	319(2)	332(36)	1.54(19)	8.7(0.9)
<i>a06m220</i>	235(2)	298(19)	1.79(11)	8.6(0.6)
<i>a06m135</i>	136(2)	247(15)	2.40(14)	8.8(0.7)

TABLE X. Results for  $M_{\text{pole}}$ ,  $g_P^*$  and  $g_{\pi NN}$  using the heuristic fit ansatz given in Eq. (43) with  $e_3 = 0$ .

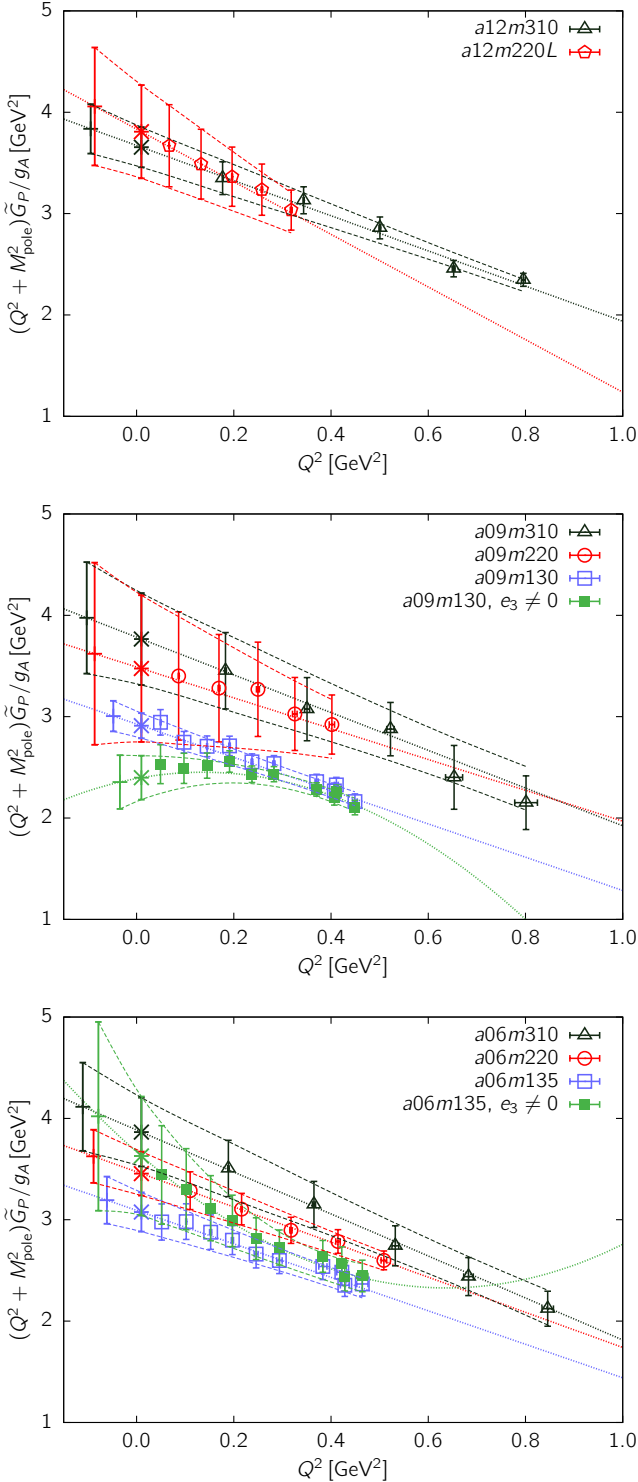


FIG. 20. The data for the quantity  $(Q^2 + M_{\text{pole}}^2)\tilde{G}_P(Q^2)/g_A$ . The three panels highlight the dependence on  $M_\pi^2$  for fixed  $a$ . The fits versus  $Q^2$  in units of  $\text{GeV}^2$  are performed using Eq. (43) with  $e_3 = 0$ . The point with symbol star (plus) gives the value at  $Q^2 = Q^{*2} \equiv 0.88m_\mu^2$  ( $Q^2 = -M_\pi^2$ ). We show the  $1\sigma$  error band of the fits. For the two physical mass ensembles,  $a09m130$  and  $a06m135$ , we also show the data (solid green squares) and the fits (green lines) including the  $e_3$  term defined in Eq. (43).

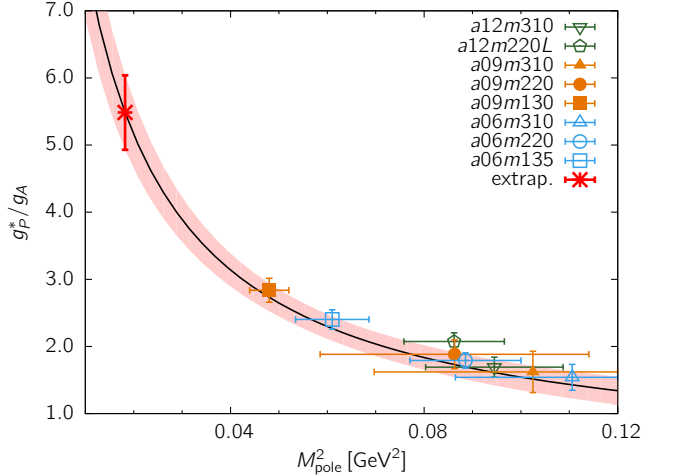


FIG. 21. The extrapolation of  $g_P^*/g_A$  to the physical pion mass and the continuum limit using  $h_0/(Q^{*2} + M_{\text{pole}}^2) + h_1 + h_2a$ , where  $M_{\text{pole}}^2$  is a free parameter introduced in the heuristic analysis to fit the data.

## XII. CONCLUSIONS

We have presented high statistics results of the axial and the induced pseudoscalar form factors on eight ensembles described in Table I using a clover-on-HISQ approach. The pseudoscalar form factor was calculated on four ensembles to test the PCAC relation.

To fit the  $Q^2$  dependence of the axial form factor,  $G_A(Q^2)$ , we use the  $z$ -expansion and the dipole ansatz. Estimates from the  $z^{2+4}$  versus  $z^{3+4}$  truncation of the  $z$ -expansion are consistent within  $1\sigma$  uncertainty. The dipole ansatz does a remarkable job of fitting the data. The estimates of  $r_A$  from these three fit ansatz agree for all eight ensembles. The results, after extrapolation in  $a$  to the continuum limit and  $M_\pi L \rightarrow \infty$ , and evaluated at  $M_\pi = 135$  MeV, are  $r_A|_{z\text{-expansion}} = 0.46(6)$  and  $r_A|_{\text{dipole}} = 0.49(3)$ . While these results are consistent, they are smaller than the phenomenological estimates given in Eq. (6). Our estimate  $r_A|_{\text{dipole}} = 0.49(3)$  corresponds to an axial mass  $\mathcal{M}_A = 1.39(9)$  that is in good agreement with the value obtained by the MiniBooNE collaboration [9]. Our final estimate from the combined dipole and the  $z$ -expansion analyses is  $r_A|_{\text{combined}} = 0.48(4)$ .

The data for the induced pseudoscalar form factor  $\tilde{G}_P(Q^2)$  versus  $Q^2$  show little dependence on the lattice spacing  $a$ , the pion mass  $M_\pi$  or the lattice size  $M_\pi L$ . Our test of the PCAC relation, including the contribution of the pseudoscalar form factor  $G_P(Q^2)$ , show significant deviations for  $Q^2 \lesssim 0.2 \text{ GeV}^2$ , in particular for the physical mass ensembles. Extrapolation in  $Q^2$  using an ansatz based on the pion pole-dominance hypothesis, Eq. (23), fits the lattice data well but leads to very low estimates of the induced pseudoscalar charge,  $g_P^* = 4.44(18)$ , and of the pion-nucleon coupling  $g_{\pi\text{NN}} = 5.78(57)$  estimated as

the residue at the pole in  $\tilde{G}_P(Q^2)$  at  $Q^2 = -M_\pi^2$ . These low estimates are a consequence of the large deviations from the PCAC relation for  $Q^2 \lesssim 0.2 \text{ GeV}^2$ . All previous estimates from  $M_\pi > 300 \text{ MeV}$  ensembles that gave  $g_P^* \approx 8$  were not sensitive to this problem as discussed in Sec. VIII.

Work is under progress to improve the statistical and systematic precision of the three form factors  $G_A(Q^2)$ ,  $\tilde{G}_P(Q^2)$  and  $G_P(Q^2)$  and to understand the reason for the failure of these three form factors to satisfy the PCAC relation for  $Q^2 \lesssim 0.2 \text{ GeV}^2$ .

#### ACKNOWLEDGMENTS

We thank the MILC Collaboration for providing the 2+1+1-flavor HISQ lattices used in our calculations. We acknowledge Gunnar Bali, Joseph Carlson, Vincenzo Cirigliano, Sara Collins, Jeremy Green, Richard Hill, Emanuele Mereghetti, Aaron Meyer and Saori Pastore for discussions. Simulations were carried out on computer facilities of (i) the USQCD Collaboration, which are funded by the Office of Science of the U.S. Department of Energy, (ii) the National Energy Research Scientific Computing Center, a DOE Office of Science User Facility supported by the Office of Science of the U.S. Department of Energy under Contract No. DE-AC02-05CH11231; (iii) Institutional Computing at Los Alamos National Laboratory; and (iv) the High Performance Computing Center at Michigan State University. The calculations used the Chroma software suite [24]. This work is supported by the U.S. Department of Energy, Office of Science of High Energy Physics under contract number DE-KA-1401020 and the LANL LDRD program. The work of H-W. Lin was supported in part by the M. Hildred Blewett Fellowship of the American Physical Society.

#### Appendix A: Fits to two-point functions

This appendix shows the 2- and 4-state fits to the nucleon two-point correlation function on the eight ensembles Figs. 22, 23, 24, 25, 26, 27, 28, and 29. The estimates of the nucleon energies and the amplitudes extracted from these fits are collected together in Tables XI, XII, XIII, XIV, XV, XVI, XVII and XVIII. Tests of the dispersion relation for the nucleon,  $(aE)^2 - \sum_i f_i^2 = (aM)^2$ , for the three cases  $f_i = ap_i$ ,  $\sin(ap_i)$  and  $2\sin(ap_i/2)$  are shown in Fig. 30 for four ensembles listed in the labels.

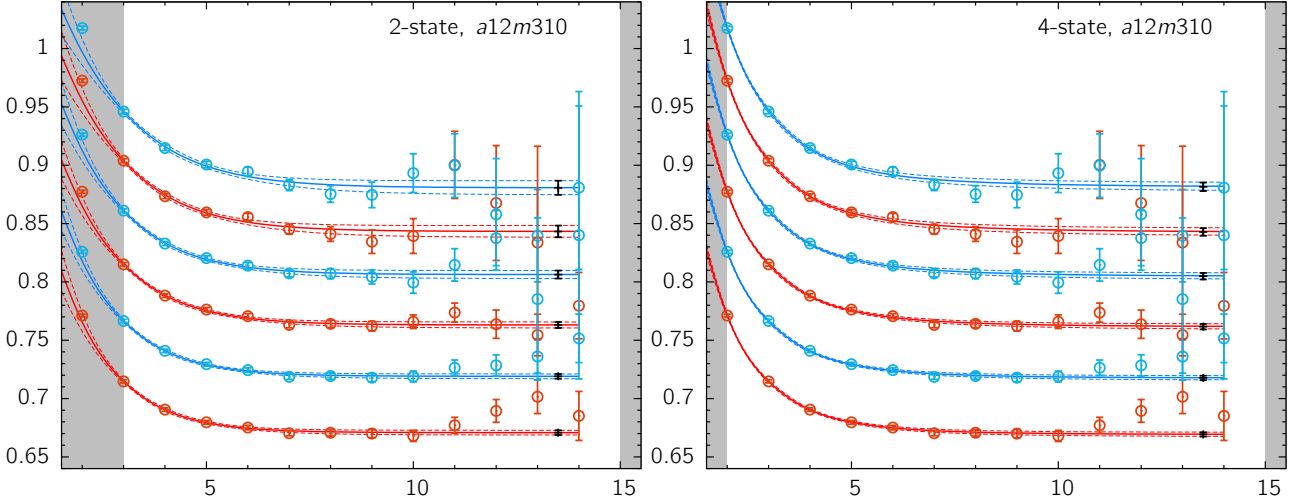


FIG. 22. Plot of the effective-energy,  $aE_0$ , versus the Euclidian time  $t$  for the  $a12m310$  ensemble data. The left panel shows the 2-state fits while the right panel shows the 4-state fits. The lines with error bands show the result for  $M_{\text{eff}}$  obtained from the 2-state (4-state) fit for the various momenta analyzed. The unshaded region specifies the range of timeslices used in the fits. To help distinguish between the estimates for the various momenta, the data and fits for  $M_{\text{eff}}$  are shown using alternating red and blue colors. For each momenta, the point with error bars in black on the right of the  $t$ -interval used in the fits is the estimate of the ground-state energy  $E_0$ .

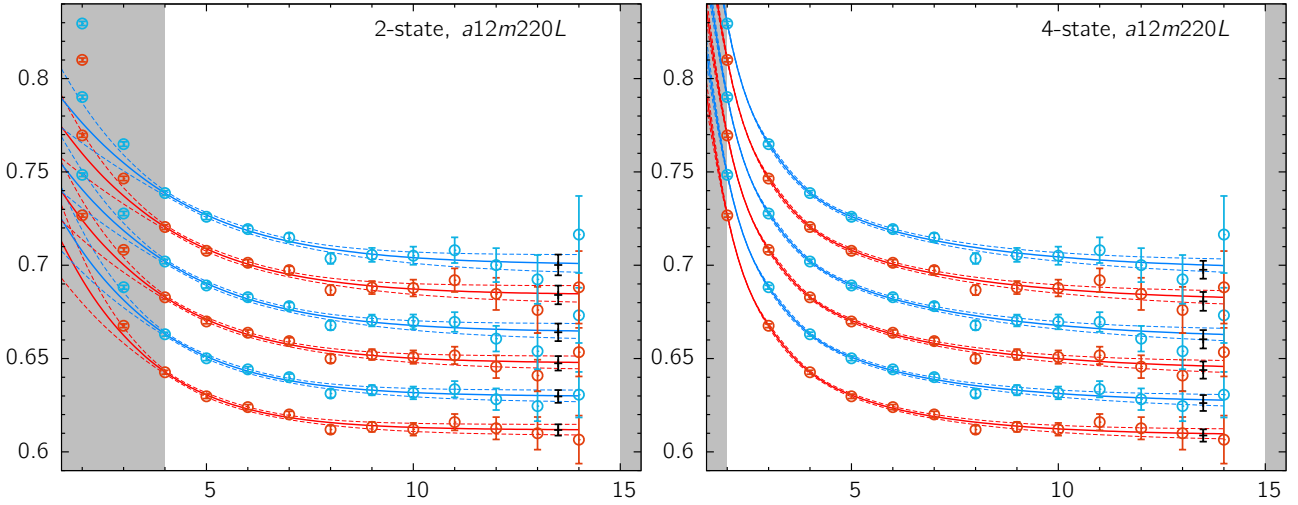


FIG. 23. Plot of the effective-energy for the  $a12m220L$  ensemble data. The rest is the same as in Fig. 22.

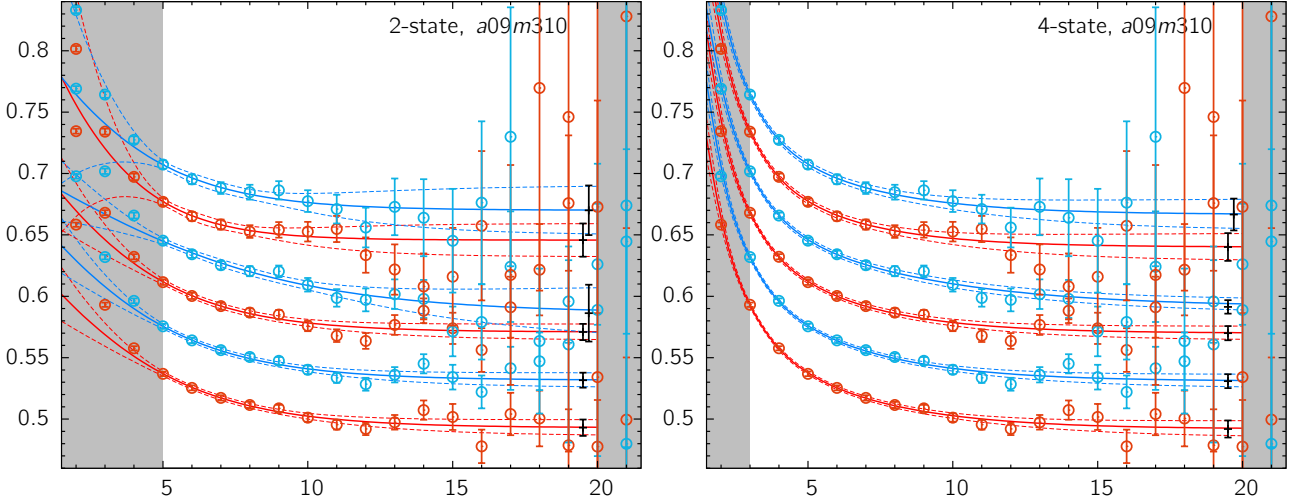


FIG. 24. Plot of the effective-energy for the  $a09m310$  ensemble data. The rest is the same as in Fig. 22.

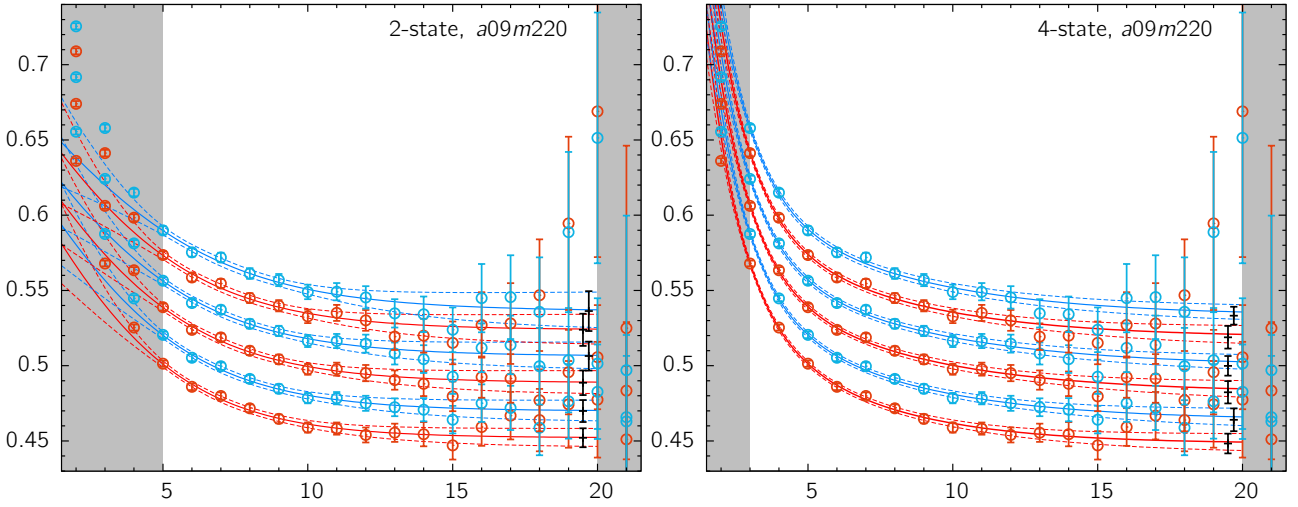


FIG. 25. Plot of the effective-energy for the  $a09m220$  ensemble data. The rest is the same as in Fig. 22.

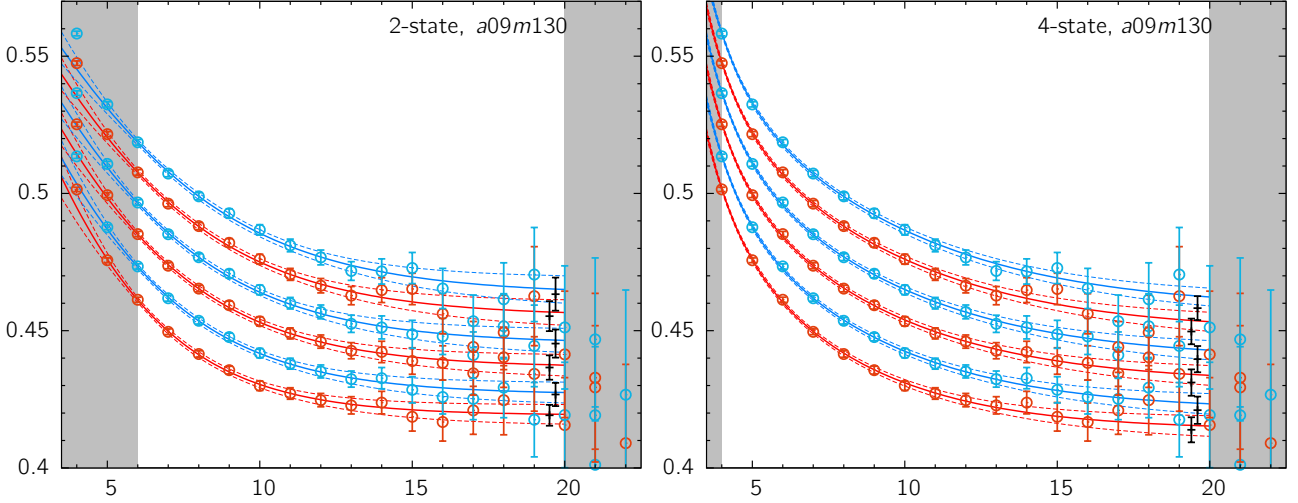


FIG. 26. Plot of the effective-energy for the  $a09m130$  ensemble data. The rest is the same as in Fig. 22.

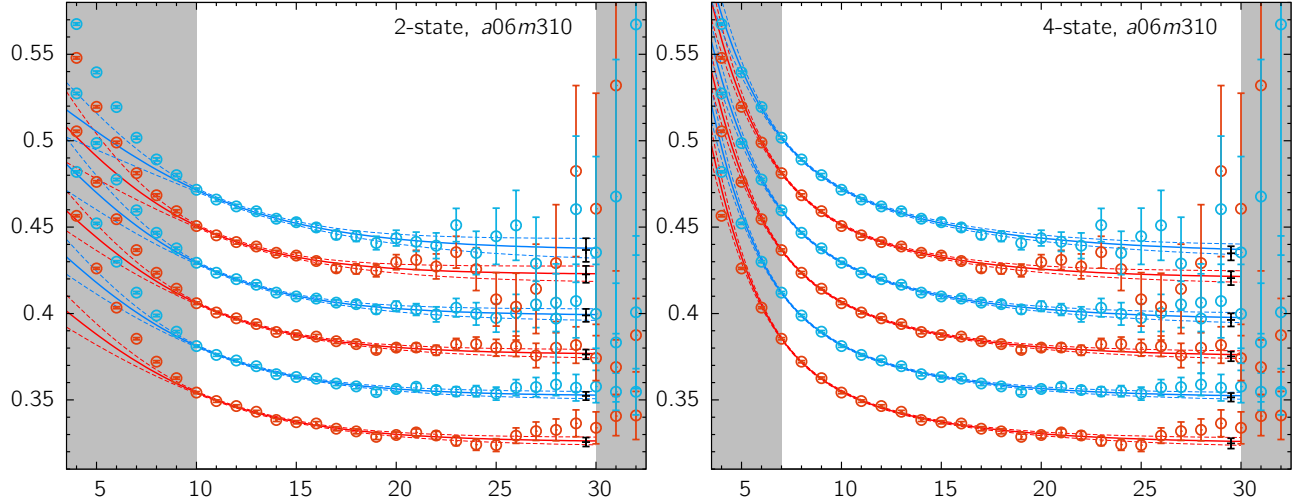


FIG. 27. Plot of the effective-energy for the  $a06m310$  ensemble data. The rest is the same as in Fig. 22.

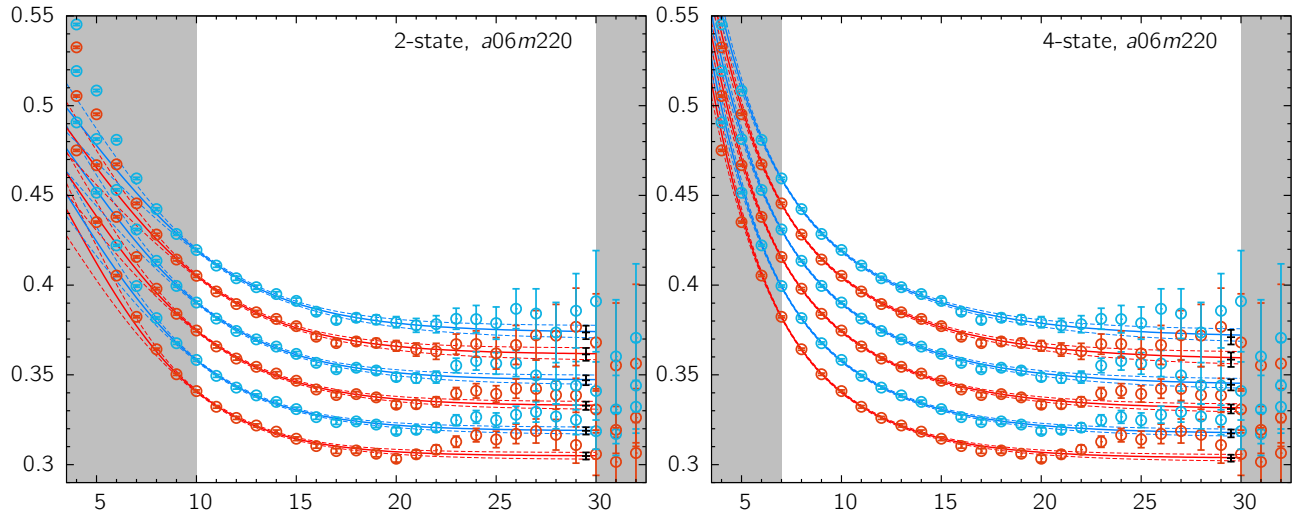


FIG. 28. Plot of the effective-energy plots for the  $a06m220$  ensemble data. The rest is the same as in Fig. 22.

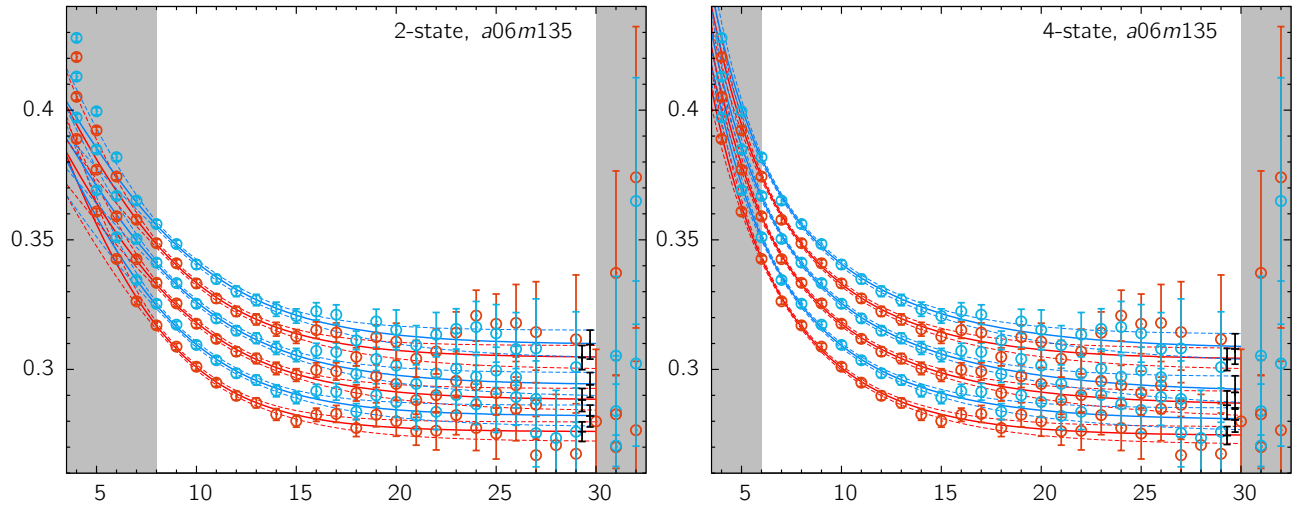


FIG. 29. Plot of the effective-energy for the  $a06m135$  ensemble data. The rest is the same as in Fig. 22.

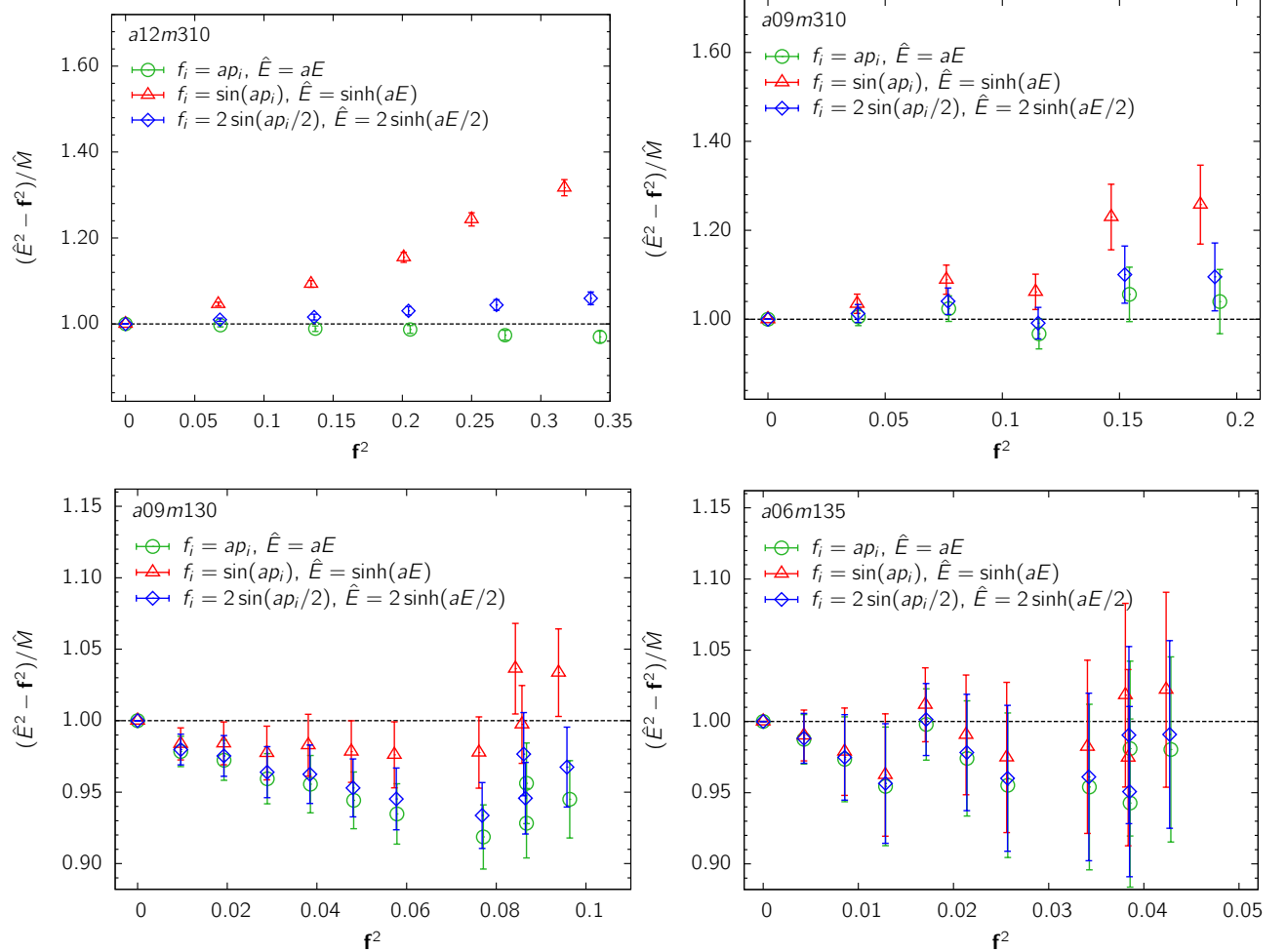


FIG. 30. Tests of the dispersion relation for the nucleon,  $(aE)^2 - \sum_i f_i^2 = (aM)^2$ , for the three cases  $f_i = ap_i$ ,  $\sin(ap_i)$  and  $2 \sin(ap_i/2)$ . Data for the  $a12m310$  and  $a09m310$  ensembles are shown in the top panels and for the two physical mass ensembles,  $a09m130$  and  $a06m135$ , in the bottom panels. The ideal behavior is a constant value given by the data at  $\mathbf{p} = 0$ .

Priors			0.15(10)	0.4(2)	0.8(6)	0.6(3)	0.6(4)	0.4(2)		
$\mathbf{n}^2$	$N_{2pt}$	$\mathcal{A}_0 \times 10^{11}$	$aE_0$	$r_1$	$a\Delta E_1$	$r_2$	$a\Delta E_2$	$r_3$	$a\Delta E_3$	$\chi^2/\text{DOF}$
0	2	03 - 15	6.86(11)	0.671(002)	1.011(186)	0.837(098)				0.916
	3	02 - 15	6.78(10)	0.670(002)	0.143(028)	0.450(038)	1.137(063)	0.563(075)		0.747
	4	02 - 15	6.75(10)	0.669(002)	0.137(030)	0.420(037)	0.732(038)	0.500(066)	0.518(066)	0.738
1	2	03 - 15	5.20(08)	0.719(002)	1.026(172)	0.807(092)				0.763
	3	02 - 15	5.15(08)	0.718(002)	0.152(029)	0.438(039)	1.204(066)	0.566(076)		0.652
	4	02 - 15	5.12(08)	0.718(002)	0.147(030)	0.409(038)	0.775(039)	0.502(067)	0.551(065)	0.620
2	2	03 - 15	3.93(08)	0.763(003)	1.008(151)	0.751(090)				0.802
	3	02 - 15	3.89(07)	0.762(002)	0.174(031)	0.400(042)	1.294(075)	0.604(079)		0.711
	4	02 - 15	3.86(08)	0.762(002)	0.169(033)	0.368(040)	0.826(043)	0.537(071)	0.609(065)	0.636
3	2	03 - 15	3.03(08)	0.806(003)	1.053(170)	0.744(104)				0.536
	3	02 - 15	3.00(06)	0.806(003)	0.176(029)	0.394(039)	1.376(077)	0.608(070)		0.522
	4	02 - 15	2.96(07)	0.805(003)	0.174(030)	0.357(037)	0.888(047)	0.550(064)	0.641(058)	0.426
4	2	03 - 15	2.30(09)	0.843(005)	1.085(173)	0.703(118)				1.652
	3	02 - 15	2.30(05)	0.844(003)	0.181(024)	0.384(033)	1.467(076)	0.598(058)		1.416
	4	02 - 15	2.27(06)	0.843(003)	0.181(025)	0.342(029)	0.958(050)	0.545(056)	0.675(051)	0.406(020)
5	2	03 - 15	1.76(09)	0.881(006)	1.106(161)	0.667(121)				0.697
	3	02 - 15	1.78(04)	0.883(003)	0.185(022)	0.377(031)	1.541(078)	0.592(056)		0.758
	4	02 - 15	1.75(05)	0.882(004)	0.186(023)	0.334(027)	1.014(053)	0.541(055)	0.703(048)	0.406(019)

TABLE XI. Results of the 2-, 3- and 4-state fits to the two-point nucleon correlator for the  $a12m310$  ensemble. The lattice momenta are  $\mathbf{p}a = 2\pi\mathbf{n}/L$  with  $\mathbf{n}^2$  listed in the first column. The third column gives the fit range  $t_{\min} - t_{\max}$ . Priors, given in the first row, were used for the multistate fit when the number of states  $N_{2pt} \geq 3$ .

Priors			0.4(3)	0.3(2)	1.0(8)	0.8(4)	0.8(6)	0.4(2)			
$n^2$	$N_{2\text{pt}}$		$\mathcal{A}_0 \times 10^{11}$	$aE_0$	$r_1$	$a\Delta E_1$	$r_2$	$a\Delta E_2$	$r_3$	$a\Delta E_3$	$\chi^2/\text{DOF}$
0	2	04 - 15	5.97(18)	0.612(003)	0.669(118)	0.529(100)					1.363
	3	02 - 15	5.75(22)	0.609(003)	0.400(067)	0.350(071)	1.461(171)	0.878(102)			0.885
	4	02 - 15	5.74(23)	0.609(003)	0.400(091)	0.349(085)	0.873(099)	0.775(117)	0.725(107)	0.405(010)	0.881
1	2	04 - 15	5.30(19)	0.630(003)	0.638(086)	0.475(092)					1.497
	3	02 - 15	5.05(26)	0.626(004)	0.417(065)	0.309(075)	1.573(178)	0.909(093)			0.945
	4	02 - 15	5.04(29)	0.626(004)	0.417(077)	0.306(089)	0.944(109)	0.806(104)	0.773(101)	0.402(010)	0.931
2	2	04 - 15	4.73(20)	0.647(004)	0.631(068)	0.440(088)					1.620
	3	02 - 15	4.50(24)	0.644(004)	0.441(067)	0.292(066)	1.661(188)	0.930(090)			1.047
	4	02 - 15	4.48(28)	0.644(005)	0.444(076)	0.288(079)	1.005(122)	0.831(100)	0.813(101)	0.399(010)	1.024
3	2	04 - 15	4.19(23)	0.664(005)	0.638(053)	0.404(087)					1.740
	3	02 - 15	3.99(21)	0.661(004)	0.475(072)	0.278(053)	1.761(201)	0.954(089)			1.164
	4	02 - 15	3.95(27)	0.660(005)	0.484(083)	0.272(066)	1.078(138)	0.860(098)	0.861(104)	0.397(010)	1.125
4	2	04 - 15	3.88(22)	0.684(005)	0.626(064)	0.421(100)					1.438
	3	02 - 15	3.71(20)	0.681(004)	0.445(074)	0.287(059)	1.777(209)	0.946(091)			0.973
	4	02 - 15	3.68(25)	0.681(005)	0.453(085)	0.280(071)	1.090(143)	0.854(101)	0.863(109)	0.396(010)	0.940
5	2	04 - 15	3.46(22)	0.700(006)	0.637(058)	0.396(095)					1.406
	3	02 - 15	3.35(17)	0.698(004)	0.467(075)	0.288(049)	1.846(220)	0.961(091)			1.003
	4	02 - 15	3.31(21)	0.698(005)	0.479(087)	0.282(060)	1.143(154)	0.874(102)	0.897(112)	0.394(009)	0.960

TABLE XII. Results of the 2-, 3- and 4-state fits to the two-point nucleon correlator for the a12m220L ensemble. The rest is the same as in Table. XI.

Priors			0.8(4)	0.3(2)	1.3(1.0)	0.70(35)	1.1(8)	0.4(2)			
$n^2$	$N_{2\text{pt}}$		$\mathcal{A}_0 \times 10^{11}$	$aE_0$	$r_1$	$a\Delta E_1$	$r_2$	$a\Delta E_2$	$r_3$	$a\Delta E_3$	$\chi^2/\text{DOF}$
0	2	05 - 20	13.3(1.2)	0.493(007)	0.943(097)	0.331(078)					1.268
	3	03 - 20	13.1(1.2)	0.492(006)	0.752(103)	0.284(074)	1.644(378)	0.688(083)			0.980
	4	03 - 20	13.1(1.4)	0.492(007)	0.796(105)	0.287(084)	1.187(261)	0.686(093)	1.018(187)	0.404(012)	0.976
1	2	05 - 20	11.5(1.0)	0.532(006)	0.948(107)	0.334(077)					1.281
	3	03 - 20	11.4(9)	0.531(005)	0.764(099)	0.294(062)	1.715(375)	0.713(073)			0.994
	4	03 - 20	11.3(9)	0.531(006)	0.803(101)	0.294(066)	1.269(264)	0.719(071)	1.090(171)	0.400(014)	0.976
2	2	05 - 20	10.3(9)	0.571(007)	0.927(146)	0.361(098)					1.383
	3	03 - 20	10.2(7)	0.571(005)	0.738(101)	0.321(066)	1.665(375)	0.712(069)			1.065
	4	03 - 20	10.1(8)	0.570(006)	0.773(107)	0.316(070)	1.271(264)	0.730(057)	1.100(160)	0.401(014)	1.048
3	2	05 - 20	6.75(2.67)	0.586(023)	1.210(662)	0.229(096)					0.738
	3	03 - 20	7.57(71)	0.594(006)	0.820(161)	0.226(036)	1.894(326)	0.691(071)			0.618
	4	03 - 20	7.22(60)	0.591(006)	0.900(152)	0.213(034)	1.413(243)	0.672(085)	1.135(178)	0.393(014)	0.586
4	2	05 - 20	8.54(1.33)	0.646(014)	0.985(850)	0.484(381)					0.653
	3	03 - 20	8.18(74)	0.642(008)	0.654(105)	0.362(099)	1.621(338)	0.677(065)			0.506
	4	03 - 20	7.93(1.15)	0.640(011)	0.667(131)	0.326(149)	1.305(273)	0.707(045)	1.100(157)	0.399(015)	0.493
5	2	05 - 20	6.88(1.79)	0.670(020)	0.858(317)	0.374(326)					0.491
	3	03 - 20	6.86(75)	0.670(009)	0.672(112)	0.338(097)	1.646(329)	0.685(061)			0.383
	4	03 - 20	6.54(1.16)	0.667(013)	0.694(148)	0.293(138)	1.341(281)	0.710(046)	1.121(160)	0.397(015)	0.365

TABLE XIII. Results of the 2-, 3- and 4-state fits to the two-point nucleon correlator for the a09m310 ensemble. The rest is the same as in Table. XI.

Priors			0.8(4)	0.3(2)	1.7(1.2)	0.6(3)	1.5(1.0)	0.4(2)			
$n^2$	$N_{2\text{pt}}$		$A_0 \times 10^{11}$	$E_0$	$r_1$	$\Delta E_1$	$r_2$	$\Delta E_2$	$r_3$	$\Delta E_3$	$\chi^2/\text{DOF}$
0 0	2	05 - 20	11.5(10)	0.452(006)	1.139(133)	0.361(078)					0.753
	3	03 - 20	11.0(10)	0.450(006)	0.805(116)	0.270(054)	2.247(423)	0.668(077)			0.541
	4	03 - 20	10.8(11)	0.448(007)	0.847(123)	0.264(063)	1.518(292)	0.630(085)	1.414(263)	0.405(014)	0.522
1	2	05 - 20	10.6(11)	0.470(007)	1.124(122)	0.340(083)					0.783
	3	03 - 20	9.85(1.04)	0.466(007)	0.804(139)	0.239(055)	2.383(424)	0.668(073)			0.546
	4	03 - 20	9.47(1.27)	0.464(008)	0.854(153)	0.225(067)	1.623(293)	0.619(088)	1.455(258)	0.400(016)	0.516
2	2	05 - 20	9.88(1.15)	0.489(008)	1.099(124)	0.333(090)					0.860
	3	03 - 20	9.21(1.02)	0.485(007)	0.787(146)	0.233(055)	2.416(425)	0.670(071)			0.607
	4	03 - 20	8.75(1.19)	0.482(007)	0.848(161)	0.213(063)	1.664(288)	0.620(086)	1.477(253)	0.397(016)	0.573
3	2	05 - 20	9.18(1.28)	0.506(010)	1.068(130)	0.319(099)					0.935
	3	03 - 20	8.61(97)	0.503(007)	0.770(155)	0.225(052)	2.457(419)	0.673(070)			0.677
	4	03 - 20	8.07(97)	0.500(007)	0.847(161)	0.202(053)	1.714(271)	0.624(084)	1.505(242)	0.394(016)	0.639
4	2	05 - 20	8.68(1.32)	0.524(011)	1.072(139)	0.327(111)					0.890
	3	03 - 20	8.38(95)	0.522(007)	0.755(145)	0.248(060)	2.375(430)	0.670(072)			0.661
	4	03 - 20	7.89(1.01)	0.519(008)	0.825(162)	0.222(060)	1.675(288)	0.633(081)	1.497(249)	0.397(015)	0.627
5	2	05 - 20	7.65(1.52)	0.536(013)	1.115(210)	0.292(103)					1.027
	3	03 - 20	7.56(77)	0.537(007)	0.793(160)	0.232(043)	2.445(397)	0.674(068)			0.779
	4	03 - 20	7.11(69)	0.533(006)	0.876(160)	0.211(041)	1.724(267)	0.635(080)	1.529(235)	0.395(015)	0.738

TABLE XIV. Results of the 2-, 3- and 4-state fits to the two-point nucleon correlator for the a09m220 ensemble. The rest is the same as in Table. XI.

Priors			1.0(5)	0.20(15)	2.0(1.5)	0.6(3)	1.7(1.2)	0.4(2)			
$n^2$	$N_{2\text{pt}}$		$\mathcal{A}_0 \times 10^{11}$	$aE_0$	$r_1$	$a\Delta E_1$	$r_2$	$a\Delta E_2$	$r_3$	$a\Delta E_3$	$\chi^2/\text{DOF}$
0	2	06 - 20	9.66(53)	0.419(004)	1.332(117)	0.353(049)					0.627
	3	04 - 20	8.79(67)	0.414(005)	1.032(090)	0.253(039)	2.736(519)	0.703(059)			0.684
	4	04 - 20	8.81(67)	0.414(005)	1.065(085)	0.259(039)	2.093(379)	0.700(057)	1.878(210)	0.393(020)	0.637
1	2	06 - 20	8.74(57)	0.427(004)	1.326(078)	0.312(041)					0.364
	3	04 - 20	7.83(67)	0.421(005)	1.120(113)	0.226(032)	3.001(530)	0.710(058)			0.464
	4	04 - 20	7.84(70)	0.421(005)	1.148(111)	0.231(033)	2.263(404)	0.699(063)	1.953(224)	0.385(023)	0.399
2	2	06 - 20	8.21(57)	0.437(004)	1.349(077)	0.300(038)					0.303
	3	04 - 20	7.38(61)	0.431(005)	1.168(119)	0.223(027)	3.117(528)	0.720(054)			0.451
	4	04 - 20	7.37(64)	0.431(005)	1.196(119)	0.226(029)	2.360(405)	0.709(057)	2.001(219)	0.380(024)	0.377
3	2	06 - 20	7.61(63)	0.445(005)	1.390(090)	0.284(037)					0.472
	3	04 - 20	6.80(56)	0.440(005)	1.241(135)	0.213(023)	3.257(534)	0.724(051)			0.594
	4	04 - 20	6.77(60)	0.440(005)	1.273(138)	0.215(024)	2.465(417)	0.710(056)	2.050(224)	0.374(025)	0.510
4	2	06 - 20	7.23(64)	0.455(005)	1.409(102)	0.278(037)					0.595
	3	04 - 20	6.47(52)	0.450(004)	1.271(140)	0.211(020)	3.325(529)	0.731(048)			0.718
	4	04 - 20	6.43(55)	0.450(005)	1.305(144)	0.212(021)	2.526(414)	0.717(052)	2.079(220)	0.370(025)	0.628
5	2	06 - 20	6.68(67)	0.463(006)	1.474(132)	0.265(035)					0.493
	3	04 - 20	6.01(45)	0.459(004)	1.348(146)	0.206(017)	3.444(525)	0.736(045)			0.692
	4	04 - 20	5.96(48)	0.458(004)	1.385(151)	0.207(017)	2.623(416)	0.722(049)	2.127(219)	0.365(026)	0.593
6	2	06 - 20	6.18(78)	0.471(007)	1.529(188)	0.253(036)					0.529
	3	04 - 20	5.60(40)	0.468(004)	1.401(153)	0.198(014)	3.514(524)	0.730(046)			0.711
	4	04 - 20	5.53(41)	0.467(004)	1.446(158)	0.199(014)	2.675(422)	0.715(051)	2.147(223)	0.362(026)	0.607
8	2	06 - 20	5.18(90)	0.485(010)	1.754(331)	0.235(034)					1.092
	3	04 - 20	4.99(31)	0.485(004)	1.522(156)	0.197(010)	3.623(508)	0.740(041)			1.280
	4	04 - 20	4.92(31)	0.484(004)	1.573(159)	0.198(011)	2.786(409)	0.728(044)	2.206(214)	0.355(026)	1.165
9	2	06 - 20	5.10(1.04)	0.497(012)	1.688(378)	0.235(041)					1.098
	3	04 - 20	4.90(30)	0.497(004)	1.445(159)	0.193(011)	3.620(502)	0.735(042)			1.248
	4	04 - 20	4.82(30)	0.496(004)	1.503(160)	0.193(011)	2.783(407)	0.722(046)	2.202(215)	0.356(026)	1.134
9'	2	06 - 20	5.91(87)	0.505(009)	1.456(185)	0.272(053)					0.619
	3	04 - 20	5.38(38)	0.502(004)	1.278(156)	0.209(015)	3.236(498)	0.728(044)			0.787
	4	04 - 20	5.30(39)	0.501(004)	1.330(158)	0.208(016)	2.506(394)	0.718(045)	2.067(207)	0.371(024)	0.703
10	2	06 - 20	5.39(85)	0.511(010)	1.557(235)	0.258(046)					0.696
	3	04 - 20	5.02(34)	0.509(004)	1.360(158)	0.206(014)	3.333(493)	0.737(041)			0.931
	4	04 - 20	4.95(34)	0.508(004)	1.411(159)	0.206(014)	2.588(391)	0.728(042)	2.112(204)	0.366(024)	0.838

TABLE XV. Results of the 2-, 3- and 4-state fits to the two-point nucleon correlator for the a09m130 ensemble.  $n^2 = 9$  has two combinations (2, 2, 1) and (3, 0, 0) labeled 9 and 9', respectively. The rest is the same as in Table. XI.

Priors			1.0(5)	0.16(10)	2.4(1.5)	0.3(2)	2.2(1.5)	0.3(2)	$\chi^2/\text{DOF}$	
$n^2$	$N_{2\text{pt}}$		$\mathcal{A}_0 \times 10^{12}$	$aE_0$	$r_1$	$a\Delta E_1$	$r_2$	$a\Delta E_2$	$r_3$	$a\Delta E_3$
0	2	10 - 30	5.56(35)	0.326(003)	1.362(097)	0.199(026)				1.371
	3	07 - 30	5.46(39)	0.325(003)	0.936(109)	0.163(028)	3.368(597)	0.356(035)		1.268
	4	07 - 30	5.40(43)	0.325(003)	0.964(116)	0.161(031)	2.554(366)	0.338(037)	2.323(334)	0.276(042)
1	2	10 - 30	5.17(29)	0.352(002)	1.444(118)	0.209(027)				1.091
	3	07 - 30	5.09(29)	0.352(002)	1.022(110)	0.175(024)	3.096(598)	0.348(038)		1.010
	4	07 - 30	5.05(31)	0.352(002)	1.054(116)	0.174(026)	2.401(399)	0.334(040)	2.269(312)	0.292(041)
2	2	10 - 30	4.74(31)	0.376(003)	1.507(135)	0.211(030)				0.819
	3	07 - 30	4.62(30)	0.376(003)	1.044(118)	0.172(024)	2.889(609)	0.333(043)		0.765
	4	07 - 30	4.57(32)	0.375(003)	1.076(125)	0.171(027)	2.263(419)	0.319(044)	2.180(316)	0.307(042)
3	2	10 - 30	4.36(37)	0.399(004)	1.601(175)	0.218(038)				0.443
	3	07 - 30	4.12(34)	0.397(003)	1.046(131)	0.164(024)	2.730(592)	0.315(046)		0.416
	4	07 - 30	4.04(40)	0.396(004)	1.074(138)	0.159(030)	2.159(423)	0.298(046)	2.099(324)	0.320(040)
4	2	10 - 30	4.18(45)	0.423(005)	1.504(234)	0.224(055)				0.884
	3	07 - 30	4.05(32)	0.422(004)	0.968(109)	0.176(025)	2.553(558)	0.303(050)		0.769
	4	07 - 30	3.94(37)	0.420(004)	1.009(111)	0.169(030)	2.107(416)	0.296(045)	2.022(318)	0.324(038)
5	2	10 - 30	3.35(56)	0.437(007)	1.623(187)	0.186(044)				0.867
	3	07 - 30	3.27(31)	0.437(004)	1.107(170)	0.149(017)	2.703(520)	0.307(046)		0.756
	4	07 - 30	3.12(33)	0.435(004)	1.149(182)	0.139(020)	2.179(357)	0.287(049)	2.083(316)	0.318(036)

TABLE XVI. Results of the 2-, 3- and 4-state fits to the two-point nucleon correlator for the a06m310 ensemble. The rest is the same as in Table. XI.

Priors			2.0(1.0)	0.25(20)	3.0(1.5)	0.3(2)	2.8(1.8)	0.3(2)	$\chi^2/\text{DOF}$	
$n^2$	$N_{2\text{pt}}$		$\mathcal{A}_0 \times 10^{11}$	$aE_0$	$r_1$	$a\Delta E_1$	$r_2$	$a\Delta E_2$	$r_3$	$a\Delta E_3$
0	2	10 - 30	10.8(4)	0.305(002)	2.900(348)	0.286(025)				1.774
	3	07 - 30	10.6(4)	0.304(002)	2.035(225)	0.249(019)	3.919(681)	0.342(021)		1.591
	4	07 - 30	10.5(4)	0.304(002)	2.066(240)	0.245(021)	3.185(345)	0.344(022)	3.078(406)	0.267(048)
1	2	10 - 30	10.0(4)	0.319(002)	2.842(265)	0.266(022)				1.432
	3	07 - 30	9.74(42)	0.318(002)	1.998(208)	0.228(019)	4.119(680)	0.341(022)		1.342
	4	07 - 30	9.62(46)	0.317(002)	2.041(215)	0.226(021)	3.253(325)	0.340(024)	3.137(426)	0.257(049)
2	2	10 - 30	9.38(46)	0.333(002)	2.869(238)	0.256(021)				1.356
	3	07 - 30	9.10(45)	0.332(002)	2.041(194)	0.218(019)	4.217(680)	0.343(021)		1.288
	4	07 - 30	8.95(50)	0.331(002)	2.083(200)	0.214(021)	3.302(321)	0.340(024)	3.203(439)	0.250(049)
3	2	10 - 30	8.97(53)	0.347(003)	2.898(242)	0.250(023)				1.162
	3	07 - 30	8.60(52)	0.346(003)	2.019(189)	0.208(020)	4.249(701)	0.336(022)		1.130
	4	07 - 30	8.38(61)	0.344(003)	2.051(202)	0.202(023)	3.313(332)	0.329(026)	3.195(461)	0.250(051)
4	2	10 - 30	8.69(66)	0.361(004)	2.843(242)	0.244(026)				0.824
	3	07 - 30	8.39(60)	0.360(003)	1.958(178)	0.203(021)	4.306(702)	0.336(021)		0.896
	4	07 - 30	8.02(77)	0.358(004)	1.979(188)	0.192(026)	3.378(335)	0.327(025)	3.268(495)	0.240(054)
5	2	10 - 30	8.18(67)	0.374(004)	2.888(225)	0.237(025)				0.885
	3	07 - 30	7.95(58)	0.373(003)	2.049(182)	0.200(019)	4.250(693)	0.337(021)		0.951
	4	07 - 30	7.59(73)	0.371(004)	2.080(192)	0.190(024)	3.360(342)	0.328(025)	3.258(488)	0.243(053)

TABLE XVII. Results of the 2-, 3- and 4-state fits to the two-point nucleon correlator for the a06m220 ensemble. The rest is the same as in Table. XI.

Priors			$1.3(7)$	$0.20(15)$	$1.3(1.0)$	$0.3(2)$	$1.1(9)$	$0.3(2)$	$\chi^2/\text{DOF}$
$n^2$	$N_{\text{2pt}}$	$\mathcal{A}_0 \times 10^{16}$	$aE_0$	$r_1$	$a\Delta E_1$	$r_2$	$a\Delta E_2$	$r_3$	$a\Delta E_3$
0	2	08 - 30	3.03(21)	0.276(004)	1.867(235)	0.283(042)			1.089
	3	06 - 30	2.96(18)	0.275(003)	1.365(113)	0.242(026)	1.375(429)	0.313(047)	0.980
	4	06 - 30	2.92(19)	0.274(003)	1.383(169)	0.237(031)	1.161(338)	0.323(027)	0.976
1	2	08 - 30	2.78(23)	0.282(004)	1.753(160)	0.254(039)			1.302
	3	06 - 30	2.73(23)	0.282(004)	1.275(142)	0.218(036)	1.680(506)	0.327(036)	1.158
	4	06 - 30	2.67(27)	0.280(005)	1.262(182)	0.206(044)	1.392(382)	0.318(029)	1.205(222)
2	2	08 - 30	2.58(24)	0.288(004)	1.737(130)	0.238(036)			1.123
	3	06 - 30	2.52(25)	0.288(005)	1.258(141)	0.200(037)	1.825(519)	0.330(033)	1.011
	4	06 - 30	2.43(32)	0.286(006)	1.243(166)	0.185(048)	1.499(387)	0.314(032)	1.256(238)
3	2	08 - 30	2.39(24)	0.294(005)	1.781(124)	0.227(034)			1.155
	3	06 - 30	2.31(26)	0.293(005)	1.292(141)	0.186(036)	1.905(522)	0.329(033)	1.043
	4	06 - 30	2.20(36)	0.291(006)	1.283(162)	0.169(048)	1.566(394)	0.306(036)	1.288(250)
4	2	08 - 30	2.44(23)	0.305(005)	1.745(144)	0.245(039)			1.186
	3	06 - 30	2.44(19)	0.305(004)	1.323(124)	0.219(028)	1.611(423)	0.333(033)	1.055
	4	06 - 30	2.38(21)	0.304(004)	1.319(151)	0.209(032)	1.355(323)	0.329(025)	1.195(190)
5	2	08 - 30	2.24(26)	0.310(006)	1.749(135)	0.226(039)			0.904
	3	06 - 30	2.22(24)	0.310(005)	1.288(142)	0.194(034)	1.836(474)	0.337(030)	0.847
	4	06 - 30	2.12(29)	0.308(006)	1.285(164)	0.179(040)	1.528(351)	0.322(029)	1.285(224)
6	2	08 - 30	2.07(30)	0.315(007)	1.800(178)	0.215(040)			1.143
	3	06 - 30	2.03(28)	0.315(006)	1.323(180)	0.181(034)	1.953(479)	0.340(029)	1.067
	4	06 - 30	1.91(32)	0.313(007)	1.342(217)	0.164(036)	1.614(337)	0.320(032)	1.339(228)
8	2	08 - 30	1.91(36)	0.329(009)	1.805(222)	0.214(049)			1.041
	3	06 - 30	1.89(28)	0.329(007)	1.313(189)	0.180(036)	1.894(466)	0.334(030)	0.968
	4	06 - 30	1.74(31)	0.326(007)	1.344(248)	0.158(034)	1.613(324)	0.313(034)	1.327(226)
9	2	08 - 30	1.73(44)	0.333(012)	1.869(411)	0.199(049)			1.386
	3	06 - 30	1.77(30)	0.334(008)	1.336(253)	0.172(032)	2.020(456)	0.338(029)	1.268
	4	06 - 30	1.61(28)	0.331(007)	1.394(311)	0.151(024)	1.699(282)	0.316(034)	1.386(217)
9'	2	08 - 30	1.85(37)	0.335(010)	1.754(262)	0.212(051)			0.777
	3	06 - 30	1.94(27)	0.338(007)	1.264(176)	0.197(038)	1.848(406)	0.341(028)	0.760
	4	06 - 30	1.81(31)	0.335(008)	1.264(235)	0.173(038)	1.602(300)	0.328(027)	1.333(211)
10	2	08 - 30	1.76(38)	0.342(010)	1.757(286)	0.207(052)			1.018
	3	06 - 30	1.85(27)	0.345(007)	1.265(181)	0.192(039)	1.865(416)	0.343(028)	0.974
	4	06 - 30	1.72(30)	0.342(008)	1.274(245)	0.168(037)	1.615(301)	0.329(028)	1.344(210)

TABLE XVIII. Results of the 2-, 3- and 4-state fits to the two-point nucleon correlator for the a06m130 AMA ensemble.  $n^2 = 9$  has two combinations (2, 2, 1) and (3, 0, 0) labeled 9 and 9', respectively. The rest is the same as in Table. XI.

## Appendix B: Fits to three-point functions

This appendix contains plots of fits to the data for three-point functions from which the form factors are extracted. The data for the ratio  $\mathcal{R}_{53}$ , defined in Eq. (18), is plotted in Figs. 31 and 32 for the  $a = 0.12$  and  $0.09$  fm ensembles. The horizontal band in these figures gives the  $\tau \rightarrow \infty$  value defined in Eq. (21).

In Figs. 33, 34, and 35 we show the data for the ratio  $\mathcal{R}_{53}$  defined in Eq. (18) versus the operator insertion time  $t$  shifted by  $\tau/2$ . The data for the ratio  $\mathcal{R}_{53}$  with  $q_3 = 0$  gives the form factor  $G_A$  while  $\mathcal{R}_{51}$  gives  $\tilde{G}_P$ . In the right panels of Figs. 33 and 35, we also show the fits used to extract the pseudoscalar form factor  $G_P(Q^2)$  using Eqs. (18) and (22). In each case, the horizontal band gives the value in the limit  $t \rightarrow \infty$ ,  $\tau \rightarrow \infty$  and  $\tau - t \rightarrow \infty$  as defined in Eqs. (21) and (22).

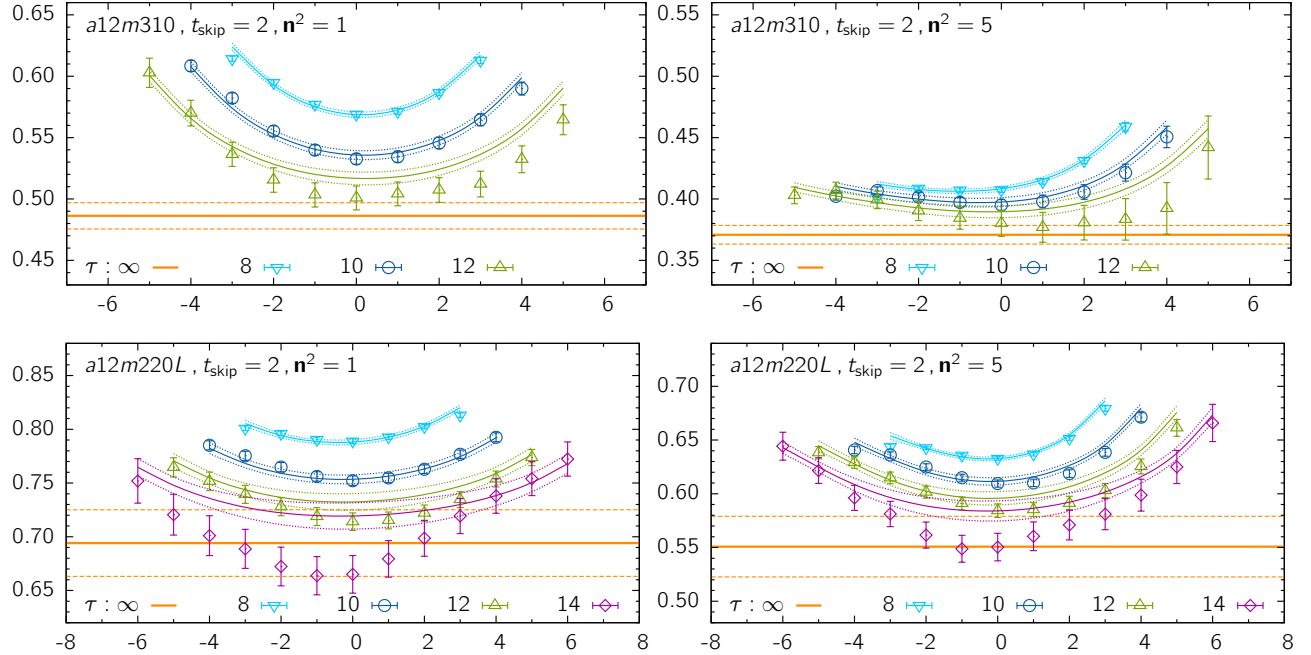


FIG. 31. The three-point data for  $\mathcal{R}_{53}$  defined in Eq. (18) versus the operator insertion time  $t$  shifted by  $\tau/2$ . The label gives the values of  $t_{\text{skip}}$  and  $\tau$  used in the fits. Prediction of the 2-state fit for various values of  $\tau$  is shown in the same color as the data. The result for the matrix elements in the  $\tau \rightarrow \infty$  limit is shown by the horizontal band. The figures on top are for the  $a12m310$  ensemble, and those on the bottom for the  $a12m220L$  ensemble. The plots on the left are for the lowest momenta  $\mathbf{p} = (1, 0, 0)2\pi/La$ , while those on the right are for  $\mathbf{p} = (2, 1, 0)2\pi/La$ .

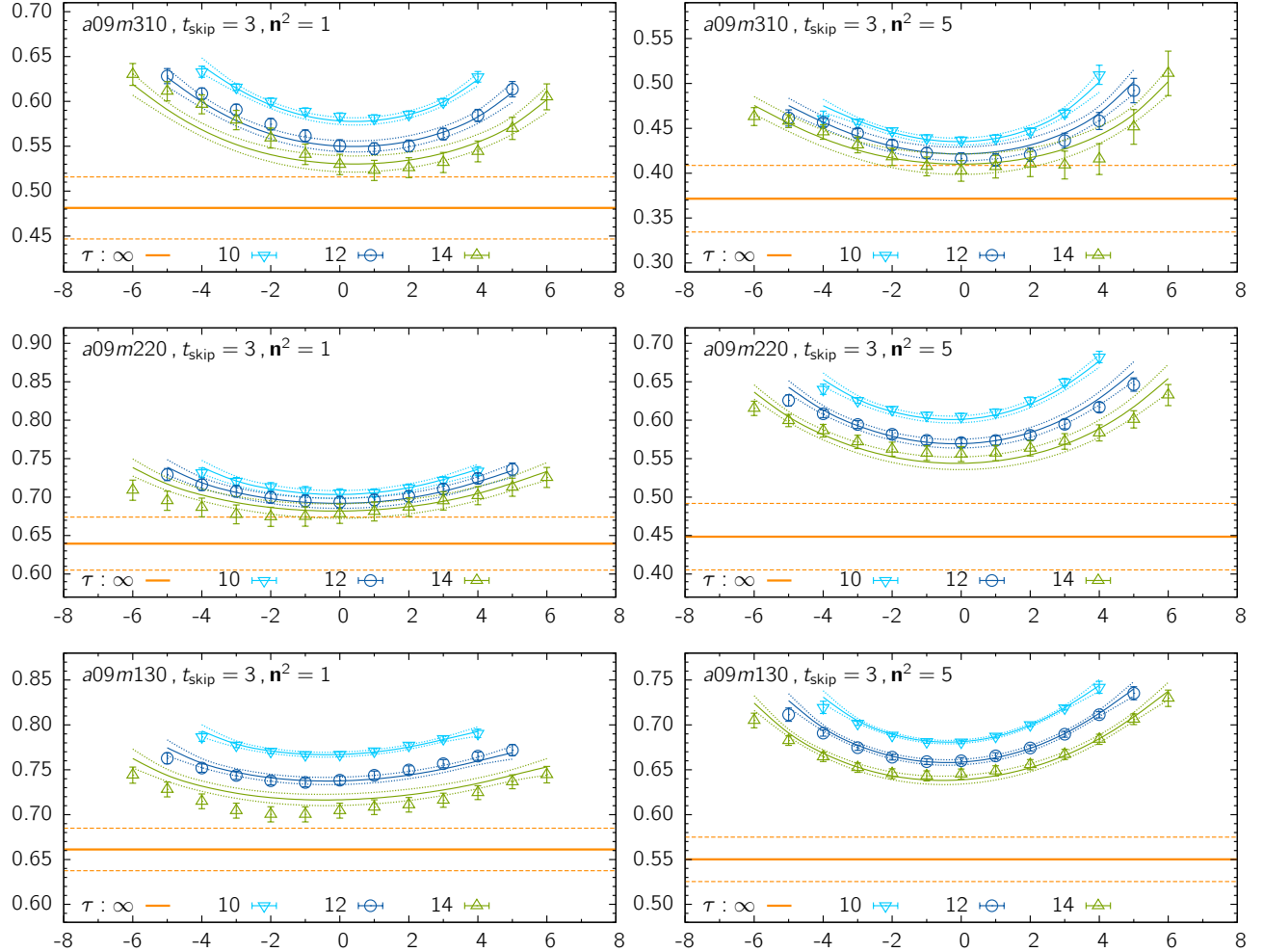


FIG. 32. The three-point data for  $\mathcal{R}_{53}$  defined in (18) versus the operator insertion time  $t$  shifted by  $\tau/2$ . The label gives the value of  $t_{\text{skip}}$  and  $\tau$  used in the fits. Prediction of the 2-state fit for various values of  $\tau$  is shown in the same color as the data. The result for the matrix elements in the  $\tau \rightarrow \infty$  limit is shown by the horizontal band. The plots in the top row are for the  $a09m310$  ensemble, middle are for the  $a09m220$ , and those on the bottom row for the  $a09m130$  ensemble. The plots on the left are for the lowest momenta  $\mathbf{p} = (1, 0, 0)2\pi/La$ , while those on the right are for the highest,  $\mathbf{p} = (2, 1, 0)2\pi/La$ .

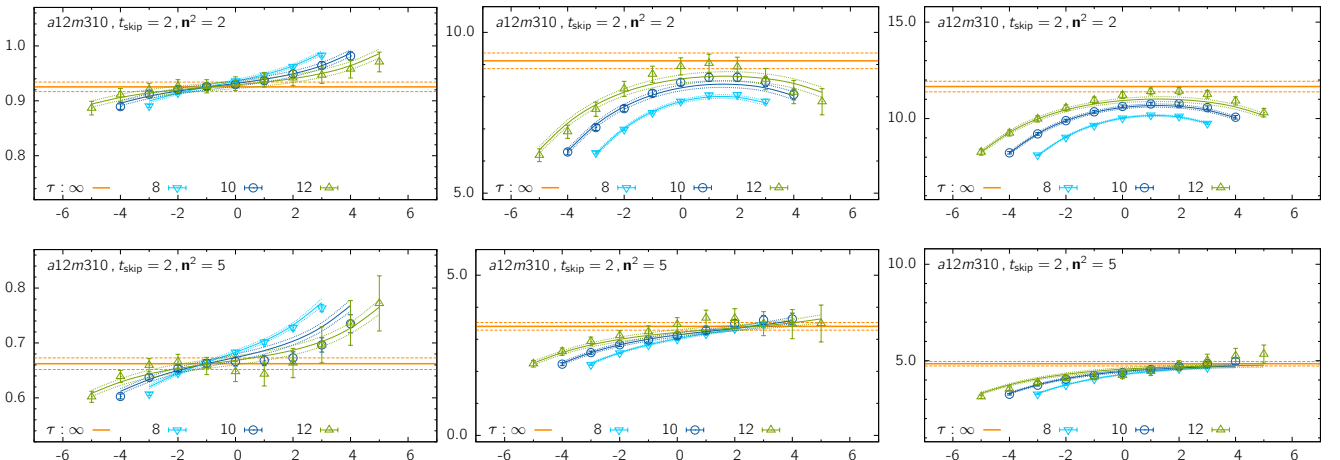


FIG. 33. Plots of the ratios that directly give the form factors:  $G_A$  from  $\mathcal{R}_{53}$  with  $q_3 = 0$  (left),  $\tilde{G}_P$  from  $\mathcal{R}_{51}$  (middle), and the pseudoscalar  $G_P$  (right) versus the operator insertion time  $t - \tau/2$  for the  $a12m310$  ensemble. The top row shows data for  $\mathbf{p}^2 = 2(2\pi/La)^2$  and the bottom row for  $\mathbf{p}^2 = 5(2\pi/La)^2$ .

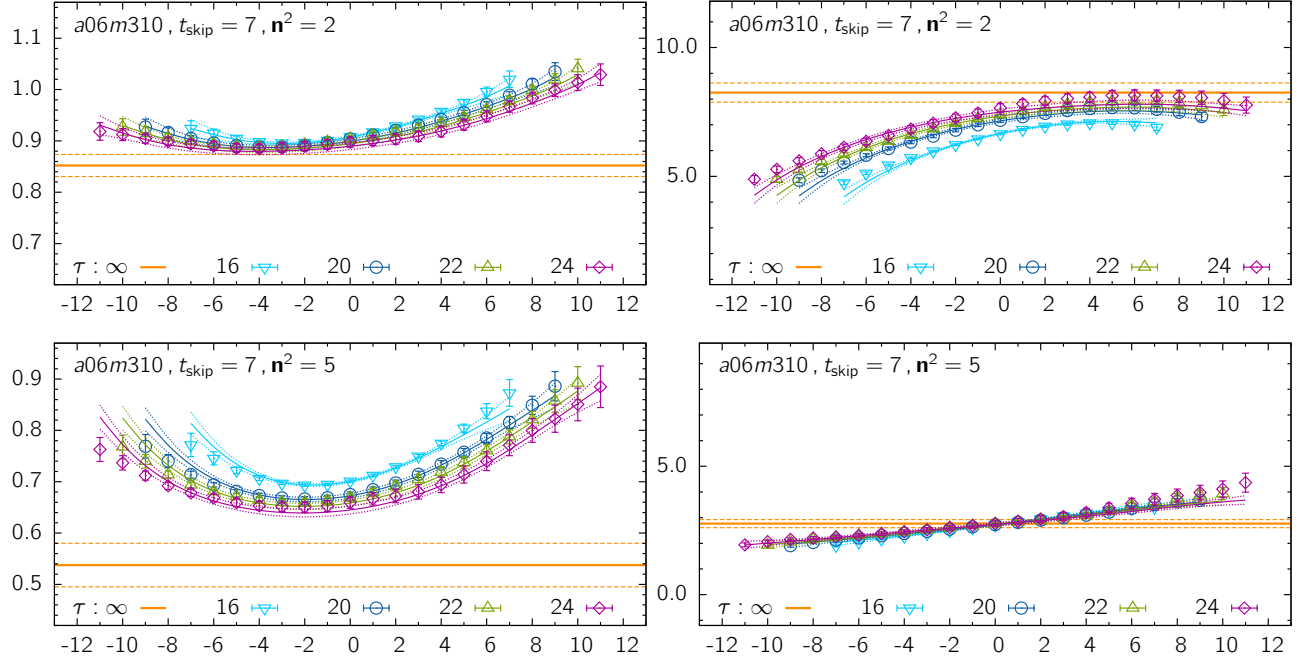


FIG. 34. Plots of the ratios that directly give the form factors:  $G_A$  from  $\mathcal{R}_{53}$  with  $q_3 = 0$  (left) and  $\tilde{G}_P$  from  $\mathcal{R}_{51}$  (right) versus the operator insertion time  $t$  shifted by  $\tau/2$  for the  $a06m310$  ensemble. Data for  $G_P(Q^2)$  has not been analyzed for this ensemble. The top row shows data for  $\mathbf{p}^2 = 2(2\pi/La)^2$  and the bottom row for  $\mathbf{p}^2 = 5(2\pi/La)^2$ .

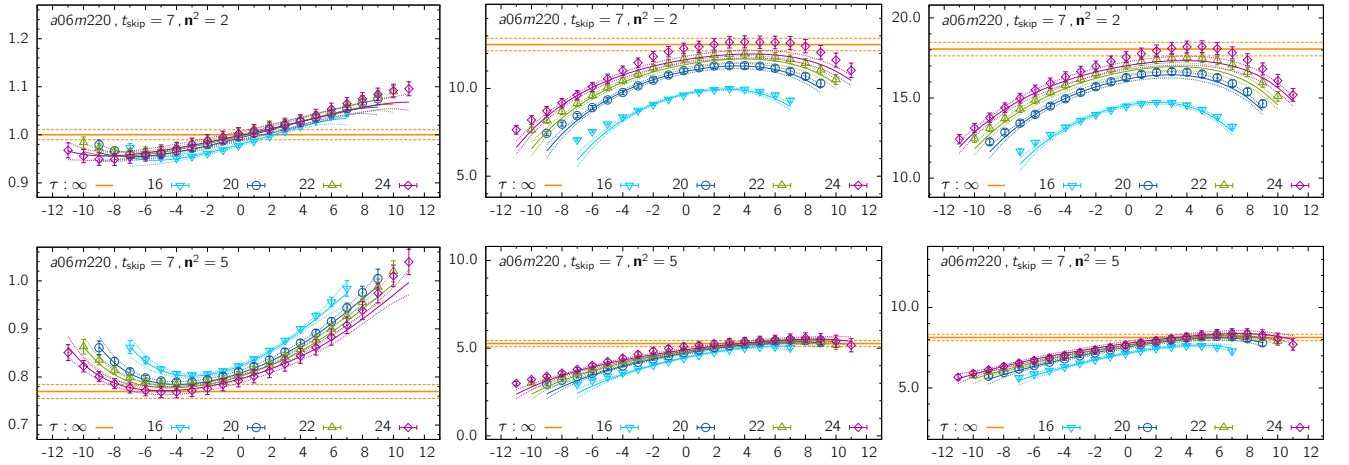


FIG. 35. Plots of the ratios that directly give the form factors:  $G_A$  from  $\mathcal{R}_{53}$  with  $q_3 = 0$  (left),  $\tilde{G}_P$  from  $\mathcal{R}_{51}$  (middle), and the pseudoscalar  $G_P$  (right) versus the operator insertion time  $t$  shifted by  $\tau/2$  for the  $a06m220$  ensemble. The top row shows data for  $\mathbf{p}^2 = 2(2\pi/La)^2$  and the bottom row for  $\mathbf{p}^2 = 5(2\pi/La)^2$ .

---

[1] Y. Fukuda *et al.* (Super-Kamiokande), Phys. Rev. Lett. **81**, 1562 (1998), arXiv:hep-ex/9807003 [hep-ex].

[2] Q. R. Ahmad *et al.* (SNO), Phys. Rev. Lett. **87**, 071301 (2001), arXiv:nucl-ex/0106015 [nucl-ex].

[3] Q. R. Ahmad *et al.* (SNO), Phys. Rev. Lett. **89**, 011301 (2002), arXiv:nucl-ex/0204008 [nucl-ex].

[4] Philip Ball, “Focus Nobel Prize–Neutrinos Oscillate,” Physics Today, <https://physics.aps.org/articles/v8/97>.

[5] C. Patrignani *et al.* (Particle Data Group), Chin. Phys. **C40**, 100001 (2016).

[6] Wikipedia List of Neutrino Experiments, “Neutrino Experiments,” [https://en.wikipedia.org/wiki/List\\_of\\_neutrino\\_experiments](https://en.wikipedia.org/wiki/List_of_neutrino_experiments).

[7] A. S. Meyer *et al.*, Phys. Rev. **D93**, 113015 (2016), arXiv:1603.03048 [hep-ph].

[8] J. Carlson, S. Gandolfi, F. Pederiva, S. C. Pieper, R. Schiavilla, K. E. Schmidt, and R. B. Wiringa, Rev. Mod. Phys. **87**, 1067 (2015), arXiv:1412.3081 [nucl-th].

[9] A. A. Aguilar-Arevalo *et al.* (MiniBooNE), Phys. Rev. **D81**, 092005 (2010), arXiv:1002.2680 [hep-ex].

[10] T. Bhattacharya, V. Cirigliano, S. D. Cohen, A. Filipuzzi, M. Gonzalez-Alonso, *et al.*, Phys. Rev. **D85**, 054512 (2012), arXiv:1110.6448 [hep-ph].

[11] E. Follana *et al.* (HPQCD Collaboration, UKQCD Collaboration), Phys. Rev. **D75**, 054502 (2007), arXiv:hep-lat/0610092 [hep-lat].

[12] A. Bazavov *et al.* (MILC Collaboration), Phys. Rev. **D87**, 054505 (2013), arXiv:1212.4768 [hep-lat].

[13] V. Bernard, L. Elouadrhiri, and U.-G. Meissner, J. Phys. **G28**, R1 (2002), arXiv:hep-ph/0107088 [hep-ph].

[14] R. A. Smith and E. J. Moniz, Nucl. Phys. **B43**, 605 (1972), [Erratum: Nucl. Phys. B101, 547 (1975)].

[15] R. J. Hill and G. Paz, Phys. Rev. **D82**, 113005 (2010), arXiv:1008.4619 [hep-ph].

[16] B. Bhattacharya, R. J. Hill, and G. Paz, Phys. Rev. **D84**, 073006 (2011), arXiv:1108.0423 [hep-ph].

[17] G. Lee, J. R. Arrington, and R. J. Hill, *Proceedings, Meeting of the APS Division of Particles and Fields (DPF 2015): Ann Arbor, Michigan, USA, 4-8 Aug 2015*, Phys. Rev. **D92**, 013013 (2015), arXiv:1505.01489 [hep-ph].

[18] M. L. Goldberger and S. B. Treiman, Phys. Rev. **111**, 354 (1958).

[19] T. Bhattacharya, V. Cirigliano, S. Cohen, R. Gupta, A. Joseph, H.-W. Lin, and B. Yoon (PNDME), Phys. Rev. **D92**, 094511 (2015), arXiv:1506.06411 [hep-lat].

[20] V. A. Andreev *et al.* (MuCap), Phys. Rev. Lett. **110**, 012504 (2013), arXiv:1210.6545 [nucl-ex].

[21] V. A. Andreev *et al.* (MuCap), Phys. Rev. **C91**, 055502 (2015), arXiv:1502.00913 [nucl-ex].

[22] M. R. Schindler, T. Fuchs, J. Gegelia, and S. Scherer, Phys. Rev. **C75**, 025202 (2007), arXiv:nucl-th/0611083 [nucl-th].

[23] V. Baru, C. Hanhart, M. Hoferichter, B. Kubis, A. Nogga, and D. R. Phillips, Nucl. Phys. **A872**, 69 (2011), arXiv:1107.5509 [nucl-th].

[24] R. G. Edwards and B. Joo (SciDAC Collaboration, LHPC Collaboration, UKQCD Collaboration), Nucl. Phys. Proc. Suppl. **140**, 832 (2005), arXiv:hep-lat/0409003 [hep-lat].

[25] T. Bhattacharya, V. Cirigliano, S. Cohen, R. Gupta, H.-W. Lin, and B. Yoon, Phys. Rev. **D94**, 054508 (2016), arXiv:1606.07049 [hep-lat].

[26] A. Hasenfratz and F. Knechtli, Phys. Rev. **D64**, 034504 (2001), arXiv:hep-lat/0103029 [hep-lat].

[27] B. Sheikholeslami and R. Wohlert, Nucl. Phys. **B259**, 572 (1985).

[28] G. S. Bali, S. Collins, and A. Schäfer, Comput. Phys. Commun. **181**, 1570 (2010), arXiv:0910.3970 [hep-lat].

[29] T. Blum, T. Izubuchi, and E. Shintani, Phys. Rev. **D88**, 094503 (2013), arXiv:1208.4349 [hep-lat].

[30] B. Yoon *et al.*, Phys. Rev. **D95**, 074508 (2017), arXiv:1611.07452 [hep-lat].

[31] M. Schmelling, Phys. Scripta **51**, 676 (1995).

[32] C. Alexandrou, M. Constantinou, K. Hadjyiannakou, K. Jansen, C. Kallidonis, G. Koutsou, and A. Vaquero Aviles-Casco, (2017), arXiv:1705.03399 [hep-lat].

[33] S. Capitani, M. Della Morte, D. Djukanovic, G. M. von Hippel, J. Hua, B. Jger, P. M. Junnarkar, H. B. Meyer, T. D. Rae, and H. Wittig, (2017), arXiv:1705.06186 [hep-lat].

[34] G. S. Bali, S. Collins, B. Glssle, M. Gckeler, J. Najjar, *et al.*, Phys. Rev. **D91**, 054501 (2015), arXiv:1412.7336 [hep-lat].

[35] T. Bhattacharya, R. Gupta, W. Lee, S. R. Sharpe, and J. M. S. Wu, Phys. Rev. **D73**, 034504 (2006), arXiv:hep-lat/0511014 [hep-lat].

[36] J. Bulava, M. Della Morte, J. Heitger, and C. Witemeier (ALPHA), Nucl. Phys. **B896**, 555 (2015), arXiv:1502.04999 [hep-lat].

[37] H.-W. Lin, T. Blum, S. Ohta, S. Sasaki, and T. Yamazaki, Phys. Rev. **D78**, 014505 (2008), arXiv:0802.0863 [hep-lat].

[38] T. Yamazaki, Y. Aoki, T. Blum, H.-W. Lin, S. Ohta, S. Sasaki, R. Tweedie, and J. Zanotti, Phys. Rev. **D79**, 114505 (2009), arXiv:0904.2039 [hep-lat].

[39] J. Green, N. Hasan, S. Meinel, M. Engelhardt, S. Krieg, J. Laeuchli, J. Negele, K. Orginos, A. Pochinsky, and S. Syritsyn, (2017), arXiv:1703.06703 [hep-lat].